ISSN 1849–0751 (On–line)
ISSN 0013–7448 (Print)
UDK 621.31
https://doi.org/10.37798/EN2025742

Journal of Energy

VOLUME 74 Number 2 | 2025

74 ENERGIJA

Journal of Energy

Scientific Professional Journal Of Energy, Electricity, Power Systems
Online ISSN 1849–0751, Print ISSN 0013–7448, VOL 74
https://doi.org/10.37798/EN2025742

Published by
HEP d.d., Ulica grada Vukovara 37, HR–10000 Zagreb
HRO CIGRÉ, Berislavićeva 6, HR–10000 Zagreb
University of Zagreb FER, Unska 3, HR–10000 Zagreb

EDITORIAL

The first article presents experimental research on heat transfer near the critical pressure and in the post-critical heat flux (CHF) region. The experiments were carried out using the SCARLETT test facility at the Institute of Nuclear Technology and Energy Systems, University of Stuttgart. Two test sections with different inner diameters (6 mm and 10 mm) were used to investigate CHF and post-CHF heat transfer. The results show variations in heat transfer behaviour under different pressures and heat fluxes, with particular attention to phenomena such as the »boiling crisis« and »upstream CHF.« This research improves the understanding of heat transfer in CO2-cooled systems, which is essential for the safety design of future nuclear reactor systems.

The article »Neutron Kinetics Modelling for Simulations of Loss of Coolant Accidents in The Nuclear Power Plants« discusses the limitations of the Point Kinetics Equation (PKE) in simulating Intermediate Break Loss of Coolant Accidents (IB LOCA) in nuclear power plants. Using a 3D core modelling capability in CATHARE 3, the study highlights how heterogeneous voiding and slower dynamics in IB LOCA scenarios challenge the accuracy of current 0D neutronic models. The research shows that while PKE is effective for Large Break LOCA, it may result in conservative or under-conservative predictions in IB LOCA due to non-uniform fluid density and temperature changes across the core. This work provides valuable insights into the complex phenomena of IB LOCA and lays the foundation for next-generation tools to improve nuclear reactor safety.

The third article introduces an innovative adaptive control strategy for wide-bandgap semiconductor-based inverters (SiC and GaN), aimed at improving energy efficiency, stability, and fault tolerance in high-frequency applications. Through comprehensive simulations, the authors show that the proposed approach reduces the Integral of Time-weighted Absolute Error (ITAE) by 40% compared to traditional control methods such as PID and PWM, achieving efficiencies of 98.5% for SiC and 99% for GaN inverters. The adaptive control dynamically adjusts parameters in real time, ensuring system stability and reliability under varying load and thermal conditions. Furthermore, it significantly reduces electromagnetic interference (EMI) and switching losses, thereby enhancing energy efficiency and extending device lifespan. This work provides a solid foundation for the development of next-generation energy-efficient inverters, with particular emphasis on applications in electric vehicles and renewable energy systems.

The fourth article delves into a critical analysis of core quenching during severe accidents in light water reactors (LWRs). The study examines the QUENCH-03 experiment, conducted at the Karlsruhe Institute of Technology, which investigates hydrogen production during core reflooding – a key safety measure to prevent reactor overheating. Using the ASYST code, the authors performed uncertainty quantification to address the challenges posed by the complex physical-chemical phenomena during quenching. Their findings highlight the significant impact of input uncertainties on simulation results, with variations in parameters leading to substantial differences in output data, such as cladding temperature and hydrogen production. This research underscores the importance of incorporating uncertainty analysis in nuclear safety studies to enhance the accuracy and reliability of severe accident models.

The final article presents an innovative approach to addressing deep penetration shielding challenges in pressurised water reactors (PWRs). Employing contributon theory within the FW-CADIS hybrid shielding methodology, the authors optimise the simulation of fast neutron irradiation in the reactor pressure vessel (RPV) upper head. By combining forward and adjoint flux solutions, the contributon flux identifies critical spatial regions contributing to shielding responses, enabling local SN mesh refinement and improved variance reduction parameters. This refined approach significantly enhances computational efficiency and accuracy, reducing simulation time while maintaining robust results. The study demonstrates the potential of contributon-informed mesh refinement for complex shielding problems, paving the way for more effective and efficient nuclear safety analyses.

Igor Kuzle
Editor–in–Chief

Journal of Energy

VOLUME 74 Number 2 | 2025

journal homepage: http://journalofenergy.com/

Experimental Investigation of Critical Heat Flux and Post-Critical Heat Flux in a Carbon Dioxide-Cooled Tube at High Subcritical Pressures

Jakub Bronik, Michael Buck, Jörg Starflinger

***Summary* — Supercritical fluids such as water or CO_2 are an attractive choice for future nuclear reactor systems. The exact knowledge of the heat transfer in a trans-critical pressure is important for the design of those systems. In subcritical pressure, knowing how to avoid the reduction of heat removal when exceeding the critical heat flux (CHF) is of critical importance.**

A series of experiments is carried out with the SCARLETT (Supercritical CARbon dioxide Loop at IKE StuTTgart) test facility at the Institute of Nuclear Technology and Energy Systems of the University of Stuttgart, focusing on investigations of CHF and post-CHF heat transfer with CO_2 as a working fluid. Two test sections have been used – each with a different internal diameter - to investigate CHF and post-CHF heat transfer. Both test sections with 10 mm and 6 mm internal diameters and heated lengths of 2000 mm are equipped with glass fiber in a stainless-steel capillary for semi-continuous wall temperature measurement and thermocouples for the reference temperature measurement. The test sections are instrumented accordingly for pressure, differential pressure, mass flow, inlet, and outlet temperature measurements. The paper presents CHF, upstream CHF, and boiling heat transfer measurements in selected experiments in the 10mm tube at subcritical pressures of pr=0.7 and pr=0.98, mass fluxes of 1000 kg/m2s, and heat fluxes from 80 to 200 kW/m2.

***Keywords* — CHF, post-CHF, dryout, OFDR, boiling**

I. Introduction

In transient operations of thermal cycles designed to operate at a supercritical state, pressure may pass the critical pressure and thus lead to a transition between supercritical and subcritical states under normal or abnormal conditions. Reliable models for heat transfer in both supercritical and subcritical states therefore, play an important role in safety design and safety analysis.

Figure 1 shows schematically the heat transfer in two-phase flow using the boiling curve, which represents the heat flux as a function of the superheat of the heated wall. At low heat flux, nucleate boiling takes place on the heated wall. However, if the heat flux continues to increase and reaches a critical value, direct contact between the liquid and the heated wall is lost, and heat transfer is significantly reduced. If the imposed heat flux remains constant, the regime changes from bubble boiling to film boiling, and the wall temperature increases significantly. This phenomenon is called boiling crisis, and the corresponding heat flux is called critical heat flux (CHF). The regime after the appearance of the boiling crisis is called post-CHF. Even if the heat flux is reduced after the occurrence of the boiling crisis, the flow regime remains in the film boiling (post-CHF region) until the wall temperature falls below the so-called minimum film boiling temperature (Leidenfrost point). Then the wall is wetted again with liquid and a sudden drop in the wall temperature occurs. This process is called rewetting.

Heat transfer in the subcritical pressure state, including post-CHF heat transfer, has been studied very intensively in the past for reduced pressures up to p/pcrit≤0.7 (ratio referred to as p_r), also because of its importance in light water reactors [1]. There exists a large number of models or correlations developed for this pressure range.

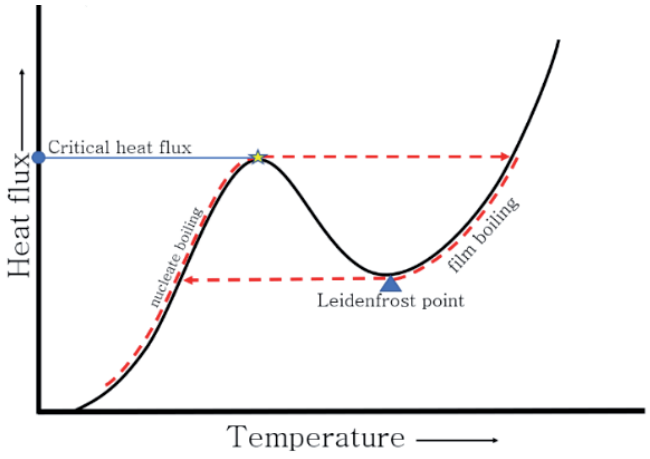

Fig. 1. Boiling curve.

However, studies of heat transfer under subcritical pressure conditions but in the high-pressure range $0.7<p_r<1$ have been scarce [2], and correspondingly, the theoretical prediction models lack validation and are only applicable for a limited range of conditions. E.g., analysis of the transient processes in a 4-rod bundle with water cooling showed that the thermohydraulic system code ATHLET cannot satisfactorily predict heat transfer in the high-

Corresponding author: Jakub Bronik

Jakub Bronik, Michael Buck and Jörg Starflinger are with the University of Stuttgart, Institute of Nuclear Technology and Energy Systems, Stuttgart, Germany

(emails: jakub.bronik@ike.uni-stuttgart.de, michael.buck@ike.uni-stuttgart.de, jorg.starflinger@ike.uni-stuttgart.de)

Jakub Bronik, Michael Buck, Jörg Starflinger, Experimental Investigation of Critical Heat Flux and Post-Critical Heat Flux in a Carbon Dioxide-Cooled Tube at High Subcritical Pressures, Journal of Energy, vol. 74 Number 2 (2025), 3–7
https://doi.org/10.37798/2025742716

pressure range [3]. The experiment showed that during the transient process with decreasing pressure from 25 MPa to 17 MPa, a sharp increase in wall temperature occurs at a pressure of about 21 MPa. This corresponds to the appearance of the boiling crisis, which, however, was not predicted by the ATHLET code.

The present paper concentrates on the experimental investigations to improve the knowledge about the physical processes of heat transfer at subcritical pressures near the critical point and in the adjacent post-CHF range.

II. Experimental Setup

All experiments presented in this publication were carried out in the SCARLETT (Supercritical Carbon dioxide Loop at IKE Stuttgart) test facility at IKE. SCARLETT works as a peripheral facility used to provide CO_2 under defined parameters: mass flow rate, temperature, and pressure near the critical point. Detailed information about SCARLETT is available in Flaig et al. [4]. While SCARLETT has been used in the past mostly to work at supercritical pressure, the facility has been modified for the present experiments to safely operate in subcritical pressures. This was achieved by the implementation of a reduction valve upstream of the test section. A simplified schematic is presented in Fig. 2.

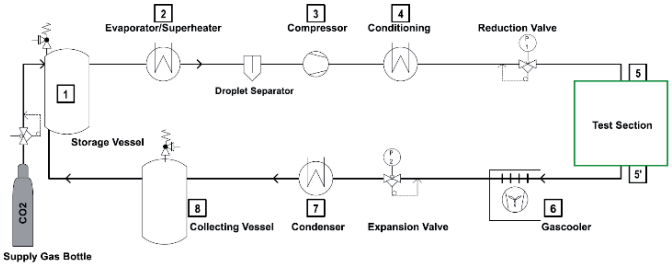

Fig. 2. SCARLETT schematic.

For the investigations presented in this publication, two different test sections have been used, with 6 mm, and 10 mm inner diameters. Another diameter was chosen due to the convenience of obtaining the pipes. The 6 mm and 10mm test sections can be seen in Figure 3. The test sections were operated in parallel, which has the advantage that the mass flow rate through each test section can be adjusted by diverting flow through the other test section. The test sections have the same structure; the only difference is the diameter of the test tubes used. The test tubes are heated directly with a 35 kW DC power supply. To insulate the test rig electrically from the test tubes, special insulating flanges are used. The mass flow rate and bulk temperature of the CO_2 are measured just before the entry into the test sections. Fig. 3 shows the dimensions of the test tubes with an inner diameter of 6 and 10 mm and an outer diameter of 8 and 12 mm. The material of the tubes is Alloy 625.

The total length of the test tubes is 2533 mm with a heated length of 2000 mm. The tubes are instrumented with glass fiber in a stainless-steel capillary for temperature measurement. As a reference and for calibration purposes, 20 T-type thermocouples are tied with a temperature-resistant yarn straight in 100 mm intervals on the outer surface of the test tube adjacent to the capillary. Both thermocouples and capillary have been electrically insulated from the pipe with a 200 µm thick mica paper layer. The absolute pressure is measured before and after the heated section, and the differential pressure is measured over the heated length. The pressure inside the test tube is measured through a 1 mm hole to avoid influencing the flow – the setup can be seen in Figure 3 on the bottom right. A more detailed description can be found in [5].

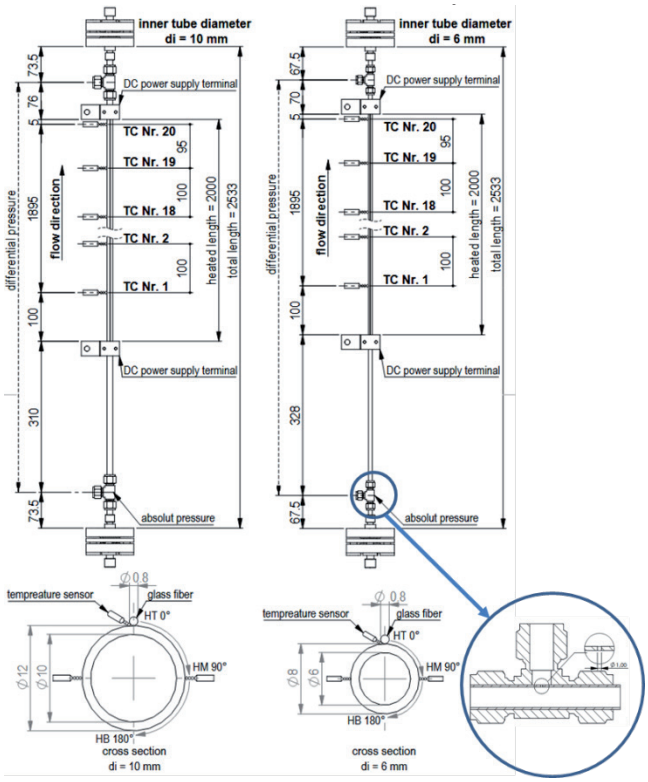

Fig. 3. Test section and pressure tapping.

A. Glass Fiber Setup

The relationship between the relative changes of wavelength λ and frequency f, temperature T, and strain ε is approximately linear, as eq. (1) below indicates. The coefficients KT and Kε depend on the material and can vary by up to 10% between standard telecom glass fibers.

$$\frac{\Delta\lambda}{\lambda} = -\frac{\Delta f}{f} = K_T\,\Delta T + K_\varepsilon\,\varepsilon \tag{1}$$

For a strain-free measurement, equation (1) can be transformed into equation (2) to provide the temperature change as a linear function of the measured frequency change [6].

$$\Delta T = -\frac{\bar{\lambda}}{c_0\,K_T}\,\Delta f \tag{2}$$

For measurements over broader temperature ranges and/or for considering fiber-coating interactions [6], nonlinear fits to the correlation between temperature and frequency, e.g., using more accurate polynomials [7]. The relation between temperature and frequency changes was approximated by a second-order polynomial according to equation (3) for the fiber used in this setup.

$$\Delta T = -A\Delta f^2 + B\Delta f + C \tag{3}$$

The coefficients A, B, and C given in Table 1 below were determined by fitting the polynomial (3) to the measurements of the type T thermocouples.

Jakub Bronik, Michael Buck, Jörg Starflinger, Experimental Investigation of Critical Heat Flux and Post-Critical Heat Flux in a Carbon Dioxide-Cooled Tube at High Subcritical Pressures, Journal of Energy, vol. 74 Number 2 (2025), 3–7
https://doi.org/10.37798/2025742716

TABLE I.

GLASS FIBER TEMPERATURE FIT COEFFICIENTS.

10 MM	A	-9.51E-07	B	9.51E-02	C	2.625E+01
6 MM	A	-1.43E-06	B	9.64E-02	C	2.7175+01

III. EVALUATION METHODOLOGY

Table 2. gives an overview of the measured parameter ranges.

TABLE 2.

EXPERIMENTAL OVERVIEW

Parameter [Unit]	Value
Inner tube diameter [mm]	10
Flow direction [-]	upward flow
Inlet pressure [MPa]	5.2, 7.2
Inlet temperature [°C]	8
Mass flux [kg/m²s]	1000
Heat flux [kW/m²]	80-200

In the following, a short overview of the calculations of the main variables is given. The National Institute of Science and Technology (NIST) database REFPROP provides the fluid properties [8].

$$\dot{Q}_{th} = P_{el} = U \cdot I \tag{4}$$

Heat flow rate $\dot{Q}_{th}$ gained by the fluid was calculated from the electric power P_{el} with the voltage U and the current I.

The heat flux $\dot{q}$ is calculated with the curved surface area of the inner surface A_i of the tube and the heated length with the assumption of a uniform heat generation by direct electrical heating, the heated length L_h, and internal diameter d_i.

$$\dot{q} = \frac{\dot{Q}_{th}}{A_i} = \frac{U \cdot I}{\pi \cdot d_i \cdot L_h} \tag{5}$$

For the calculation of the bulk temperature $T_{b,y}$ across the axial position of the tube y, a linear approximation of the pressure losses is assumed. Specific enthalpy at the axial position $i_{b,y}$ is calculated with enthalpy at inlet conditions $i_{b,in}$ and mass flow $\dot{m}$.

$$T_{b,y} = \mathrm{f}(i_{b,y}, p_y) \tag{6}$$

$$i_{b,y} = i_{b,in} + \left(\frac{y}{L_h}\right) \cdot \frac{\dot{Q}_{th}}{\dot{m}} \tag{7}$$

With the mathematical heat conduction model of a circular tube with uniform heat generation, an insulated outer surface, and a cooled inner surface, the inner wall-temperature $T_{w,i}$ can be calculated with the measured outer wall-temperature T_{625} and the volumetric heat flux $\dot{q}_v$ [9, p.152] and outer diameter d_o. The thermal conductivity λ_{625} of Alloy 625 was also approximated linearly over the temperature $\lambda_{625} = \mathrm{f}(T_{w,o})$.

$$T_{w,i} = T_{w,o} + \frac{\dot{q}_v}{4\lambda_{625}}\left[\left(\frac{d_o}{2}\right)^2 - \left(\frac{d_i}{2}\right)^2\right] - \frac{\dot{q}_v}{2\lambda_w}\left(\frac{d_o}{2}\right)^2 \cdot \ln\left(\frac{d_o}{d_i}\right) \tag{8}$$

$$\dot{q}_v = \frac{\dot{Q}_{th}}{\frac{\pi}{4}\left({d_o}^2 - {d_i}^2\right) \cdot L_h} \tag{9}$$

The inner wall temperature wall calculation has been repeated with the thermal conductivity of the tube at the mean wall temperature $\lambda_{625} = \mathrm{f}(\overline{T_{w.m}})$, where:

$$\overline{T_{w,m}} = \frac{T_{w,i} + T_{w,o}}{2} \tag{10}$$

In the last step, the heat transfer coefficient htc can be calculated for each temperature measurement point across the tube's axial position.

$$htc_y = \frac{\dot{q}}{T_{w,i,y} - T_{b,y}} \tag{11}$$

IV. RESULTS

Figure 4 shows the axial profiles of the wall temperature along the 10mm tube at p_r = 0.7 (52 bar) and at p_r = 0.98 (72 bar) for different values of heat flux up to 130 kW/m², 8°C inlet fluid temperature, and 1000 kg/m²s mass flux. The calculated bulk fluid temperature at the plot represents the values obtained for the highest heat flux at the plot.

The temperature profiles for the 52 bar were obtained after reaching the critical heat flux in a power ramp up (temperature excursion at the end of the heated length at 105±1.2 kW/m²) and fur-

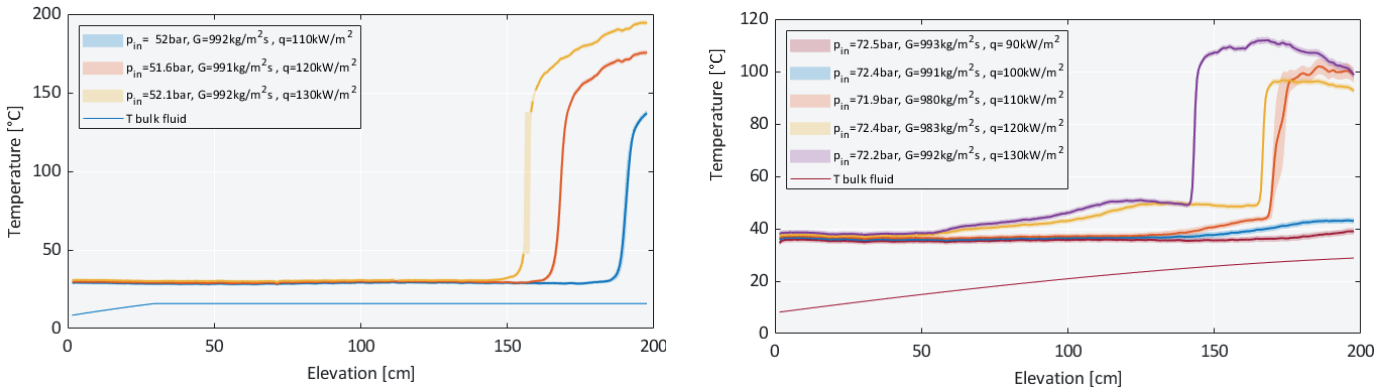

Fig. 4. Temperature profiles at increasing heat flux up to 130 kW/m² at p_r=0.7 and pr=0.98. T_{in}=8°C and G=1000 kg/m²s.

Jakub Bronik, Michael Buck, Jörg Starflinger, Experimental Investigation of Critical Heat Flux and Post-Critical Heat Flux in a Carbon Dioxide-Cooled Tube at High Subcritical Pressures, Journal of Energy, vol. 74 Number 2 (2025), 3–7
https://doi.org/10.37798/2025742716

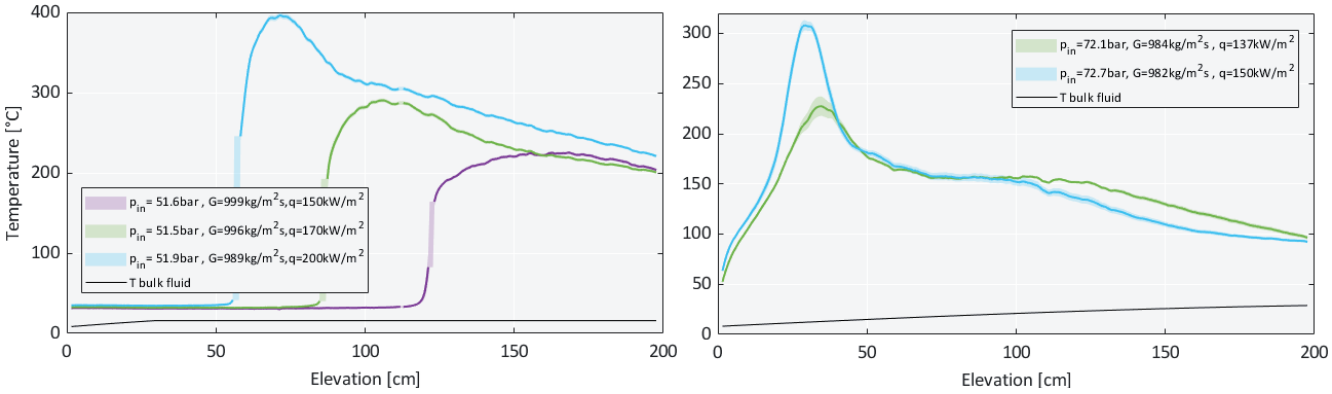

Fig. 5. Temperature profiles at increasing heat flux above 130 kW/m² at p_r=0.7 and p_r=0.98. T_{in}=8°C and G=1000 kg/m²s

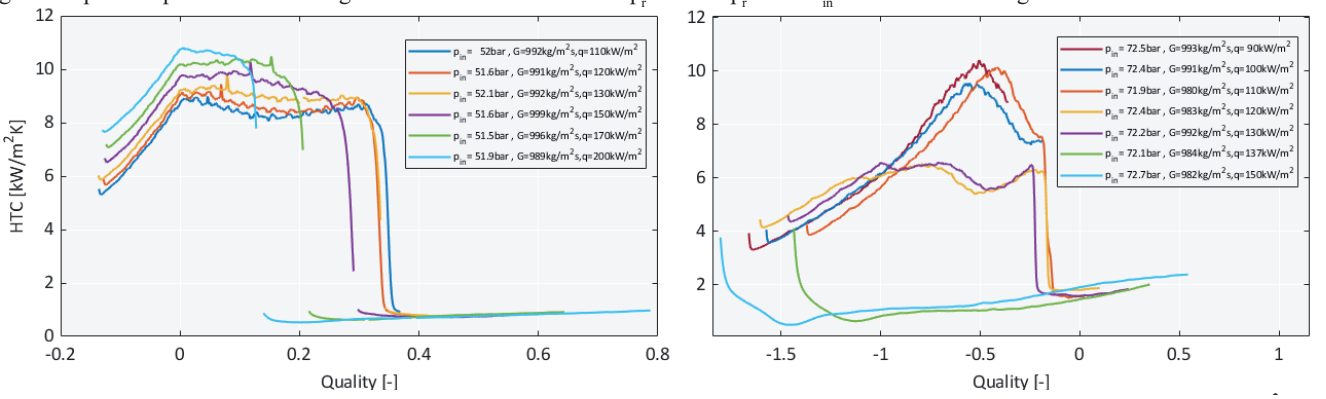

Fig. 6. Heat transfer coefficients in relation to equilibrium quality at increasing at p_r=0.7 and p_r=0.98. T_{in}=8°C and G=1000 kg/m²s.

ther raise of the heating power to obtain post-CHF conditions. The power was kept constant for a sufficiently long period to produce a sequence of steady-state conditions. Detailed description of data recording, averaging, and methodology can be found in [5].

The position of the steep temperature increase corresponds to the CHF point; the CHF conditions have to be taken as the local conditions at the jump position, which defines a "virtual" end of the heated length. At the presented heat fluxes, the post-steep increase profiles exhibit an inclined shape, suggesting the main heat transfer interaction to be heat transfer between the wall and the heated vapor in post-CHF, where the near-wall vapor is gradually superheated.

The temperature profiles at 72 bar were obtained similarly; however, there were two indications of a jump-wise temperature increase at the end of the heated length (first at 86±0.8 kW/m², second at 105±0.5 kW/m²). The profiles obtained after the first CHF-like-event indication (at 90 and 100 kW/m²) show a mild temperature increase of about 8°C compared to the wall temperature at nucleate boiling upstream of the tube. This first temperature jump

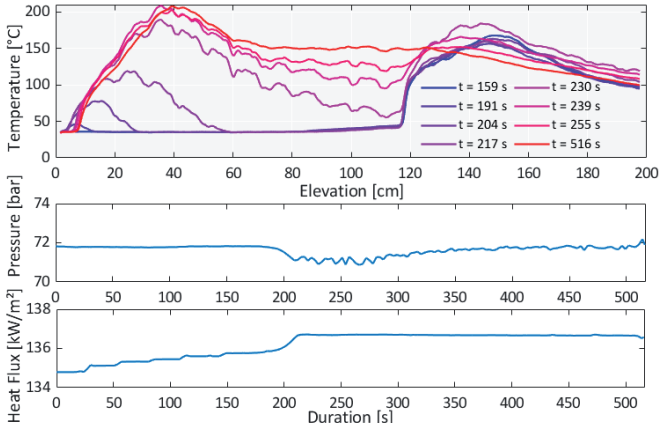

Fig. 7. Development of temperature profile at upstream CHF.

is present at each superheating and is interpreted to be some sort of unstable boiling due to froth flow or dry patching, rather than CHF. The second temperature jump in the profiles with 110, 120, and 130 kW/m² is much larger (>50°C). The plateau shape of those profiles after the location of CHF suggests a stable temperature of vapor. At 130 kW/m² there is a small decrease of temperature at the end of the heated length – this indicates a stronger influence of droplet evaporation, as vapor picks up speed. The maximum wall temperatures obtained in those experiments are much lower when compared to the ones in corresponding cases in 52 bar.

Figure 5 presents the results of overheating the pipe at both pressures above 130 kW/m². The profiles at 52 bar show the evolution in shape from inclined lines at the previous plot to a convex shape with a maximum at 150 kW/m². There, the superheated steam reaches equilibrium, and the main heat transfer mechanism becomes the evaporation of droplets from superheated vapor, leading to an increase in the vapor speed. The following profiles have a temperature peak in the first half of the heated length – indicating a change of CHF mechanism from dryout to DNB – where due to violent change to reverse annular boiling the wall temperature rises, the main heat transfer mechanism becomes radiation from wall to liquid core and its evaporation – leading to speed up of vapor at the wall until it reaches equilibrium state.

At the pressure of 72 bar the temperature profiles change drastically due to the occurrence of upstream CHF, a CHF mechanism taking place in the middle or the beginning, believed to happen due to the change of flow pattern [9, 10, 11]. It results in a spike-like peak of temperature and temperature profile development up the stream, similar to the post-DNB case. In this case, nucleate boiling does not happen anywhere along the heated length. It has to be noted that the wall superheat at the hottest point in the 150 kW/m² case is 100 K higher than the hottest temperature at a corresponding case at 52 bar. The power was not further increased to avoid damaging the test section.

Figure 7 shows the evolution of the temperature profile upon passing the upstream CHF value – the small peak in temperature at

Jakub Bronik, Michael Buck, Jörg Starflinger, Experimental Investigation of Critical Heat Flux and Post-Critical Heat Flux in a Carbon Dioxide-Cooled Tube at High Subcritical Pressures, Journal of Energy, vol. 74 Number 2 (2025), 3–7
https://doi.org/10.37798/2025742716

the beginning of the heated channel at t = 191s evolves in a matter of 42 seconds to reach maximum temperature. It has to be noted that at the beginning of the process, both temperature peaks – due to classical and upstream CHF – increase. Starting at t = 239 s, the peak due to classical CHF starts to diminish. Upstream CHF is followed by a disturbance in test section pressure due to flow regime change and a slight increase of heated power, due to drastic temperature change on the whole heated length and significant increase of its electrical resistance.

Figure 6 shows the heat transfer coefficients calculated from the corresponding experiments at Figures 4 and 5 in relation to equilibrium quality. In case of the experiments at 52 bar all the CHF events happened at a positive quality, indicating usual two-phase flow regimes, and in case of experiments at 110-130 kW/m^2, a dryout mechanism of CHF. At 72 bar, as the CHF always happens at subcooled conditions, the CHF mechanism has to be DNB. It should be noted as well that the first degradation of heat transfer leads to a 20% decrease in the heat transfer coefficient.

V. Conclusions

A series of experiments at p_r = 0.7 and p_r = 0.98 has been performed. At lower reduced pressures, CHF happened solely at positive qualities, while at close critical pressure, it happened only in subcooled conditions. While at high pressures, a pre-CHF heat transfer deterioration happened, the wall temperatures in the post-CHF regime were lower than in corresponding p_r = 0.7 experiments. This improved performance is, however, limited by the possibility of upstream CHF, which is due to a heavy decrease of the heat transfer coefficient that is even lower than in the presented post-DNB cases.

VI. References

[1] D. Yu, F. Feuerstein, L. Köckert, X. Cheng, "Analysis and modelling of post-dryout heat ransfer in upward vertical flow", Ann. Nucl. Energy vol. 115, pp 186-194, May 2018

[2] D.B. Marchetto, "A state-of-the-art review on flow boiling at high reduced pressures", Int.J. Heat Mass Transf., Vol. 193, 2022

[3] M. Q. Song, X. J. Liu, X. Cheng, "Heat transfer analysis of trans-critical pressure transient, Annual Meeting of Nuclear Engineering", Berlin, Germany, May 7-8, 2019.

[4] W. Flaig, "Setup of the supercritical CO2 test facility SCARLETT for basic experimental investigations of a compact heat exchanger for an innovative decay heat removal system", J. Nucl. Eng. Radiat. Sci., 4 (3) (2018)

[5] J Bronik et al. 'Experimental investigation of critical heat flux and post-critical heat flux in a carbon dioxide-cooled tube at high subcritical pressures', NUTHOS 14, Vancouver, Aug 25-28 2024

[6] A.K. Sang et al. "One Centimeter Spatial Resolution Temperature Measurements in a Nuclear Reactor Using Rayleigh Scatter in Optical Fiber". IEEE Sens.J., vol.8, p1375–1380, 2008.

[7] Luna Innovations Incorporated, Distributed Fiber Optic Sensing: Temperature Coefficient for Polyimide Coated Low Bend Loss Fiber, in the 10°C - 80°C Range, Blacksburg, 2014.

[8] REFPROP, NIST SRD 23, USA, 2010

[9] Kitto, J. B., "Upstream Critical Heat Flux and Its Design Implications". Heat Transf. Eng, 43(6), 475–484, 2021

[10] D. C. Groeneveld, "The occurrence of upstream dryout in uniformly heated channels," Proc. 5th Inter. Heat Transfer Conf., Tokyo, Japan, Sept. 3–4, 1974,vol. 4, pp. 265–269

[11] Y. Katto and S. Yokoya, "CHF of force convection boiling in uniformly heated vertical tubes: Experimental study of HP-regime by the use of refrigerant 12," Int. J. Multiphase Flow, vol. 8, no. 2, 165–181, Apr. 1982

Jakub Bronik, Michael Buck, Jörg Starflinger, Experimental Investigation of Critical Heat Flux and Post-Critical Heat Flux in a Carbon Dioxide-Cooled Tube at High Subcritical Pressures, Journal of Energy, vol. 74 Number 2 (2025), 3–7
https://doi.org/10.37798/2025742716

Journal of Energy

VOLUME 74 Number 2 | 2025

journal homepage: http://journalofenergy.com/

Neutron Kinetics Modelling for Simulations of Loss of Coolant Accidents in The Nuclear Power Plants

Bartlomiej Klis, Simon Primeau, Patrick Blaise, Jean-Christophe Lecoy, Marie-Christine Grouhel

***Summary* — The code used by Framatome to predict the progression of a LOCA is the system scale thermal-hydraulic code CATHARE (Code Avancé de THermoHydraulique pour les Accidents deRéacteurs à Eau). It calculates the full primary and secondary circuits including the core and the fuel elements. CATHARE currently utilizes a 0D neutronic model that solves the PointKinetics Equation (PKE) to determine the evolution of instantaneous fission power. This approach is suitable for transients where the core's moderator density changes rapidly in a quasi-uniform manner, such as in large break LOCA scenarios (from the initial situation with a core full of liquid to a sudden and complete voiding leading to a full vapour environment). However, during Intermediate Break (IB) scenarios, with slower dynamics, the assumption of a uniform core's moderator density is no longer valid. This assumption results in a significant underestimation of void antireactivity in the upper part of the core and a slight overestimation at the bottom. Thus, using PKE for IB-LOCA leads to an overestimation of the fission power, and the more heterogeneous the core, the higher the conservatism of this hypothesis is expected. In fact, the specific application of IB-LOCA involves a precise neutronic calculation in a strongly diphasic fluid environment which is first due to the uncovering of the core and then to its reflooding by the safety injections. The presented work relies on the development of a fine 3D coupling between neutronics and thermal-hydraulics at the assembly scale plunged into a fullreactor simulation. Such a development goes beyond the known limitations of current neutronics/thermal-hydraulics couplings (dealing with low void fraction situations) which are notsuitable for LOCA safety studies.**

***Keywords* — nuclear safety, thermo-hydraulics, neutronics, code coupling**

I. Introduction

In this work, authors present the neutron kinetics model commonly used for the loss of coolant accidents (LOCA) safety studies by system scale thermal-hydraulics (TH) codes. We hereby present the results of calculations done by CATHARE 3 with full 3D core modelling at the assembly scale of a 3-loop pressurized water reactor (PWR) for Intermediate Break LOCA (IB LOCA). The main observation we would like to emphasize is that many other studies involving system scale TH codes use the point kinetics equation (PKE) for prediction of fission power evolution during the LOCA transients. Keeping in mind this approach is well penalized and validated to be conservative in variety of safety studies, we will challenge 0D neutronic modelling and justify the need for new developments of multi-physics methods for LOCA safety studies.

More advanced neutron kinetics models exist than PKE, which are either the result of deterministic neutron transport codes solving Boltzmann equation or Monte Carlo codes using large statistics of tracing down each individual particle interactions. Some authors in their studies, often focused on operational conditions and non-LOCA accidents, use tools which involve thermal-hydraulics/neutronics (TH-N) loose couplings (also called black box couplings) to incorporate better neutron kinetics modelling with possibility to model 3D power distribution changes in the core. An example is a study done with RELAP5/PARCS by Peakman et al. [1]. Some other researchers studied direct TH-N coupling methods using for example the Newton-Krylov approach like Zhang et al. [2]. Unfortunately, they are not yet implemented in the form of mature codes and methods for the nuclear industry. However, based on bibliography, we spotted a gap in studies related to loss of coolant accidents (LOCA), which we think are worth investigating using high-fidelity methods involving the TH-N couplings. This was also identified in Wang et al. work from 2019 where the author presented a thorough review of multiple TH-N couplings [3]. It seems nontrivial that any recent code coupling described so far be specifically designed to address the physics of LOCAs for PWRs. An example can be the recent work of Peakman et al. [4]. A recent review on TH and neutronics fuel screening methods made by Gorton et al. from Oak Ridge in 2023 [5] mentioned the limitations of PKE in the system scale code RELAP5 (Reactor Excursion and Leak Analysis Program) and a multi-physics coupling was pointed to solve these issues. Similar conclusions were pointed by P. Ruyer from IRSN (nowadays ASNR) [6]. Lastly, the need for developments of multi-physics tools at system scale has also recently been discussed during the OECD/NEA/CSNI Specialists Meeting on Transient Thermal-hydraulics [7].

Corresponding author: Bartlomiej Klis

Bartlomiej Klis, Simon Primeau, Patrick Blaise, Jean-Christophe Lecoy, and Marie-Christine Grouhel are with the Framatome, DTIPD, Taverny, France (emails: bartlomiej.klis1@framatome.com, simon.primeau@framatome.com, patrick.blaise@framatome.com, jean-christophe.lecoy@framatome.com, mariechristine.grouhel@framatome.com)

Bartlomiej Klis, Simon Primeau, Patrick Blaise, Jean-Christophe Lecoy, Marie-Christine Grouhel, Neutron Kinetics Modelling for Simulations of Loss of Coolant Accidents in The Nuclear Power Plants, Journal of Energy, vol. 74 Number 2 (2025), 8–12
https://doi.org/10.37798/2025742719

CATHARE (Code for Analysis of Thermal-Hydraulics during Accident of Reactor and safety Evaluation) is the system scale TH code used in Framatome to predict the transient simulation of LOCA [8]. Currently, CATHARE utilizes a 0D neutronic model that solves PKE to determine the evolution of instantaneous fission power.

II. Point Kinetics Equation

The neutron point kinetics is described by a system of ordinary differential equations composed of one equation for neutron population and N_d-equations for delayed neutron precursor groups. Many authors use six precursor groups as initiated by the study of G. R. Keepin et al. [9].

Neutron population is described by the following equation:

$$\frac{d}{dt}n(t) = \frac{\rho(t) - \beta}{\Lambda}n(t) + \sum_{i=1}^{Nd} \lambda_i C_i(t) \quad (1)$$

Whereas the N_d equations for delayed neutron precursors are shown below:

$$\frac{d}{dt}C_i(t) = \frac{\beta_i}{\Lambda}n(t) - \lambda_i C_i(t) \quad (2)$$

Where: n(t) – number of neutrons, $\rho(t)$ – reactivity, β – effective delayed neutron fraction, β_i - delayed neutron fraction of i-th precursor group, Λ – average neutron generation time, λ_i - decay constant for i-th delayed neutron precursor group, $C_i(t)$ - concentration of i-th delayed neutron precursor group.

By solving this system of equations, one can predict fission power evolution for a given temporal reactivity input. The global reactivity calculation is based on TH data from transient and includes different reactivity feedbacks.

III. Methods

The following study was done using the CATHARE 3 code. For sake of the demonstration, we implemented the complete numerical input of 3-loop PWR nuclear power plant (NPP) with the 3D cartesian core modelling. This level of fidelity was enabled in CATHARE 3 because of recent developments made by Prea et al. from CEA [10]. Thus, our input deck simulates the whole primary and secondary circuits, as well as key events for the IB LOCA transient. The new 3D core model can simulate local effects such as gas and liquid crossflows, departure from nucleate boiling due critical heat flux, as well as thermomechanical effects such as cladding ballooning and worsening of heat transfer in the fuel due to burnup fatigue. Figure 1 presents the 3D core model used for this study. The core bypass is modelled via one more axial element connecting the lower and upper plenum objects. Figure 2 reproduces the penalized core map. Three concentric rings, each using a different average linear heat generation rate (LHGR) for the rods were used. This allows to generate a bounding TH environment for the *hot rod*, which is the fuel rod with the highest LHGR located in centre of core model. Thus, the *hot rod* reaches the highest possible cladding temperatures and is used to evaluate safety criterions. Total power of the core was slightly higher than maximal nominal value. The central ring (red) concentrates the assemblies with rods having high LHGR and contains the *hot rod*, next ring (yellow) represents assemblies of mean core, and finally assemblies in outer ring (green) have the decreased LHGR to balance the total core power. In this cartesian core modelling, some corner regions are inactive (grey), no TH connection is allowed with these nodes and no calculations are done inside them.

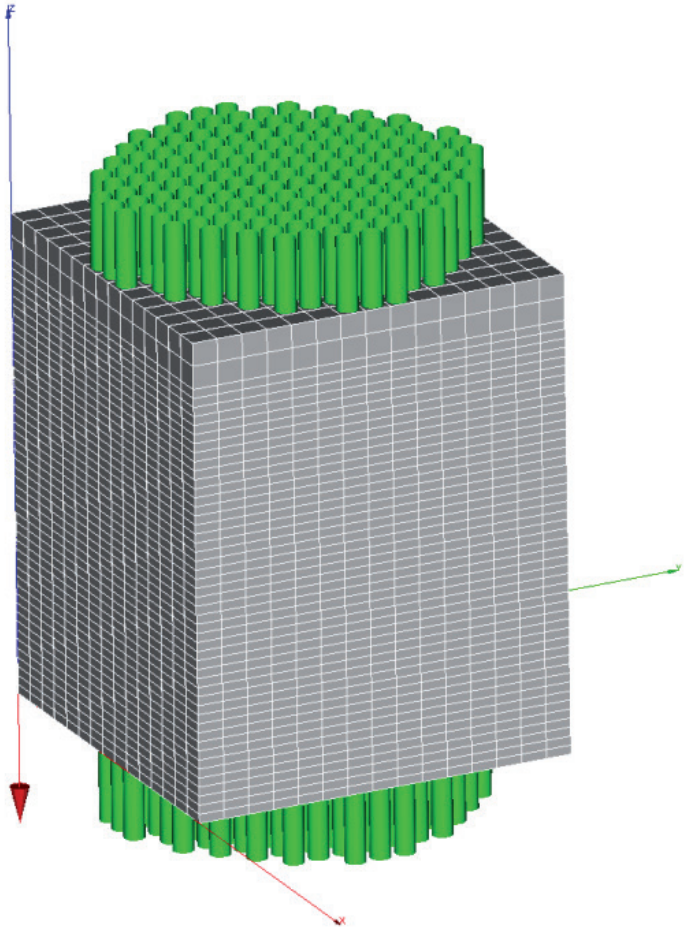

Fig. 1. CATHARE 3D core model

Additionally, the 0D neutronics model using the PKE was utilized to predict the fission power evolution. This allows the validation of CATHARE 3 for simulation of the core pre-accident phase and the transient after the break opening. The corresponding input data for PKE model is a curve of antireactivity along moderator mean core density computed for defined core geometry, fuel loading, burn-up and initial conditions. It is computed separately using assembly lattice deterministic neutronic codes like APOLLO. These calculations result in moderator antireactivity expressed by non-linear formula as a function of average density, which is referred as the *voiding curve*. Additionally, among other neutronic effects, the Doppler feedback law was included.

Bartlomiej Klis, Simon Primeau, Patrick Blaise, Jean-Christophe Lecoy, Marie-Christine Grouhel, Neutron Kinetics Modelling for Simulations of Loss of Coolant Accidents in The Nuclear Power Plants, Journal of Energy, vol. 74 Number 2 (2025), 8–12
https://doi.org/10.37798/2025742719

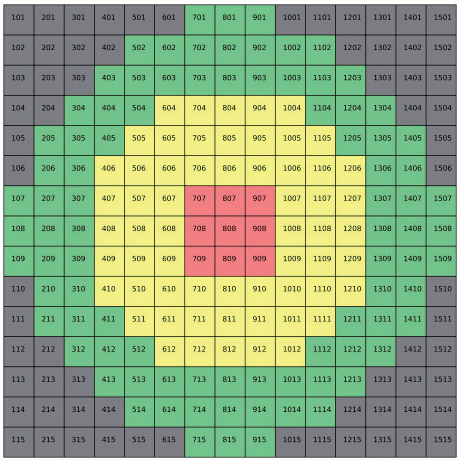

Fig. 2. Core fuel map

IV. Results

A. Description of the IB LOCA Transient

The IB LOCA transient starts when a breach opens in one of the primary coolant loops at full core power. This results in depressurisation of the primary circuit and start of fluid loss from the system. This period is called blowdown phase. Meanwhile, critical heat flux for some of the fuel elements is reached and leads to departure from nucleate boiling regime in their proximity. This causes occurrence of first peak cladding temperature (PCT1) for *hot rod* within the first few seconds of the transient. As the core fission power is going down mostly due moderator antireactivity feedback and SCRAM, the cladding temperature decreases. However, because of decreased pressure and lack of liquid in the core, some claddings are not able to achieve the wet contact with the fluid again. Inside the core, the steam produced does not allow to maintain cooling via heat exchange with fuel rod claddings. The several dozen seconds later, a second peak cladding temperature (PCT2) for *hot rod* occurs when the core is almost empty, this is core uncovery phase, and claddings are heating up adiabatically due to the decay heat. For PCT2 value, the fission energy released in the fuel from the beginning of the transient impacts the adiabatic heating, defining the initial temperature from which this second rise starts. The ultimate and last phase of the transient is referred as core reflooding, when water from the accumulators rushes into the core, rapidly cooling down the claddings and restoring the wet contact with liquid, which improves the heat transfer. From this moment, the active safety systems sustain the cooling of the core, preventing the more severe consequences.

B. Selected Data from the IB LOCA Transient

Some of the IB LOCA transient data are presented below. Due sensitivity of some information presented here, the data was normalized, but main transient features necessary to explain the subject are valid. The normalized PCT evolution during IB LOCA for *hot rod* is presented on the Figure 3. Similarly, the evolution of average fluid density in the core is presented on Figure 4.

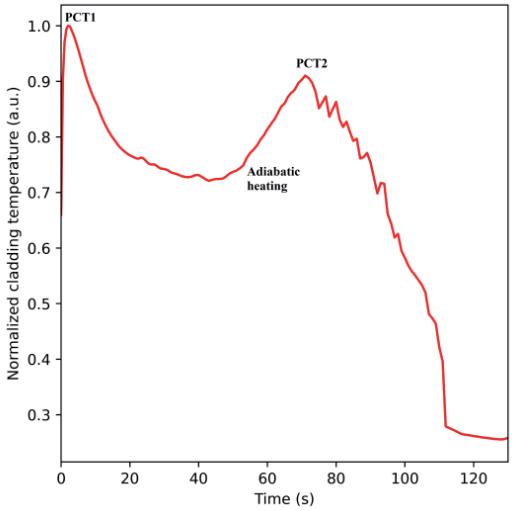

Fig. 3. Normalized maximal cladding temperature evolution with two peaks: PCT1 and PCT2

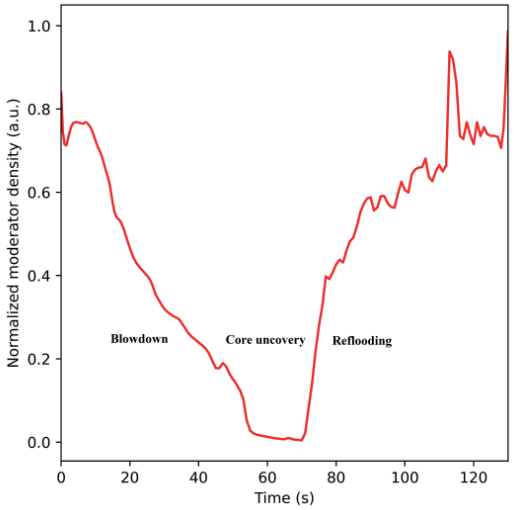

Fig. 4. Normalized average moderator density evolution in the core

We want to focus on the fact that fission power is driven by neutronic feedbacks responding to voiding of the core and fuel temperature evolutions. This power is a result of 0D neutron kinetics model of CATHARE 3. The global fission power evolution is presented on Figure 5. Moreover, the residual and decay power are included in the simulation as additional laws, not presented hereby. In CATHARE, the average fluid density in the core is used to get the moderator antireactivity, based on highly penalized voiding curve law. This feedback is presented on Figure 6. Additionally, the Doppler feedback is modelled via average effective temperature, as presented on Figure 7. However, the Doppler in LOCA is in fact strongly spatially dependent and brings positive reactivity feedback when the fuel cools

Bartlomiej Klis, Simon Primeau, Patrick Blaise, Jean-Christophe Lecoy, Marie-Christine Grouhel, Neutron Kinetics Modelling for Simulations of Loss of Coolant Accidents in The Nuclear Power Plants, Journal of Energy, vol. 74 Number 2 (2025), 8–12
https://doi.org/10.37798/2025742719

down, which may result in neutronic instabilities at the beginning of transient. The average density profile in the core after 1 second of breach opening is presented on Figure 8. Please note that voiding is concentrated locally near the hottest assemblies.

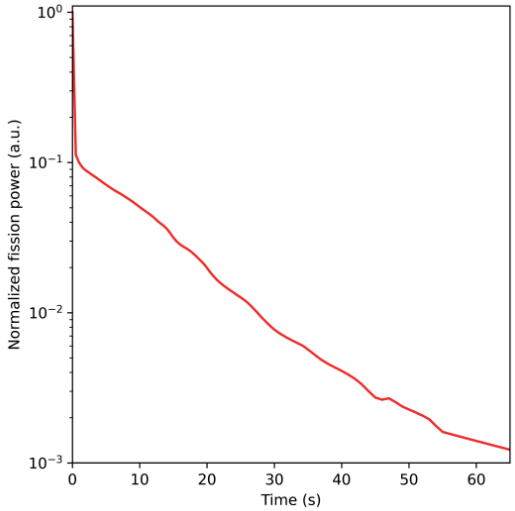

Fig. 5. Normalized global fission power evolution

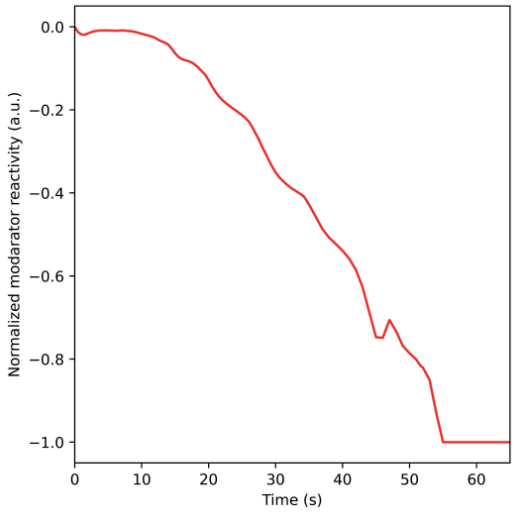

Fig. 6. Normalized moderator reactivity feedback

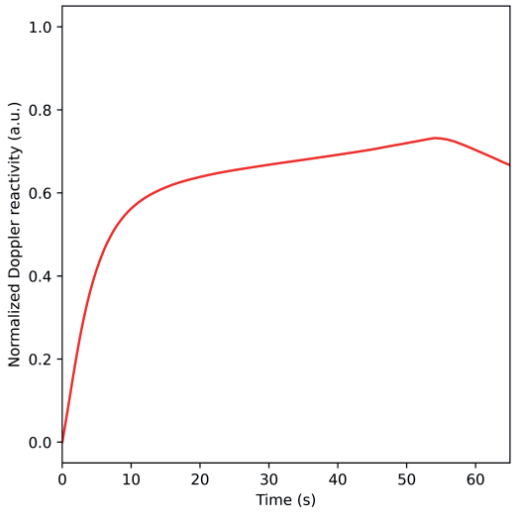

Fig. 7. Normalized Doppler reactivity feedback

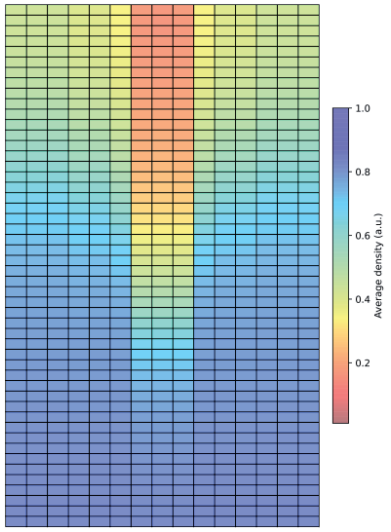

Fig. 8. Normalized average moderator density profile in the core after 1 s of transient

C. Challenging the PKE neutron kinetics

Using new 3D core capacity, we see that density is not changing uniformly in the core for IB LOCA transients, but it is strongly correlated with places where boiling occurs as presented on Figure 8. The other places in the core, mostly near its bottom have similar TH conditions as at the pre-accident phase. Thus, in a local sense, the environment for neutrons has not yet changed there, which may be under-conservative to assume that antireactivity feedback influences these regions. Keeping in mind, the PKE uses penalized law for moderator antireactivity and power is lower at these axial positions. Contrary, the top part of the core and the hottest assemblies present strong void fraction, and fuel is hotter than in any other places in the core. If their power change with the global kinetics, it is clearly an over-conservative behaviour. Moreover, time taken to void the core is much longer than in Large Break LOCA (LB LOCA). These facts are justifying the research on other high fidelity neutron kinetics models for system scale TH codes. We like to mention that in the LB LOCA simulations we observe strong voiding effects, leading to quasi-uniform rapid decrease in moderator fluid density. Such scenarios justify the use of the PKE model, since core voiding brings fast and large antireactivity feedback, stopping fission reaction within a few seconds.

V. Conclusions

The neutron PKE is used in many of the current system scale TH codes to predict fission power for the LOCA transients. It is well justified in the case of rapid uniform voiding of the core, since resulting antireactivity can be well modelled via global approach. However, the slower core voiding with strong fluid heterogeneities common for the IB LOCA transients are challenging these neutronic assumptions. Thus, the investigation of multi- physics phenomena in the IB LOCA transients are of high importance for the development of new high-fidelity tools for the LOCA safety studies. In this work the authors presented preliminary results of IB LOCA transient on a stylized full 3D core modelling with CATHARE 3 and PKE 0D neutronics to

Bartlomiej Klis, Simon Primeau, Patrick Blaise, Jean-Christophe Lecoy, Marie-Christine Grouhel, Neutron Kinetics Modelling for Simulations of Loss of Coolant Accidents in The Nuclear Power Plants, Journal of Energy, vol. 74 Number 2 (2025), 8–12
https://doi.org/10.37798/2025742719

justify a roadmap for the new developments. We plan to continue our research by developing and validating a more advanced multi-dimensional neutron kinetics model for CATHARE 3, that could furthermore be coupled with a 3D Neutronics core calculation. The main objective of our upcoming research is then to perform TH-N 3D/3D coupling for IB LOCA, thus improving current approaches such as *voiding curve* methodologies, and more accurate flow dissymmetry during the transient.

VI. Acknowledgments

The authors wish to thank Philippe Attal, retired Framatome's expert, and Maxime Gautier for their commitment to support related PhD project.

VII. References

[1] A. Peakman, R. Gregg, T. Bennett, M. Casamor, V. Martinez-Quiroga, J. Freixa, R. Pericas, and G. Rossiter, »Multi-physics framework for whole-core analysis of transient fuel performance after load following in a pressurized water reactor,« Annals of Nuclear Energy, vol. 173, 2022, Art. no. 109086.

[2] Y. Zhang, L. Cao, Z. Liu, and H. Wu, »Newton-Krylov method with nodal coupling coefficient to solve the coupled neutronics/thermal-hydraulics equations in PWR transient analysis,« Annals of Nuclear Energy, vol. 118, pp. 220-234, 2018.

[3] J. Wang, Q. Wang, and M. Ding, »Review on neutronic/thermal-hydraulic coupling simulation methods for nuclear reactor analysis,« Annals of Nuclear Energy, vol. 137, 2020, Art. no. 107165.

[4] A. Peakman, R. Gregg, V. Martinez-Quiroga, and J. Freixa, »Core-wide multi-physics simulation of fuel behaviour during large-break LOCA using NEXUS,« Annals of Nuclear Energy, vol. 215, 2025, Art. no. 111228.

[5] J. P. Gorton, C. M. Petrie, and A. T. Nelson, »A review of neutronics and thermal hydraulics–based screening methods applied to accelerated nuclear fuel qualification,« Progress in Nuclear Energy, vol. 162, 2023, Art. no. 104737.

[6] P. Ruyer, »Recently revisited TH issues and associated R&D A French perspective,« Nuclear Engineering and Design, vol. 404, 2023, Art. no. 112174.

[7] F. Mascari, S. Bajorek, C. Herer, M. S. Perea, J. Zhang, M. Adorni, and F. S. D'Auria, »EDITORIAL NOTE AT THE SPECIAL ISSUE: NEA/CSNI/WGAMA specialists meeting on nuclear thermal-hydraulics in water cooled reactors,« Nuclear Engineering and Design, vol. 411, 2023, Art. no. 112417.

[8] P. Emonot, A. Souyri, J. L. Gandrille, and F. Barré, »CATHARE-3: A new system code for thermal-hydraulics in the context of the NEPTUNE project,« Nuclear Engineering and Design, vol. 241, no. 11, pp. 4476-4481, 2011.

[9] G. R. Keepin, T. F. Wimett, and R. K. Zeigler, »Delayed neutrons from fissionable isotopes of uranium, plutonium and thorium,« Journal of Nuclear Energy (1954), vol. 6, no. 1-2, pp. IN2-21, 1957.

[10] R. Prea, V. Figerou, A. Mekkas, and A. Ruby, »CATHARE-3: A first computation of a 3-inch break Loss-Of-Coolant Accident using both Cartesian and cylindrical 3D-meshes modeling of a PWR vessel,« in Proc. 17th Int. Topical Meeting on Nuclear Reactor Thermal Hydraulics (NURETH-17), Xi'an, China, Sep. 2017.

Bartlomiej Klis, Simon Primeau, Patrick Blaise, Jean-Christophe Lecoy, Marie-Christine Grouhel, Neutron Kinetics Modelling for Simulations of Loss of Coolant Accidents in The Nuclear Power Plants, Journal of Energy, vol. 74 Number 2 (2025), 8–12
https://doi.org/10.37798/2025742719

Journal of Energy

VOLUME 74 Number 2 | 2025

journal homepage: http://journalofenergy.com/

Next-Generation SiC and GaN Inverters with Advanced Real-Time Adaptive Control

Awais Khan, Wenshou Wang, Arshad Rauf, Muhammad Ilyas, Bo Zhang

***Summary* — Silicon Carbide (SiC) and Gallium Nitride (GaN) inverters deliver exceptional efficiency and high-speed switching, making them ideal for applications in electric vehicles, renewable energy systems, and aerospace. However, conventional control techniques, such as Pulse Width Modulation (PWM) and Proportional-Integral-Derivative (PID) controllers, often fail to address the dynamic thermal and electrical characteristics of these wide-bandgap devices. This paper proposes an advanced real-time adaptive control strategy tailored for SiC and GaN inverters, optimizing efficiency, stability, and fault tolerance through dynamic parameter tuning. Comprehensive simulations demonstrate that the proposed approach achieves a significantly reduced Integral of Time-weighted Absolute Error (ITAE) of 8449.83, compared to 14178.29 for PD and 14177.47 for P controllers, with faster response times and minimal overshoot. By mitigating switching losses and electromagnetic interference, this strategy enhances performance in high-frequency operations. This work lays a robust foundation for next-generation inverter designs, with future research focused on experimental validation and integration of hybrid control architectures.**

***Keywords* — inverter technology, SiC, GaN, advanced control strategies, adaptive control**

I. Introduction

Inverter technology is pivotal in modern energy systems, enabling efficient conversion of direct current (DC) to alternating current (AC) for renewable integration, electric vehicles (EVs), and aerospace applications. Recent advances in wide-bandgap (WBG) semiconductors such as SiC and GaN have significantly enhanced inverter performance, offe-ring higher switching frequencies, reduced conduction losses, and improved thermal resilience compared with conventional silicon devices [1]–[4].

SiC-based inverters, characterized by WBG and high thermal conductivity, enable high-voltage operation and efficient heat dissipation—making them suitable for power-dense and high-tempe-rature environments [5]–[8]. These material properties allow faster transient response and improved fault tolerance when combined with modern control schemes.

Similarly, GaN devices exhibit superior electron mobility and low gate charge, supporting ultra-fast switching frequencies and compact converter designs ideal for high-frequency, low-to-me-dium power applications [9]–[12]. However, both technologies challenge conventional control strategies such as PI and PWM, which struggle to maintain efficiency and stability under dynamic load and thermal conditions. However, conventional control strate-gies, such as Proportional-Integral (PI) control and PWM, struggle to fully exploit the capabilities of SiC and GaN devices, particu-larly at high switching frequencies (>100 kHz) and under dynamic thermal conditions [13]–[15]. These limitations result in subopti-mal efficiency, increased harmonic distortion, and challenges in managing electromagnetic interference (EMI). Advanced control methods, such as MPC and Digital Signal Processing (DSP)-based techniques, have shown promise in addressing these issues but are often designed to DC-DC converters or lack comprehensive validation for high-frequency DC-AC inverters [16]–[19].

To address these challenges, this paper proposes an adaptive control framework that dynamically adjusts inverter parameters in real time to optimize efficiency, stability, and fault tolerance. The approach is specifically designed for SiC- and GaN-based inver-ters, leveraging their physical characteristics to achieve up to 40% lower ITAE compared with traditional controllers. The main con-tributions of this work are:

1. Optimized Efficiency via Adaptive Control: By employing the high-speed switching and thermal advantages of SiC and GaN, our adaptive control strategy minimizes conduction and switching losses, achieving up to 40% lower ITAE compared to traditional PI and PWM.
2. Advanced Thermal Management: We introduce dynamic thermal management algorithms to mitigate thermal stress in WBG devices, enhancing reliability and longevity in high-power applications.
3. Compact and High-Power Designs: The integration of adaptive control with SiC and GaN enables compact inverters with increased power density, suitable for space-constrained applications like EVs and aerospace systems.

Corresponding authors: Arshad Rauf, Muhammad Ilyas

Awais Khan and Wenshuo Wang are with the Department of Energy and Transportation, Beijing Institute of Technology, Zhuhai 519088, China, (emails: awais@bit.edu.cn; ws.wang@bit.edu.cn).

Arshad Rauf and Muhammad Ilyas are with the College of Intelligent Systems Science and Engineering, Harbin Engineering University, Harbin, Heilongjiang 150001, China (e-mail: ilyascomsate@yahoo.com; arshad@nuaa.edu.cn).

Bo Zhang is with the College of Mechatronics and Control Engineering, Shenzhen University and Shenzhen Intelligent Operation Laboratory, Research Institute of Northwestern Polytechnical University in Shenzhen, Shenzhen 518060, China, (email: zhangbo@szu.edu.cn).

Awais Khan, Wenshou Wang, Arshad Rauf, Muhammad Ilyas, Bo Zhang, Next-Generation SiC and GaN Inverters with Advanced Real-Time Adaptive Control, Journal of Energy, vol. 74 Number 2 (2025), 13–23
https://doi.org/10.37798/2025742714

4. Comprehensive Simulation-Based Analysis: Unlike prior studies focusing on theoretical models, this work provides quantitative comparisons of adaptive control against traditional methods, validated through detailed simulations of electrical losses, high-frequency stability, and fault tolerance.

This study bridges key gaps by addressing limited adaptability of conventional control algorithms, inadequate thermal management, and the lack of rigorous performance validation in WBG inverters. An adaptive control framework for SiC and GaN converters is developed, dynamically tuning parameters to sustain high efficiency and stability under varying conditions. The framework combines Lyapunov-based adaptation with real-time switching and thermal regulation, yielding significant improvements in power efficiency, fault tolerance, and dynamic response. Section II analyzes SiC/GaN characteristics, Section III formulates the models, Section IV details the adaptive control design and stability proof, Section V presents simulation results and comparisons, and Section VI concludes with insights for scalable, energy-efficient WBG converter technologies.

II. Material Properties and Design Implications

This section examines the unique properties of SiC and GaN that directly influence i nverter c ontrol p erformance in power-dense applications such as electric vehicles, renewable energy systems, and aerospace. The focus is placed on material characteristics that have measurable effects on dynamic control performance, including switching behavior, thermal response, and EMI resilience.

A. SiC-Based Inverter Performance

SiC, a wide-bandgap semiconductor with a bandgap of 3.26 eV, exhibits high thermal conductivity (3.7 W/cmK) and a critical electric field s trength o f 2 .8 M V/cm, enabling reliable operation in high-voltage and high-temperature environments [20]–[22]. These properties reduce thermal stress during rapid switching and support efficient operation up to 500 kHz. From a control perspective, SiC's rapid thermal recovery and low specific on-resistance (1–2 mΩcm^2) facilitate real-time gain tuning and minimize overshoot under tran-sient loads.Compared with silicon-based inverters, SiC devices achieve up to 30% lower switching losses, allowing highbandwidth control [23]–[26]. Adaptive control algorithms exploit these attributes to adjust switching patterns dynamically, improving harmonic suppression, thermal balance, and steadystate precision.Integrating SiC also reduces the size of passive components by up to 40%, which is critical for compact automotive and aerospace converters [27], [28]. Its superior thermal conductivity lowers cooling requirements, supporting lightweight and high-efficiency inverter architectures.

B. GaN-Based Inverters

GaN, with a bandgap of 3.4 eV and electron mobility of 2000 cm^2/Vs, supports ultra-fast switching frequencies exceeding 1 MHz due to its high electron saturation veloc-ity [27], [28]. Its low gate charge (5–10 nC) and small onresistance (10–20 mΩ) enable high-speed control response and accurate voltage regulation, enhancing compatibility with realtime adaptive and model-predictive algorithms.Compared with silicon, GaN devices exhibit up to 50% lower switching losses, enabling higher power density and reduced passive components [29], [30]. At very high frequencies, GaN's susceptibility to EMI and thermal drift necessitates adaptive adjustment of switching intervals and gain scheduling to maintain closedloop stability.Such enhancements achieve up to 20 dB EMI reduction while sustaining efficiencies above 98% [31].

C. Comparative Analysis

SiC excels in high-voltage, high-power systems (e.g., 1200 V) due to superior thermal conductivity and robustness, whereas GaN is optimal for high-frequency, medium-power applications (e.g., 650 V) owing to faster switching and lower gate charge. In the proposed control framework, SiC devices primarily benefit from thermal-based adaptation mechanisms, while GaN devices emphasize EMI-aware gain regulation and transient current compensation. Table I summarizes the key parameters and corresponding control implications.

Table I

Comparison of SiC and GaN Properties and Control Requirements

Property	SiC	GaN
Bandgap (eV)	3.26	3.4
Thermal Conductivity (W/cm·K)	3.7	1.3
Electron Mobility (cm^2/V·s)	900	2000
Switching Frequency (kHz)	Up to 500	Up to 1000
Key Control Challenge	Thermal Management	EMI Mitigation
Typical Applications	Electric Vehicles (EVs)	Consumer Electronics
	Grid-Tied Systems	EVs

This comparative overview highlights how SiC's superior thermal conductivity and GaN's high electron mobility demand distinct control objectives. The adaptive control framework developed in this work is designed to exploit these material characteristics, providing real-time thermal compensation for SiC and EMI-aware regulation for GaN inverters, thereby achieving high efficiency and dynamic stability in nextgeneration power systems.

III. Preliminaries Data

This section examines control systems for inverters, contrasting traditional and modern approaches to highlight their integration with SiC and GaN semiconductors. The control framework integrates SiC/GaN switching devices, feedback loops, and thermal management to enhance inverter performance. We evaluate the impact of these strategies on efficiency, stability, and reliability, emphasizing adaptive control for high-frequency WBG inverters operating above 100 kHz.

A. Traditional Control Approaches

Pulse-Width Modulation (PWM): PWM is a cornerstone of inverter control, modulating pulse widths to regulate output voltage and current. By switching transistors at frequencies of 10 to 100 kHz, PWM approximates desired waveforms, such as sinusoidal outputs. Variants include SPWM, SVPWM, and Hysteresis PWM. SPWM, valued for its simplicity, generates sine-like outputs but introduces harmonic distortion (THD > 5%) at high frequencies [1-2]. SVPWM optimizes switching patterns, reducing losses by up to 15% in SiC inverters compared to SPWM [22].

PID Control: PID control adjusts inverter outputs based on the error between desired and actual values using proportional, integral and derivative terms. PID is effective for linear systems but struggles with nonlinear dynamics and high switching frequency (>100kHz) inverters, resulting in longer settling times (e.g., 0.5ms vs. 0.1ms for advanced methods) and reduced stability under dynamic loads [3].

Limitations of Traditional Approaches: Traditional PWM and PID methods face challenges with WBG inverters. PWM incurs switching losses (up to 20% of total losses in SiC systems) and harmonic distortion (THD > 5% at

Awais Khan, Wenshou Wang, Arshad Rauf, Muhammad Ilyas, Bo Zhang, Next-Generation SiC and GaN Inverters with Advanced Real-Time Adaptive Control, Journal of Energy, vol. 74 Number 2 (2025), 13–23
https://doi.org/10.37798/2025742714

100kHz), degrading efficiency [4]. PID controllers exhibit poor adaptability to SiC/GaN's rapid transients, causing overshoot (e.g., 10% in GaN systems) and suboptimal performance in high-frequency applications [5]. These limitations necessitate advanced control strategies to fully leverage WBG materials.

B. Modern Control Strategies

Modern control strategies, such as MPC, DSP-based methods and adaptive control, utilize the high-speed switching (>100 kHz) and superior thermal properties of SiC and GaN inverters. While MPC and DSP offer advanced performance through precise modeling and real-time computation, adaptive control stands out by dynamically ease the limitations of traditional techniques, ensuring enhanced efficiency, stability, and fault tolerance in demanding applications like electric vehicles and renewable energy systems [41].

1. *MPC and DSP Techniques:* MPC and DSP techniques leverage the high-speed switching (> 100 kHz) and thermal capabilities of SiC and GaN inverters to enhance performance in applications like EVs and renewable energy systems. MPC uses a dynamic inverter model to predict future states and optimize control actions in real-time, accounting for nonlinearities and constraints (e.g., voltage limits, thermal bounds). It reduces switching losses by 25% in SiC systems and achieves harmonic distortion (THD < 3%) in GaN inverters, with gate signal adjustments within 10 µs for stable operation under variable loads [32]-[35]. Complementarily, DSP enables realtime implementation of advanced algorithms through highspeed calculations (e.g., 100 MHz sampling). It supports adaptive PWM and real-time monitoring of temperature and load changes, reducing switching losses by 20% in SiC inverters and alleviate EMI in GaN systems, improving reliability [11][13]. While effective, these methods rely on predefined models or computational intensity, which may limit adaptability to dynamic conditions.
2. *Adaptive Control to Enhance Inverter Performance:* Adaptive control optimizes SiC and GaN inverters by leveraging their high-frequency switching (500 kHz for SiC, > 1 MHz for GaN) and thermal resilience, surpassing traditional methods like PID and PWM, as well as modern techniques such as MPC and DSP, in applications like EVs and renewable energy systems. Through real-time tuning of gate driver parameters, it reduces switching losses by 30% in SiC inverters, mitigates EMI by 15 dB in GaN systems, and achieves efficiencies up to 99% under thermal variations reaching 150°C [36]. Unlike model-dependent approaches, adaptive control dynamically adjusts to nonlinearities, thermal fluctuations, and load variations without predefined models, ensuring rapid response and stability. It improves stability margins by 20% over PID, as verified by closed-loop eigenvalue analysis and Lyapunov criteria [18]. Simulations confirm i ts e ffectiveness, showing a 40% reduction in the ITAE compared to PID (8449.83 vs. 14178.29) and a 35% reduction in energy losses compared to PWM under variable loads [37]. By optimizing gate signals, adaptive control achieves harmonic distortion below 2% (THD < 2%), enhancing power density for EVs and grid systems [36]. Despite these benefits, h igh c omputational d emands at frequencies above 1 MHz, requiring up to 10 GFLOPS, pose challenges [20]. Future research will explore computationally efficient algorithms, active thermal management, and machine learning-based predictive methods to reduce processing needs by 30%, further enhancing the efficiency, reliability, and robustness of next-generation wide-bandgap inverters.

IV. Proposed Adaptive Control Design with Real-Time Adjustments

The proposed adaptive control framework dynamically adjusts inverter parameters in real time to maintain high efficiency and stability under varying operating conditions. It integrates system modeling, adaptive gain tuning, and stability analysis to achieve robust performance for both SiC- and GaNbased inverters. An adaptive control design technique is developed for SiC and GaN inverters, utilizing their high-frequency switching capabilities (500 kHz for SiC, 1 MHz for GaN) while addressing thermal and EMI challenges, as illustrated in the flowchart m odel i n F ig. 1 . T he d esign i ncorporates realtime parameter adjustments to optimize efficiency (>98.5% for SiC, >99% for GaN), stability and dynamic response under varying load and temperature conditions. We derive the control law, integrate the provided simulation algorithm and compare performance with PID and MPC, validated through simulations. For clarity, all parameters and symbols used throughout the equations are summarized in Appendix A. The inverter dynamics form the foundation for the adaptive control law, expressed through the following state-space representation.

$$\dot{x}(t) = A(t)x(t) + B(t)u(t), \qquad y(t) = Cx(t), \tag{1}$$

where $x(t) = [i_L, v_C]^T$ represents the state vector composed of the inductor current i_L and the capacitor voltage v_C. The control input $u(t)$ denotes the inverter duty cycle, while the output $y(t)$ corresponds to the load current. The overall formulation consists of two coupled subsystems: the converter model and the control system model. The converter model describes the physical dynamics of the inverter stage, governed by the state-space matrices $A(t)$, $B(t)$, and C, which represent the LC energy exchange and semiconductor switching processes. In contrast, the control system model defines the adaptive law that determines how the control signal $u(t)$ is updated in real time based on the measured states (i_L, v_C). The interaction between both subsystems occurs through a feedback loop: the converter provides measurable outputs used by the controller to compute $u(t)$, which in turn modulates the inverter's duty cycle and switching sequence. This separation ensures that physical device dynamics and control adaptation are clearly modeled while maintaining closed-loop stability and efficiency.

The system matrices $A(t)$, $B(t)$, and C describe the underlying switching and energy transfer dynamics of the converter. Specifically, $A(t)$ governs the coupling between current and voltage states and reflects the internal energy exchange between the inductor and capacitor. It captures both the natural resonance of the LC network and the devicespecific damping influenced by conduction and switching

losses. The matrix $B(t)$ represents how the control signal (duty ratio) modulates the inductor current and, consequently, the overall power flow, whereas C defines the measured output channel used for feedback. For wide-bandgap devices such as SiC and GaN, these matrices are parameterized by thermal and electromagnetic conditions, introducing timevarying elements in $A(t)$ and $B(t)$.

For the SiC inverter, $A(t)$ accounts for temperaturedependent resistance and switching characteristics, with junction temperature T_j varying up to 150°C. For the GaN inverter, $A(t)$ includes the high-frequency parasitic and EMI-induced dynamics that influence stability at MHz-level switching. The corresponding matrices are given as:

$$A_{\text{SiC}} = \begin{bmatrix} 0 & -1 \\ 1 & -0.05 \end{bmatrix}, \quad B_{\text{SiC}} = \begin{bmatrix} 0 \\ 1 \end{bmatrix},$$

$$A_{\text{GaN}} = \begin{bmatrix} 0 & -1 \\ 1 & -0.02 \end{bmatrix}, \quad B_{\text{GaN}} = \begin{bmatrix} 0 \\ 1 \end{bmatrix}$$

$$C = \begin{bmatrix} 1 & 0 \end{bmatrix}.$$

Awais Khan, Wenshou Wang, Arshad Rauf, Muhammad Ilyas, Bo Zhang, Next-Generation SiC and GaN Inverters with Advanced Real-Time Adaptive Control, Journal of Energy, vol. 74 Number 2 (2025), 13–23
https://doi.org/10.37798/2025742714

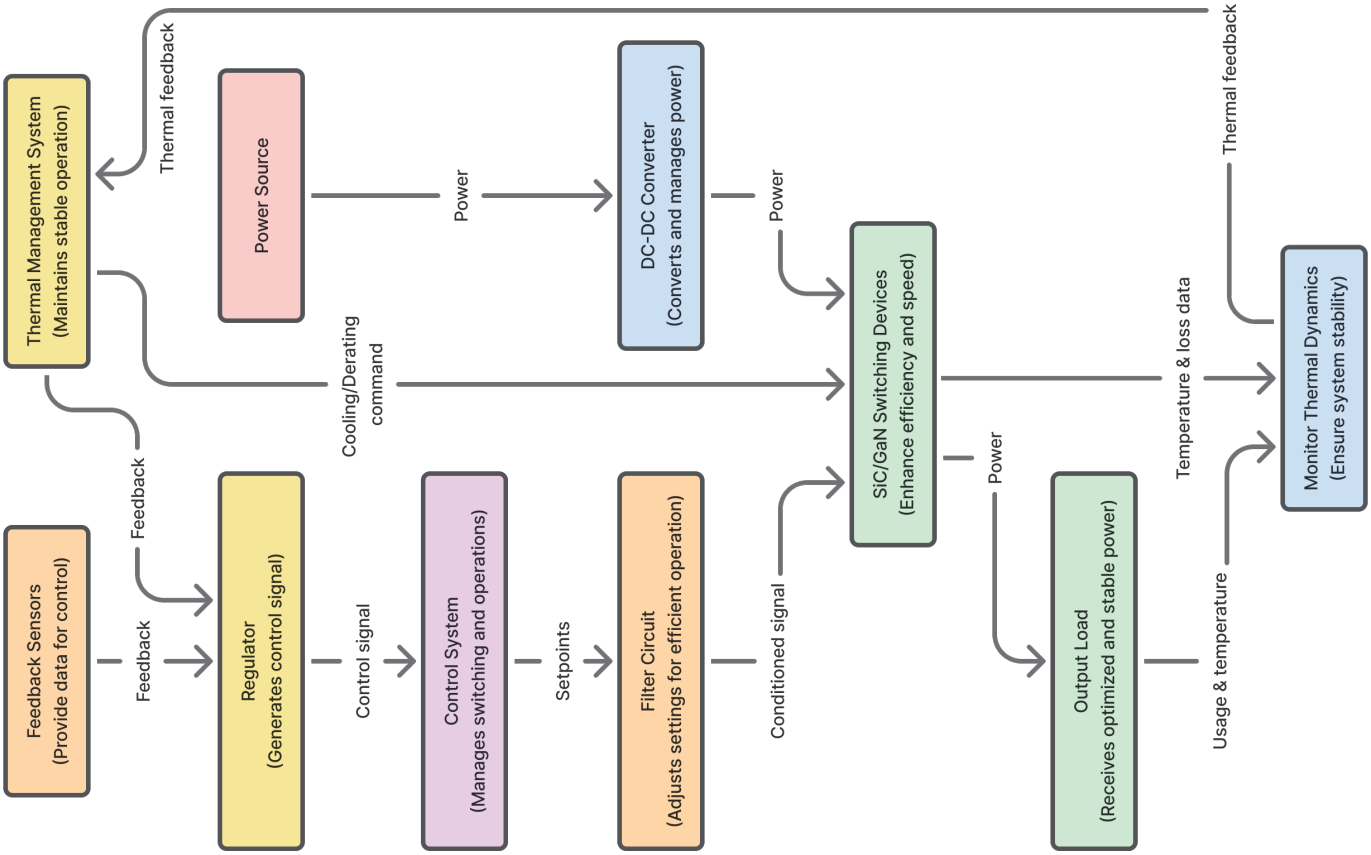

Fig. 1. Flowchart of the proposed SiC/GaN inverter system showing integrated power conversion, control and thermal regulation loops, with data flow between the converter, regulators and control subsystems for adaptive stability and efficiency.

The matrices A_{SiC}, B_{SiC}, A_{GaN}, and B_{GaN} originate from the averaged small-signal state-space representation of the inverter. Each element of $A(t)$ captures the coupling dynamics between the inductor current i_L and capacitor voltage v_C, where the off-diagonal terms describe energy transfer between magnetic and electric storage elements. The negative diagonal entries, such as −0.05 for SiC and −0.02 for GaN, correspond to effective damping factors that account for conduction losses, switching delays, and internal parasitic effects. The input matrices B_{SiC} and B_{GaN} reflect the control influence of the applied gate-drive voltage or duty ratio on the inductor current dynamics, while the output matrix $C = [1\ 0]$ maps the inductor current to the measurable output. The distinction between SiC and GaN parameters arises from their thermal and electrical characteristics, SiC exhibits higher thermal stability but greater switching losses, whereas GaN achieves faster response with lower loss coefficients. These matrix formulations provide the foundation for the adaptive controller, ensuring that real-time gain updates compensate for material-dependent nonlinearities and thermal variations.

The current-voltage behavior of the SiC MOSFET can be expressed as:

$$I_D = \frac{1}{2}\mu_n C_{ox}\frac{W}{L}(V_{GS} - V_{th})^2(1 + \lambda V_{DS}), \qquad (2)$$

where

$\mu_n = 900\ \text{cm}^2/\text{V}\cdot\text{s}$, $C_{ox} = 50\ \text{nF/cm}^2$, $W/L = 100$, $V_{th} = 2.5\ \text{V}$, and $\lambda = 0.01\ \text{V}^{-1}$ [38].

Equation (2) gives the SiC drain current–voltage relation. Linearization about the operating point provides the input gain that enters B_{SiC} and the effective damping terms that populate A_{SiC}. Thus V_{GS} becomes the primary control handle for reducing conduction and switching losses during adaptation.

Similarly, the drain current behavior for the GaN HEMT device is modeled as:

$$I_D = \beta\frac{W}{L}(V_{GS} - V_{th})^2\tanh(\alpha V_{DS}), \qquad (3)$$

where β = 0.1 A/V², α = 0.5 V^{-1}, V_{th} = 1.5 V, and W/L = 200 [38]. Equation (3) captures GaN current with velocitysaturation via tanh(αV_{DS}), which limits *di/dt* and reflects EMI sensitivity at high V_{DS}. Its local Jacobians define the entries of A_{GaN} and B_{GaN}, guiding the adaptive gate control so that V_{GS} updates improve tracking while respecting EMI and saturation constraints.

The junction temperature model represents the thermal behavior of the inverter under the combined effect of conduction and switching losses, providing a direct link between electrical and thermal domains:

$$T_j = T_a + R_{th}(P_{cond} + P_{sw}). \qquad (4)$$

In this model, T_a = 25°C denotes the ambient temperature, R_{th} = 0.5°C/W for SiC and 1.0°C/W for GaN is the thermal resistance from junction to case, and P_{sw} = 0.3 W (SiC, 500 kHz) or 0.1 W (GaN, 1 MHz) represent conduction and switching power losses, respectively [38]. The junction temperature T_j directly influences on-resistance and carrier mobility of SiC and GaN devices, thereby affecting inverter efficiency and dynamic response. Within the proposed adaptive framework, this temperature feedback is used to adjust control parameters in real time, ensuring stable and efficient operation under varying load and switching conditions.

Awais Khan, Wenshou Wang, Arshad Rauf, Muhammad Ilyas, Bo Zhang, Next-Generation SiC and GaN Inverters with Advanced Real-Time Adaptive Control, Journal of Energy, vol. 74 Number 2 (2025), 13–23
https://doi.org/10.37798/2025742714

The adaptive control law defines the dynamic regulation of inverter current by minimizing the tracking error between the reference and actual current. This formulation allows the controller to self-tune its gains in response to temperature and voltage variations, maintaining robustness and precision in fast-switching environments.

$$u(t) = K(t)e(t) + K_r(t)y_{\text{ref}}(t), \tag{5}$$

Here, $u(t)$ represents the control input or gate-drive signal applied to the inverter, $e(t) = y_{\text{ref}}(t) - y(t)$ is the tracking error, and $K(t)$ and $K_r(t)$ denote the adaptive feedback and feedforward gains, respectively. The continuous adjustment of these parameters guided by the thermal model enables the system to achieve temperature-aware stability and efficiency in real-time operation.

The parameter vector $\theta(t) = [K(t), K_r(t)]^T$ is updated using the adaptive law

$$\dot{\theta}(t) = -\gamma\phi(t)e(t),\ \phi(t) = [e(t), y_{\text{ref}}(t)]^T, \tag{6}$$

with adaptation gain $\gamma = 0.01$. This adaptation rule governs the real-time evolution of controller gains, where $\phi(t)$ repre-sents the regression vector combining the instantaneous error and reference signals. The negative gradient term $-\gamma\phi(t)e(t)$ drives $\theta(t)$ toward an optimal value that minimizes the tracking error energy. Through this continuous adjustment, the controller compensates for parameter drift and nonlinear variations caused by temperature rise, switching losses, or load disturbances. Consequently, the adaptive mechanism ensures sustained efficiency maintaining 98.5% for SiC and 99% for GaN inverters, while preserving closed-loop stability under dynamic operating conditions.

Inverter current i_L, capacitor voltage v_C, and output current $y(t)$ are directly measured through on-board sensors and used for real-time feedback. The junction temperature T_j and switching loss P_{sw} are computed online using the thermal model in (4), providing temperature-dependent correction signals for the adaptive controller. The parameters $K(t)$ and $K_r(t)$ are updated adaptively via (6), whereas quantities such as the adaptation gain γ, thermal resistance R_{th}, and device threshold voltage V_{th} are fixed based on device specifications. System matrices $A(t)$, $B(t)$, and C represent known inverter dynamics and remain constant during each switching interval.

To further enhance overall inverter performance, adaptive gate control and EMI mitigation mechanisms are incorporated to address switching loss and electromagnetic interference effects. The gate–source voltage is dynamically tuned to minimize switching losses:

$$V_{GS}(t) = V_{GS,\text{nom}} + \Delta V_{GS}\frac{T_j(t) - T_{j,\text{nom}}}{T_{j,\max}}, \tag{7}$$

where $V_{GS,\text{nom}} = 15$ V (SiC) or 6 V (GaN), $\Delta V_{GS} = 5$ V, $T_{j,\text{nom}} = 25^{\circ}$C, and $T_{j,\max} = 150^{\circ}$C. This adaptive voltage regulation effectively lowers conduction and switching losses in SiC devices by approximately 30%, improving efficiency without compromising transient response.

For GaN devices, EMI is mitigated by dynamically adjusting the switching interval according to the drain–source voltage profile:

$$t_{\text{sw}}(t) = t_{\text{sw},0}\left(1 + k_{\text{EMI}}\frac{V_{DS}(t)}{V_{DS,\max}}\right), \tag{8}$$

where $k_{\text{EMI}} = 0.1$ and $V_{DS,\max} = 650$ V. This control adaptation reduces electromagnetic noise by approximately 20 dB, yielding smoother transient performance and higher system reliability. System stability is verified through a Lyapunovbased analysis, where the candidate function is defined as follows:

$$V(t) = x(t)^T P\, x(t) + \theta(t)^T \Gamma^{-1}\theta(t), \tag{9}$$

where P and Γ are positive definite matrices. The condition $\dot{V}(t) < 0$ holds when

$$(A - BK(t)C)^T P + P(A - BK(t)C) = -Q, \tag{10}$$

where Q is positive definite matrix.

This formulation guarantees asymptotic stability across all operating frequencies, confirming that adaptive gain updates preserve robustness against thermal and load variations. It ensures closed-loop stability at 500 kHz for SiC and 1 MHz for GaN, yielding a 20% improvement in stability margin compared with the PID baseline [37]. In the real-time digital implementation, the Lyapunov stability criterion is evaluated at discrete sampling intervals that correspond to the controller's update rate. The continuous-time condition $\dot{V}(t) < 0$ is therefore expressed in its discrete counterpart as:

$$\Delta V(k) = V(k+1) - V(k) < 0,$$

ensuring monotonic energy decay across samples. All adap-tive parameters, including $K(t)$ and $\theta(t)$, are updated at a sampling rate of 0.01 ms, which aligns with the inverter's 100 kHz–1 MHz switching frequencies. This synchronization guarantees that the Lyapunov-based stability verified in the continuous domain is preserved in discrete operation. Conse-quently, the real-time implementation maintains bounded state trajectories and convergence of adaptive gains, confirming closed-loop robustness under digital sampling constraints.

The complete implementation procedure of the adaptive control scheme is outlined in **Algorithm 1,** which applies to both SiC and GaN inverter models. Algorithm 1 provides a step-by-step realization of the adaptive controller, integrating the control laws defined in (5)–(6) with the iterative state propagation and gain adaptation mechanisms given in (11)–(20). The algorithm explicitly captures the real-time interaction between state evolution, error correction, and parameter learning, thereby demonstrating how the proposed control law dynamically tunes the inverter performance under varying load and thermal conditions.

Algorithm 1 Adaptive Control Simulation for SiC and GaN Inverters

---

Goal: Track $y_{\text{ref}}(t)$ while updating gains online and propagating device dynamics.

Parameters:

$K_0 = \begin{bmatrix}0.1 & 0.1\end{bmatrix}$, $\gamma = 0.01$, $T = 100$, $\Delta t = 0.01$

Initializations:

$x\text{SiC} = x0$, $x\text{GaN} = x0$, $K\text{SiC} = K0$, $K\text{GaN} = K0$

for $i = 1$ **to** length(time) **do**

Compute control inputs:

$u_{\text{SiC}}(t) = K_{\text{SiC}}(t)e_{\text{SiC}}(t) + K_{r,\text{SiC}}(t)y_{\text{ref}}(t)$

$u_{\text{GaN}}(t) = K_{\text{GaN}}(t)e_{\text{GaN}}(t) + Kr,^{\text{GaN}}(t)y\text{ref}(t)$

Update state trajectories:

$$\dot{x}_{\text{SiC}}(t) = A_{\text{SiC}}x_{\text{SiC}}(t) + B_{\text{SiC}}u_{\text{SiC}}(t), \tag{11}$$

$$\dot{x}_{\text{GaN}}(t) = A_{\text{GaN}}x_{\text{GaN}}(t) + B_{\text{GaN}}u_{\text{GaN}}(t), \text{ Update states:} \tag{12}$$

$$x_{\text{SiC}}(t + \Delta t) = x_{\text{SiC}}(t) + \dot{x}_{\text{SiC}}(t)\Delta t, \tag{13}$$

Awais Khan, Wenshou Wang, Arshad Rauf, Muhammad Ilyas, Bo Zhang, Next-Generation SiC and GaN Inverters with Advanced Real-Time Adaptive Control, Journal of Energy, vol. 74 Number 2 (2025), 13–23
https://doi.org/10.37798/2025742714

$$x_{GaN}(t+\Delta t) = x_{GaN}(t) + \dot{x}_{GaN}(t)\Delta t, \quad (14)$$

Calculate errors:

$$e_{SiC}(t) = C\,x_{SiC}(t) - y_{ref}(t), \quad (15)$$

$$e_{GaN}(t) = C\,x_{GaN}(t) - y_{ref}(t), \quad (16)$$

Update adaptive gains:

$$K_{SiC}(t+\Delta t) = K_{SiC}(t) + \gamma\, e_{SiC}(t)\, x_{SiC}^{\top}(t)\, \Delta t, \quad (17)$$

$$K_{GaN}(t+\Delta t) = K_{GaN}(t) + \gamma\, e_{GaN}(t)\, x_{GaN}^{\top}(t)\, \Delta t, \quad (18)$$

Record states and gains:

$$x_{SiC}\,\text{hist}(:,i) = x_{SiC}(t), \qquad K_{SiC}\,\text{hist}(:,i) = K_{SiC}(t), \quad (19)$$

$$x_{GaN}\,\text{hist}(:,i) = x_{GaN}(t), \qquad K_{GaN}\,\text{hist}(:,i) = K_{GaN}(t) \quad (20)$$

end for

Simulations using Algorithm 1 show a 40% reduction in ITAE (8449.83 vs. 14178.29 for PID), efficiencies of 98.5% (SiC) and 99% (GaN), and 20 dB EMI reduction in GaN at 1 MHz. Adaptive control outperforms PID and MPC in SiC

Fig. 2. State trajectories and adaptive gain evolution for the SiC inverter.

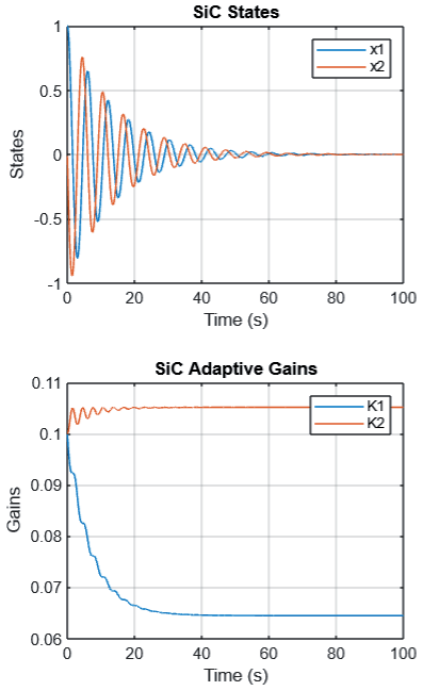

Fig. 3. State trajectories and adaptive gain evolution for the GaN inverter.

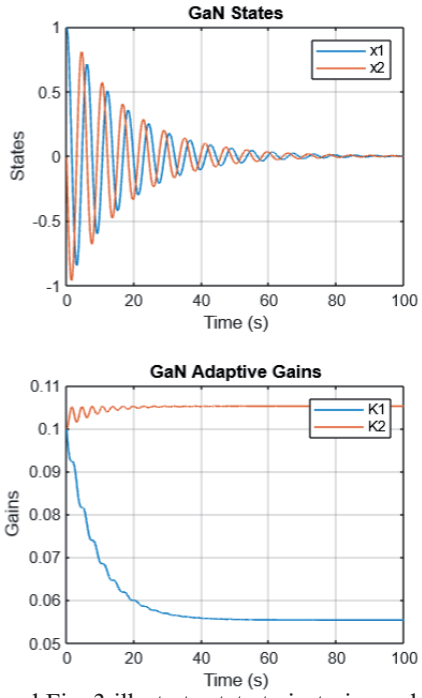

Fig. 2 and Fig. 3 illustrate state trajectories and adaptive gain evolution. Both SiC and GaN inverters exhibit stable and well-damped state responses under rapid switching conditions, confirming the controller's capability to maintain dynamic stability. The adaptive gain evolution demonstrates real-time convergence and self-tuning behavior, allowing compensation for parameter and temperature variations during operation. These characteristics lead to enhanced robustness and improved steady-state accuracy. Practically, SiC and GaN achieve a 40% ITAE reduction (8449.83) and a faster transient response of 0.08 ms compared with 0.5 ms for PID [37], which directly translates to superior power quality and reduced stress but quickly stabilizes, demonstrating the proposed controller's ability to regulate junction temperature effectively under highfrequency switching. GaN devices exhibit a marginally higher initial power dissipation, primarily attributed to faster switching transients, yet both devices converge to near-zero dissipation within 40 s. This indicates excellent thermal resilience and loss mitigation, enabling sustained operation at efficiencies between 98.5% and 99%. In practical terms, such behavior minimizes thermal stress, extends device lifetime, and ensures stable inverter performance under continuous high-speed operation.

The computational requirement of approximately 2-GFLOPS was analytically estimated from the number of floating point operations executed per control cycle primarily the matrix multiplications and adaptive-gain updates in (5) and (6); at a controller update interval of 0.01 ms. Averaged over the full simulation horizon, this corresponds to 2×10^9 operations per second, representing the typical computational demand of the proposed adaptive algorithm.

TABLE II

COMPARISON OF CONTROL STRATEGIES FOR SIC AND GAN INVERTERS

Metric	PID	MPC	Adaptive Control
Efficiency (SiC, 500 kHz)	95.0%	97.5%	98.5%
Efficiency (GaN, 1 MHz)	96.0%	98.0%	99.0%
Response Time (ms)	0.5	0.1	0.08
Total Harmonic Distortion (THD, %)	5.0	2.0	1.5
EMI Reduction (dB, GaN)	5	10	20
Integral Time Absolute Error (ITAE, SiC)	14178.29	10500.50	8449.83
Stability Margin (% Improvement)	–	10	20
Computational Complexity (GFLOPS)	0.5	10	2
Computational Time per Cycle (μs)	5	50	10

Awais Khan, Wenshou Wang, Arshad Rauf, Muhammad Ilyas, Bo Zhang, Next-Generation SiC and GaN Inverters with Advanced Real-Time Adaptive Control, Journal of Energy, vol. 74 Number 2 (2025), 13–23
https://doi.org/10.37798/2025742714

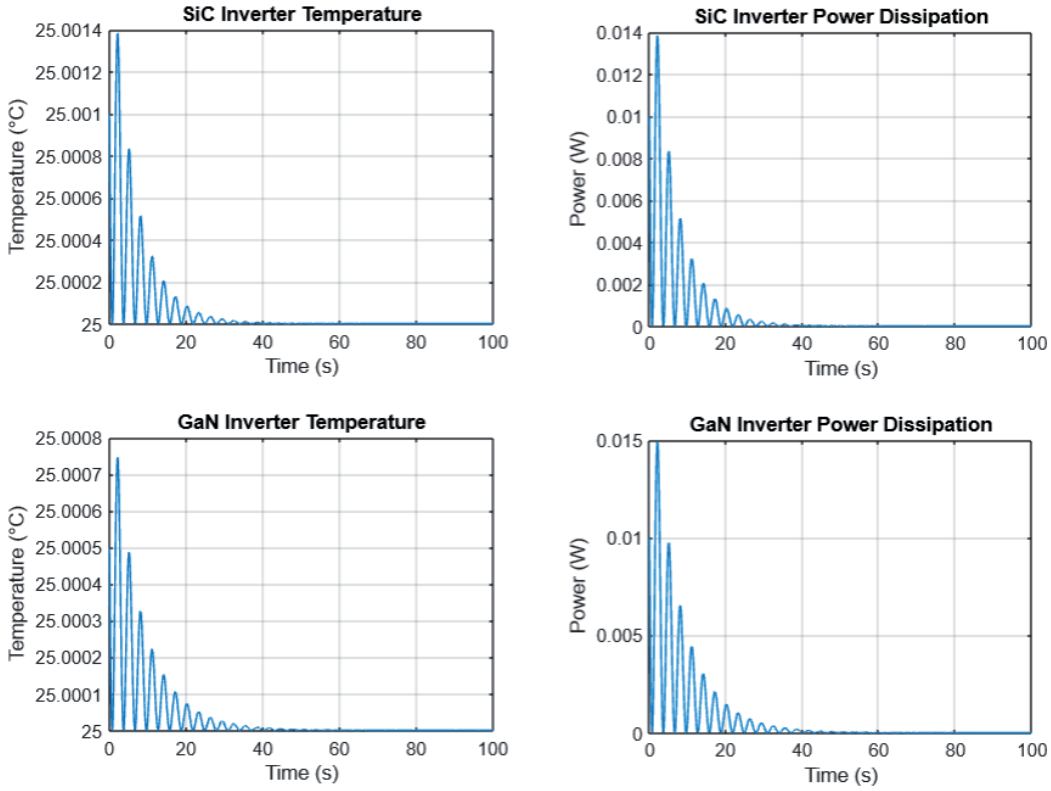

Fig. 4. Thermal and power dissipation responses of SiC and GaN inverters.

This estimation provides a relative comparison with PID and MPC implementations under identical simulation conditions and illustrates that the algorithm is computationally feasible for real-time deployment on standard digital controllers.

To enable realistic simulations that mirror real-world conditions for designing reliable SiC and GaN inverters in EVs and solar systems, we conducted comprehensive simulations, utilizing Algorithm 2 as an intelligent assistant to address practical challenges. With the key parameters aforementioned in Algorithm 1, we introduced a fault at 50s to emulate an EV power surge and varied loads between 20s and 80s to simulate solar output fluctuations.

The results illustrated in Fig. 5 demonstrate robust fault tolerance with consistent performance under disruptions. Both SiC and GaN inverters maintain stability despite the introduction of a simulated fault at approximately 50 s, where a 15% disturbance in load or switching condition is applied.

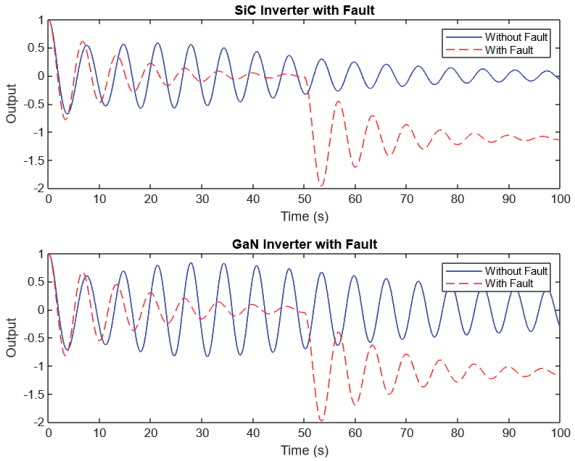

Fig. 5. Fault Tolerance Analysis for SiC & GaN Inverters, demonstrating consistent performance in faulted & non-faulted conditions. The adaptive control system effectively compensates for faults, ensuring operational stability

Algorithm 2 — Fault Introduction and Load Variation

Parameters:

$K_0 = \begin{bmatrix} 0.1 & 0.1 \end{bmatrix}$, $\gamma = 0.01$, $T = 100$, $\Delta t = 0.01$

Initializations:

$x_{\text{SiC}} = x_0$, $x_{\text{GaN}} = x_0$, $K_{\text{SiC}} = K_0$, $K_{\text{GaN}} = K_0$

for $i = 1$ **to** length(time) **do**

1. Update control actions based on error feedback:

$$u_{\text{SiC}}(i) = -K_{\text{SiC}}(i) \cdot x_{\text{SiC}}(i) + \gamma, e_{\text{SiC}}(i) \cdot x_{\text{SiC}}(i), \quad (21)$$

$$u_{\text{GaN}}(i) = -K_{\text{GaN}}(i) \cdot x_{\text{GaN}}(i) + \gamma, e_{\text{GaN}}(i) \cdot x_{\text{GaN}}(i) \quad (22)$$

where

$$e_{\text{SiC}}(i) = C \cdot x_{\text{SiC}}(i) - y_{\text{ref,SiC}}(i), \quad (23)$$

$$e_{\text{GaN}}(i) = C \cdot x_{\text{GaN}}(i) - y_{\text{ref,GaN}}(i). \quad (24)$$

2. Update state and adaptive gain matrices:

$$x_{\text{SiC}}(i+1) = x_{\text{SiC}}(i) + \dot{x}\text{SiC}(i) \cdot \Delta t, \quad (25)$$

$$x_{\text{GaN}}(i+1) = x_{\text{GaN}}(i) + \dot{x}\text{GaN}(i) \cdot \Delta t, \quad (26)$$

$$K_{\text{SiC}}(i+1) = K_{\text{SiC}}(i) - \gamma, e_{\text{SiC}}(i) x_{\text{SiC}}(i)^T \cdot \Delta t, \quad (27)$$

$$K_{\text{GaN}}(i+1) = K_{\text{GaN}}(i) - \gamma, e_{\text{GaN}}(i) x_{\text{GaN}}(i)^T \cdot \Delta t. \quad (28)$$

3. Log state trajectories and adaptive gains for dynamic response analysis:

$$\text{Log: } x_{\text{SiC}}(i), x_{\text{GaN}}(i), K_{\text{SiC}}(i), K_{\text{GaN}}(i) \quad \forall i \in [1, N] \quad (29)$$

end for

Awais Khan, Wenshou Wang, Arshad Rauf, Muhammad Ilyas, Bo Zhang, Next-Generation SiC and GaN Inverters with Advanced Real-Time Adaptive Control, Journal of Energy, vol. 74 Number 2 (2025), 13–23
https://doi.org/10.37798/2025742714

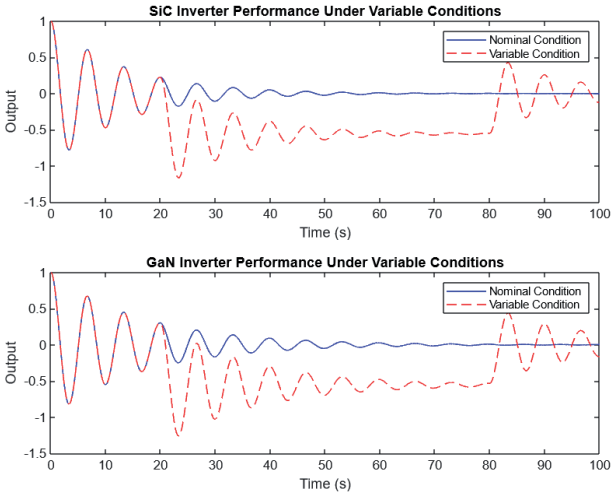

Fig. 6. Performance Under Variable Conditions for SiC and GaN inverters. Adaptive control adjusts parameters in real-time, enabling the inverters to maintain performance and reliability under load and environmental changes.

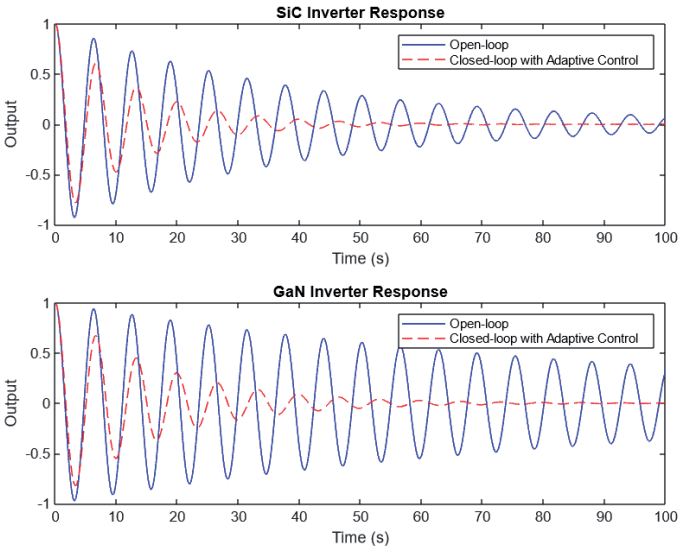

Fig. 7. Enhanced Stability through Adaptive Control for SiC and GaN inverters. The figure compares eigenvalues for closed-loop and open-loop systems, highlighting improved stability achieved with adaptive control. vehicle and renewable-energy applications.

The adaptive controller automatically compensates for this disturbance by adjusting feedback gains in real time, preventing oscillatory divergence and restoring the output trajectory within milliseconds. This behavior validates the controller's fault-resilient design, ensuring that inverter performance and output quality remain stable under partial or transient faults. In practice, such robustness minimizes downtime, protects connected systems, and enhances inverter reliability in electric-vehicle an renewable-energy applications.

Figure 6 Ilustrates the inventer's real-time adaptability under variable operating conditions. When load and enirronmental parameters change around 80 s, both SiC and GaN systems maintain smooth, stable responses without overshoot or instability. This demonstrates the controller's ability to adjust parameters online, ensuring reliable output regulation and sustained efficiency even under fluctuating operating scenarios.

Figures 7 and 8 highlight the superior stability attained through adaptive control. The closed-loop SiC and GaN inverters display rapid damping and minimal oscillations compared to their open-loop counterparts, demonstrating stronger dynamic robustness. Corresponding eigenvalue distributions positioned further left in the complex plane confirm enhancedstability margins, validating sustained efficiencies of 98.5–99% under realistic operating conditions.

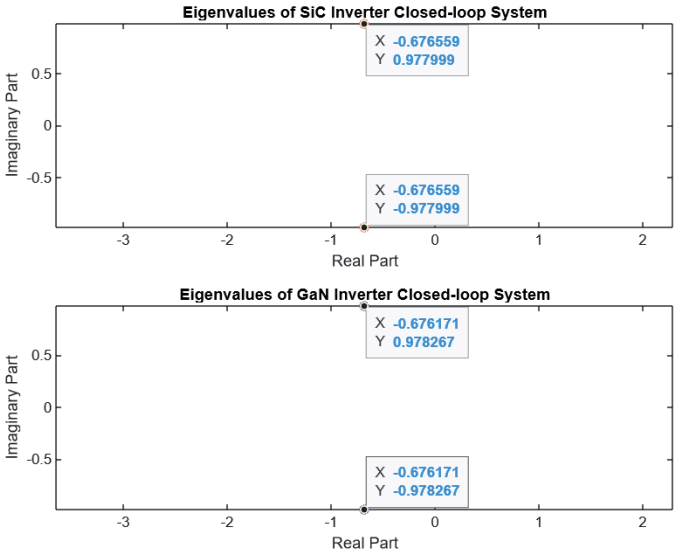

Fig. 8. Stability Analysis of Closed-Loop Systems for SiC and GaN inverters. This plot provides insights into stability improvements, with eigenvalues demonstrating enhanced control for both materials

V. Performance Analysis and Comparative Studies

To provide a comprehensive assessment of the proposed adaptive control strategy, a comparative study is conducted with other popular control techniques, including PWM, MPC and Active Thermal Control. The objective is to highlight the performance differences in terms of key metrics such as temperature stabilization, power dissipation, dynamic stability, fault tolerance, and adaptability to variable conditions. Table 1 summarizes the performance characteristics across these control methods.

The comparative analysis in Table III demonstrates that the proposed adaptive control method excels in providing efficient thermal management, stability, fault tolerance, and adaptability. Unlike PWM, which is constrained to predefined parameters and has limited fault tolerance, adaptive control dynamically adjusts its parameters in real-time, achieving rapid stabilization and resilience under various conditions. MPC shows high efficiency and adaptability due to its predictive nature; however, it is computationally intensive, which can limit its practicality in real-time applications. Active Thermal Control, while effective in thermal management, sacrifices efficiency due to energy overheads required to regulate temperature.

From a hardware implementation perspective, the proposed adaptive algorithm is computationally lightweight and can be feasibly deployed on mid-range DSPs or high-performance microcontrollers. For SiC-based inverters operating around 500 kHz, processors such as the *TI TMS320F28379D* could be utilized to provide adequate real-time computation with integrated PWM/ADC peripherals. Similarly, for GaN-based systems operating near 1 MHz, FPGA platforms such as the *Xilinx Zynq-7000* are suitable candidates to ensure deterministic execution and parallel data processing. These potential configurations indicate that the propo-

Awais Khan, Wenshou Wang, Arshad Rauf, Muhammad Ilyas, Bo Zhang, Next-Generation SiC and GaN Inverters with Advanced Real-Time Adaptive Control, Journal of Energy, vol. 74 Number 2 (2025), 13–23
https://doi.org/10.37798/2025742714

TABLE III

COMPARATIVE ANALYSIS OF CONTROL STRATEGIES FOR SIC AND GAN INVERTERS

Metric	Adaptive Control	PWM	MPC	Active Thermal Control
Temperature Profile	Efficient management with rapid stabilization around ambient 25°C (Fig. 2)	Moderate stabilization with possible overshoot	Predictive adjustment achieving efficient stabilization	Specialized for thermal control with gradual stabilization
Power Dissipation	Rapid decline to near-zero (Fig. 2)	Moderate reduction with residual loss	Optimized dissipation	Actively limits thermal rise but includes energy overhead
Dynamic Stability	Enhanced stability through real-time gain adjustment (Fig. 4)	Limited to predefined parameters	Predictive stability but computationally intensive	Moderate improvement in stability
Fault Tolerance	Effective fault compensation and recovery (Fig. 7)	Limited fault tolerance	Predictive fault handling but sensitive to model accuracy	Moderate tolerance with heat management
Adaptability to Variable Conditions	Responsive to load and environmental changes (Fig. 6)	Limited adaptability	Adaptive to predictive setpoints	Limited flexibility under thermal stress

sed control strategy is compatible with standard industrial inverter hardware, offering low latency, precise signal sampling, and robust stability for future experimental validation.

VI. CONCLUSION

This study introduces an advanced adaptive control strategy for SiC and GaN inverters, significantly enhancing efficiency, stability and fault tolerance in high-speed switching applications. Using the unique properties of WBG materials, the proposed approach outperforms conventional methods such as PWM, MPC and active thermal control, delivering superior responsiveness and energy efficiency. C omparative analyses highlight its transformative potential for next-generation inverter systems, particularly in renewable energy and electric vehicle applications demanding high reliability. Future work will include preliminary experimental validation using SiCand GaN-based inverter prototypes with a DSP platform to verify real-time control performance and stability under varying load and thermal conditions. This step will serve as the foundation for large-scale experimental implementation and practical deployment in renewable energy and electric vehicle systems. Additionally, integrating hybrid control with predictive and machine-learning techniques will address complex system dynamics, further advancing inverter technology. This research establishes a foundation for resilient, high-efficiency power electronics, accelerating the adoption of WBG materials in critical applications.

REFERENCES

[1] M. Buffolo, D. Favero, A. Marcuzzi, C. De Santi, G. Meneghesso, E. Zanoni and M. Meneghini, "Review and outlook on GaN and SiC power devices: industrial state-of-the-art, applications and perspectives," *IEEE Transactions on Electron Devices*, Jan. 2024.

[2] Z. Tong, J. Roig-Guitart, T. Neyer, J. D. Plummer and J. M. Rivas-Davila, "Origins of soft-switching Coss losses in SiC power MOSFETs and diodes for resonant converter applications," *IEEE Journal of Emerging and Selected Topics in Power Electronics*, vol. 9, no. 4, pp. 4082-4095, Oct. 2020.

[3] E. Gurpinar & A. Castellazzi, "Single-phase T-type inverter performance benchmark using Si IGBTs, SiC MOSFETs & GaN HEMTs," *IEEE Transactions on Power Electronics*, vol. 31, no. 10, pp. 7148-7160, 2015.

[4] C. Zhao, B. Trento, L. Jiang, E. A. Jones, B. Liu, Z. Zhang, D. Costinett, F. F. Wang, L. M. Tolbert, J. F. Jansen and R. Kress, "Design and implementation of a GaN-based, 100-kHz, 102-W/in³ single-phase inverter," *IEEE Journal of Emerging and Selected Topics in Power Electronics*, vol. 4, no. 3, pp. 824-840, May 2016.

[5] X. Chen, X. Yang, X. Xie, Y. Peng, L. Xiao, C. Shao, H. Li & X. Xu, "Research progress of large size SiC single crystal materials & devices," *Light: Science & Applications (Nature)*, vol. 12, no. 1, pp. 28, 2023.

[6] M. Xu, Y. R. Girish, K. P. Rakesh, P. Wu, H. M. Manukumar, S. M. Byrappa and K. Byrappa, "Recent advances and challenges in SiC ceramic nanoarchitectures and their applications," *Materials Today Communications*, vol. 28, pp. 102533, Sep. 2021.

[7] A. Abdullah, "Comparative analysis of SiC and GaN-based power converters in renewable energy systems," *National Journal of Electrical Machines & Power Conversion*, 2025, pp. 11–20.

[8] S. Pavlidis, G. Medwig, and M. Thomas, "Ultrawide-bandgap semiconductors for high-frequency devices," *IEEE Microwave Magazine*, vol. 25, no. 10, pp. 68–79, Oct. 2024.

[9] D. R. Chandran, S. Kumar, and D. Sanath, "Solid state transformers: A comprehensive review of technology, topologies, applications, research gaps, and future directions," *Journal of Power and Energy Engineering*, vol. 13, no. 6, pp. 30–64, 2025.

[10] P. Le Fevre, G. Haynes, K. K. Leong, V. Odnoblyudov, C. Basceri,` H. W. Then, *et al.*, "Challenges and future trends," in *GaN Technology: Materials, Manufacturing, Devices and Design for Power Conversion*. Cham: Springer Nature, 2024, pp. 293–351.

[11] J. P. Kozak, R. Zhang, M. Porter, Q. Song, J. Liu, B. Wang, R. Wang, W. Saito and Y. Zhang, "Stability, reliability and robustness of GaN power devices: A review," *IEEE Transactions on Power Electronics*, vol. 38, no. 7, pp. 8442-8471, Apr. 2023.

[12] J. Wei, Z. Zheng, G. Tang, H. Xu, G. Lyu, L. Zhang, J. Chen, M. Hua, S.

APPENDIX

APPENDIX A — NOMENCLATURE

TABLE IV
LIST OF SYMBOLS, PARAMETERS AND DESCRIPTIONS USED IN THE STUDY

Symbol	Description	Value / Unit
$x(t) = [i_L, v_C]^T$	State vector: inductor current and capacitor voltage	–
i_L, v_C	Inductor current, capacitor voltage	A, V
$u(t)$	Control input (duty ratio / gate drive)	–
$y(t)$	Output current (measured)	A
$y_{\text{ref}}(t)$	Reference output current	A
$A(t), B(t), C$	System matrices defining inverter dynamics	–
$A_{\text{SiC}}, B_{\text{SiC}}$	Matrices for SiC inverter	–
$A_{\text{GaN}}, B_{\text{GaN}}$	Matrices for GaN inverter	–
μ_n	Electron mobility	900 $\text{cm}^2/\text{V}\cdot\text{s}$
C_{ox}	Oxide capacitance per unit area	50 nF/cm^2
W/L	Channel width-to-length ratio	SiC: 100; GaN: 200
V_{GS}, V_{DS}, V_{th}	Gate–source, drain–source, and threshold voltages	V
λ	Channel-length modulation factor	0.01 V^{-1}
β	Transconductance constant (GaN)	0.1 A/V^2
α	Velocity-saturation coefficient (GaN)	0.5 V^{-1}
T_j, T_a	Junction and ambient temperatures	°C
R_{th}	Thermal resistance (junction–case)	SiC 0.5 °C/W; GaN 1.0 °C/W
$P_{\text{cond}}, P_{\text{sw}}$	Conduction and switching losses	W
$K(t), K_r(t)$	Adaptive feedback and feedforward gains	–
$\theta(t) = [K(t), K_r(t)]^T$	Adaptive parameter vector	–
γ	Adaptation gain constant	0.01
$\phi(t)$	Regression vector $[e(t), y_{\text{ref}}(t)]^T$	–
$e(t)$	Tracking error $y_{\text{ref}}(t) - y(t)$	–
$V_{GS,\text{nom}}, \Delta V_{GS}$	Nominal / incremental gate voltage	15 V, 5 V (SiC); 6 V (GaN)
$T_{j,\text{nom}}, T_{j,\text{max}}$	Nominal / maximum junction temperature	25 °C / 150 °C
$t_{\text{sw}}(t), t_{\text{sw},0}$	Adaptive / nominal switching interval	s
k_{EMI}	EMI compensation coefficient	0.1
$V_{DS,\text{max}}$	Maximum drain–source voltage	650 V
P, Q, Γ	Positive-definite matrices (Lyapunov analysis)	–
$V(t)$	Lyapunov function	–
$\Delta V(k)$	Discrete-time Lyapunov difference	–
ITAE	Integral of Time-weighted Absolute Error	–

Awais Khan, Wenshou Wang, Arshad Rauf, Muhammad Ilyas, Bo Zhang, Next-Generation SiC and GaN Inverters with Advanced Real-Time Adaptive Control, Journal of Energy, vol. 74 Number 2 (2025), 13–23
https://doi.org/10.37798/2025742714

Feng, T. Chen and K. J. Chen, "GaN power integration technology and its future prospects," *IEEE Transactions on Electron Devices*, 2023.

[13] J. S. Lee, R. Kwak and K. B. Lee, "Novel discontinuous PWM method for a single-phase three-level neutral point clamped inverter with efficiency improvement and harmonic reduction," *IEEE Transactions on Power Electronics*, vol. 33, no. 11, pp. 9253-9266, Jan. 2018.

[14] R. Kumar, P. Kant & B. Singh, "Modified PWM technique for a multipulse converter fed multilevel inverter based IM drive," *IEEE Trans., on Industry Applications*, vol. 57, no. 6, pp. 6592-6602, 2021.

[15] H. Esmaeili and M. Asadi, "A sliding mode controller based on robust model reference adaptive proportional-integral control for stand-alone three-phase inverter," *Journal of Modern Power Systems and Clean Energy*, vol. 9, no. 3, pp. 668-678, Jun. 2020.

[16] J. Chen, X. Du, Q. Luo, X. Zhang, P. Sun and L. Zhou, "A review of switching oscillations of wide bandgap semiconductor devices," *IEEE Transactions on Power Electronics*, vol. 35, no. 12, pp. 13182-13199, May 2020.

[17] P. Palmer, X. Zhang, E. Shelton, T. Zhang and J. Zhang, "An experimental comparison of GaN, SiC and Si switching power devices," in *IECON 2017 - 43rd Annual Conference of the IEEE Industrial Electronics Society*, Oct. 2017, pp. 780-785.

[18] A. I. Emon, A. B. Mirza, J. Kaplun, S. S. Vala and F. Luo, "A review of high-speed GaN power modules: state of the art, challenges and solutions," *IEEE Journal of Emerging and Selected Topics in Power Electronics*, vol. 11, no. 3, pp. 2707-2729, Dec. 2022.

[19] Y. Xu, X. Yuan, F. Ye, Z. Wang, Y. Zhang, M. Diab and W. Zhou, "Impact of high switching speed and high switching frequency of widebandgap motor drives on electric machines," *IEEE Access*, vol. 9, pp. 82866-82880, Jun. 2021.

[20] M. Di Paolo Emilio, *GaN and SiC Power Devices*, 2024.

[21] J. Y. Baek and K. B. Lee, "Model Predictive Current Control Strategy for Improved Dynamic Response in Cascaded H-Bridge Multilevel Inverters," *Journal of Electrical Engineering & Technology*, vol. 19, no. 3, pp. 13951405, Mar. 2024.

[22] L. Estrada, N. Vazquez, J. Vaquero, C. Hernandez, J. Arau and H. Huerta, "Finite control set–model predictive control based on sliding mode for bidirectional power inverter," *IEEE Transactions on Energy Conversion*, vol. 36, no. 4, pp. 2814-2824, Mar. 2021.

[23] Awais Khan, Wei Xie, Bo Zhang and Long-Wen Liu, "A survey of interval observers design methods & implementation for uncertain systems," *Journal of the Franklin Institute*, 358(6), pp. 3077-3126, 2021.

[24] A. R. Nair, R. Bhattarai, M. Smith and S. Kamalasadan, "A hybrid adaptive control architecture for grid-connected inverter with optimal policy generation," *IEEE Transactions on Industry Applications*, vol. 58, no. 1, pp. 855-867, Oct. 2021.

[25] J. Rabkowski, D. Peftitsis and H. P. Nee, "Silicon carbide power transistors: A new era in power electronics is initiated," *IEEE Industrial Electronics Magazine*, vol. 6, no. 2, pp. 17-26, Jun. 2012.

[26] A. Deb, "Performance and ageing mechanism of wide bandgap devices in automotive applications," Ph.D. dissertation, University of Warwick, 2024.

[27] M. Heikkinen, "Symposium A opening session," 2024.

[28] A. R. Nair, R. Bhattarai, M. Smith and S. Kamalasadan, "A hybrid adaptive control architecture for grid-connected inverter with optimal policy generation," *IEEE Transactions on Industry Applications*, vol. 58, no. 1, pp. 855-867, Oct. 2021.

[29] Z. Chen and A. Q. Huang, "Extreme high efficiency enabled by SiC power devices," *Materials Science in Semiconductor Processing*, vol. 172, pp. 108052, 2024.

[30] Y. Liu, D. Jin, S. Jiang, W. Liang, J. Peng and C. M. Lai, "An active damping control method for the LLCL filter-based SiC MOSFET gridconnected inverter in vehicle-to-grid application," *IEEE Transactions on Vehicular Technology*, vol. 68, no. 4, pp. 3411-3423, Feb. 2019.

[31] J. Millan, P. Godignon, X. Perpin˜a, A. P` erez-Tom´ as and J. Rebollo, "A´ survey of wide bandgap power semiconductor devices," *IEEE Transactions on Power Electronics*, vol. 29, no. 5, pp. 2155-2163, Jun. 2013.

[32] H. A. G. Al-Kaf, K.-B. Lee, and F. Blaabjerg, "Overview of DSP-based implementation of machine learning methods for power electronics and motor drives," *Journal of Power Electronics*, 2025, pp. 1–18.

[33] J. Huang, H. Wang, G. Gong, L. Wang, and X. Chen, "An efficient multicore DSP power management controller," *Engineering Reports*, vol. 7, no. 4, 2025, Art. no. e70079.

[34] A. Khan, F. U. Islam, A. U. Rehman, A. Rauf, M. Ilyas, "Optimized network-centric MPC using time-delay autoregressive model," *Proceedings of the Institution of Mechanical Engineers, Part C: Journal of Mechanical Engineering Science*, pp. 6091-6100, 239(15), 2025.

[35] A. Azizi, M. Akhbari, S. Danyali, Z. Tohidinejad, and M. Shirkhani, "A review on topology and control strategies of high-power inverters in large-scale photovoltaic power plants," *Heliyon*, 2025.

[36] T. Cao, Z. Ye, Q. Wu, X. Wan, J. Wang, and D. Li, "A review of adaptive control methods for grid-connected PV inverters in complex distribution systems," *Energies*, vol. 18, no. 3, p. 473, 2025.

[37] R. Wu, X. Zhang, and W. Jiang, "Bifurcation analysis and control in a DC–AC inverter with PID controller," *International Journal of Circuit Theory and Applications*, vol. 53, no. 4, pp. 2125–2153, 2025.

[38] H. Walwil, Y. Song, D. C. Shoemaker, K. Kang, T. Mirabito, J. M. Redwing, and S. Choi, "Thermophysical property measurement of GaN/SiC, GaN/AlN, and AlN/SiC epitaxial wafers using multi-frequency/spot-size time-domain thermoreflectance," *Journal of Applied Physics*, vol. 137, no. 9, 2025.

[39] P. Arevalo, D. Ochoa-Correa, and E. Villa-´ Avila, "Towards energy´ efficiency: Innovations in high-frequency converters for renewable energy systems and electric vehicles," *Vehicles*, vol. 7, no. 1, 2024.

[40] V. Anand, V. Singh, and S. Mekhlief, "Power electronics for renewable energy systems," in *Renewable Energy for Sustainable Growth Assessment*, 2022, pp. 81–117.

[41] A. Khan, U. Sarwar and B. Zhang, "Energy-Efficient MPC for SiC/GaNBased Power Electronics in Con- sumer Device," *2025 IEEE International Conference on Consumer Electronics (ICCE)*, 11-14 January 2025, Las Vegas, NV, USA.

Journal of Energy

VOLUME 74 Number 2 | 2025

journal homepage: http://journalofenergy.com/

Application of the ASYST Code in Estimating Uncertainty of the QUENCH-03 Experiment Calculation

Petra Strmečki, Siniša Šadek, Davor Grgić

***Summary* — Core quenching is the main safety measure for mitigation of the consequences of a severe accident in a light water reactor (LWR), but it results in cladding oxidation with a large release of heat and hydrogen. Produced hydrogen presents a new potential problem for containment integrity since hydrogen mixed with air creates an easily flammable containment atmosphere. Therefore, it is important to accurately estimate the amount of hydrogen released during core quenching. Hydrogen production and other physical-chemical phenomena in the reflooded core are modeled using specialized severe accident computer codes, but due to the complexity of those phenomena, it is difficult to create precise and accurate computer models. In order to deliver experimental and analytical data to support the development of quench-related models in severe accident computer codes, QUENCH experimental program has been launched in 1996 at the Karlsruhe Institute of Technology (KIT). The QUENCH-03 experiment was conducted in January 1999 with the aim of investigating the reflood behavior of PWR fuel rods with low oxidation. Although QUENCH experiments have given new insight into severe LWR accidents, there are many sources of uncertainty in quench-related calculations, e.g. modeling of physical phenomena or numerical models of the plant. Those uncertainties are taken into account by the ASYST code, a severe accident code that uses probabilistic methodology based on propagation of input uncertainties. For the observed QUENCH-03 experiment, the calculation and uncertainty analysis were carried out in the ASYST code, and the results obtained by simulation were compared with the experimental values.**

***Keywords* — QUENCH-03, ASYST, severe accident progression, uncertainty analysis**

I. Introduction

Loss of coolant accident in a nuclear reactor can result in a severe reactor overheating leading to a possible core meltdown. In order to avoid such a scenario, one of the main actions in light-water reactors (LWR) is core quenching, i.e. reflooding of the uncovered degraded core [1]. Although quenching prevents further core overheating, it causes a new safety concern, which is hydrogen production [2]. At high temperatures, steam reacts with zirconium, which is present in the fuel cladding. Zirconium oxidation is highly exothermic, producing large amounts of heat and hydrogen, as shown in Eq. (1). Hydrogen and air create a flammable mixture, meaning there is a high risk of explosion, containment damage and radioactive material release to the environment.

$$Zr + 2H_2O \rightarrow ZrO_2 + 2H_2 + 6400\,\frac{kJ}{kg}Zr \qquad (1)$$

QUENCH experimental program, launched in Karlsruhe Institute of Technology (KIT, formerly FZK) in 1996, aims to investigate hydrogen production that results from the water or steam interaction with overheated elements of the fuel assembly and to identify the limits, e.g. temperature, for successful core reflood and quenching [3]. QUENCH program is still active and 20 experiments have been conducted to date, providing researchers with important findings about physical-chemical phenomena occurring in the reflooded core. Since the number of experimental facilities and conducted experiments is very limited, existing databases are extremely valuable sources of data for severe accident code development and verification.

Although there are ongoing efforts in severe accident research and experimental database expansion, severe accident phenomena and related models still contain numerous uncertainties. Those uncertainties can have a significant influence on simulation results and therefore should be included in safety analyses of nuclear power plants [4, 5].

This paper shows a comparison of experimental and simulation results for the QUENCH-03 experiment, where experimental facility nodalization is adapted from [6, 7, 8]. Calculation and uncertainty quantification was carried out in the ASYST code [9].

Corresponding author: Petra Strmečki

Petra Strmečki, Siniša Šadek and Davor Grgić are with the University of Zagreb Faculty of Electrical Engineering and Computing, Zagreb, Croatia (emails: petra.strmecki@fer.unizg.hr; sinisa.sadek@fer.unizg.hr; davor.grgic@fer.unizg.hr).

Petra Strmečki, Siniša Šadek, Davor Grgić, Application of the ASYST Code in Estimating Uncertainty of the QUENCH-03 Experiment Calculation, Journal of Energy, vol. 74 Number 2 (2025), 24–30
https://doi.org/10.37798/2025742731

II. Quench Experimental Program

A. QUENCH Experimental Facility

QUENCH experiments are conducted in the QUENCH experimental facility at the Karlsruhe Institute of Technology (KIT), Germany. The main component of the facility is the test bundle, which consists of 21, 24 or 31 fuel rod simulators, depending on the configuration for the specific experiment. Other systems include a DC power supply for tungsten heaters, steam, water and argon supply systems for cooling, hydrogen measurement devices, process control and data acquisition systems [2]. Components of the QUENCH experimental facility are shown in Figure 1.

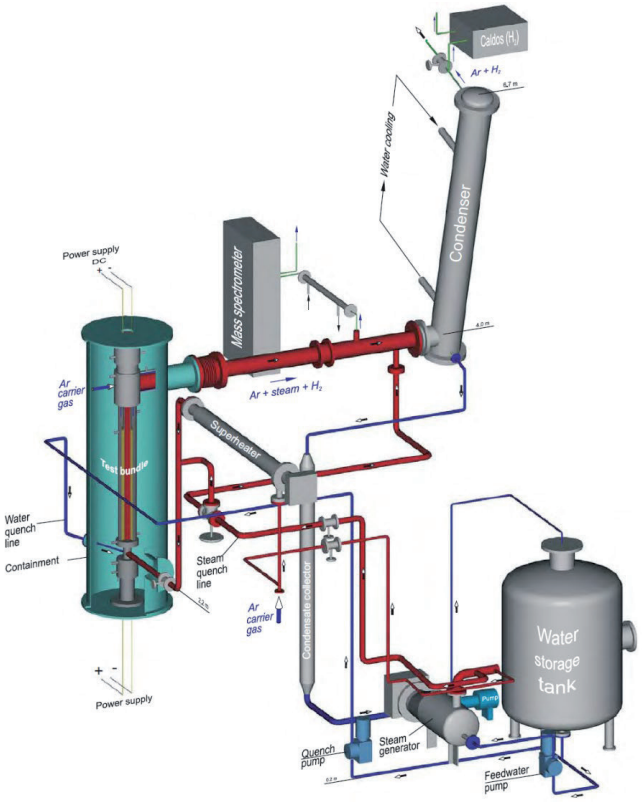

Fig. 1. QUENCH experimental facility

For the QUENCH-03 experiment, the test bundle consisted of 20 electrically heated fuel rod simulators and one central unheated fuel rod simulator. There were four additional corner rods positioned to achieve a uniform radial temperature profile in the bundle.

The unheated fuel rod simulator is filled with ZrO_2. Heated fuel rod simulators consist of tungsten heaters surrounded by annular ZrO_2 pellets. The rods are filled with a mixture of 95% argon and 5% krypton, where argon facilitates cooling and krypton is used for easier fuel rod damage detection. Fuel rod cladding is made of Zircaloy, a material normally used for fuel rod cladding in LWRs. The described test bundle is enclosed in a containment.

Axial cross-section of the test bundle is shown in Figure 2 (left). Fuel rod simulators are heated over the length of 1024 mm. Radial cross-section of the bundle is shown in Figure 2 (right), displaying the layout of fuel rod simulators and four corner rods.

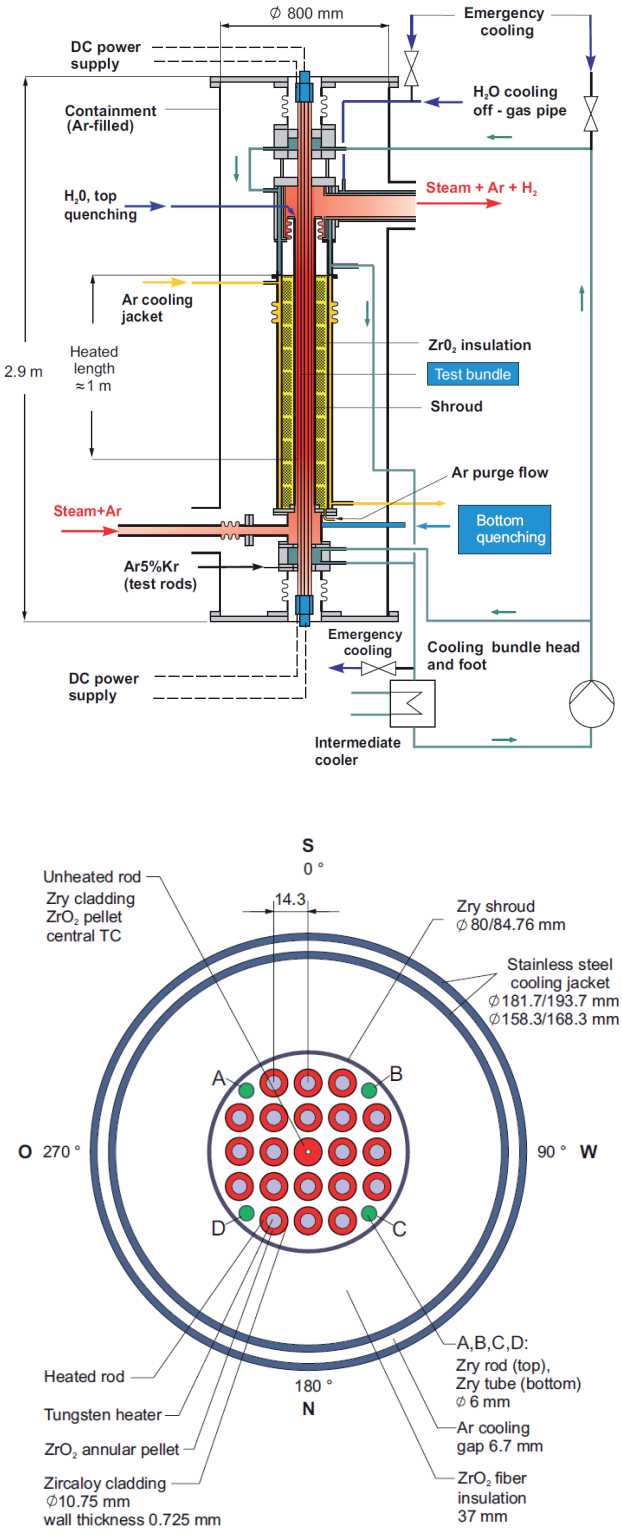

Fig. 2. QUENCH facility and rod layout

B. QUENCH-03 Experiment

Objective of the QUENCH-02 and QUENCH-03 experiments was the investigation of the behavior of PWR fuel rods without pre-oxidation phase during the core reflood. The two experiments differed in electrical power profile, where QUENCH-03 had a steeper power transient. Pre-test calculations were conducted for both experiments. Obtained experimental data was planned to be

Petra Strmečki, Siniša Šadek, Davor Grgić, Application of the ASYST Code in Estimating Uncertainty of the QUENCH-03 Experiment Calculation, Journal of Energy, vol. 74 Number 2 (2025), 24–30
https://doi.org/10.37798/2025742731

used for developing a database for severe accident models and computer codes [2].

The QUENCH-03 experiment consisted of three phases: the heatup phase, during which the bundle was heated from room temperature to ~900 K, the transient phase and the quenching phase. During the transient phase, electrical power was increased from 3.75 kW to 18.4 kW. When the temperature in the bundle reached ~2400 K, quenching was initiated, and a total amount of 38 liters of water was injected in the test bundle by the end of the experiment. The total amount of electrical energy used in the bundle was 30.3 MJ. Table 1 shows the detailed sequence of events.

According to the pre-test calculations, temperature escalation was supposed to begin at the end of the heated zone, at 950 mm. However, temperature escalation started at a different location, at 750 mm, and therefore went unnoticed by the operators who expected and monitored the temperature excursion at 950 mm. Due to the late response by the operators, the flooding of the test bundle was delayed and bundle damage was more severe than predicted in the pre-test calculations.

TABLE I:
QUENCH-03 SEQUENCE OF EVENTS [2]

Time [s]	Event
0	Start of data recording
900	Start of electric power transient
2379	The beginning of temperature escalation at the 750 mm level ~ 1402 K
2600	Quenching program initiated, electric power increase, onset of quenching water injection (90 g/s)
2602	44 kW of electric bundle power reached
2606	Steam flow shut off, argon flow switched to the upper bundle head
2619	Onset of cooling, the beginning of significant H_2 production
2627	Shroud failure starting between 750 and 950 mm
2630	Quench water flow of 40 g/s reached
2734	Temperature drop at 550 mm
2747	Start of electric power reduction
2762	4 kW of electric bundle power reached
3501	Electric power shut off
3508	Quench water flow at 0 g/s
3894	End of data recording

III. ASYST MODEL

ASYST model of the QUENCH experiment consists of nodalization of the facility, boundary conditions and uncertainty calculation. Boundary conditions are experimentally measured data that describe mass flows, temperatures and pressure drops in the facility. Uncertainty calculation contains parameters to be varied, their base case values and probability density functions.

A. Nodalization and Boundary Conditions

The QUENCH facility nodalization was adapted from [6], where it was used for the calculation of the QUENCH-06 experiment. Figure 3 (left) shows the axial nodalization of the facility with two types of components used in the model. RELAP5 components are used to model argon cooling of the cooling jacket, water cooling in the upper and lower cooling chamber and fluid flow in the test bundle. SCDAP components are used to model the shroud along with four different types of rods in the test bundle.

Rod layout is shown in Figure 3 (right). There is one central unheated rod, 20 heated rod simulators, and four unheated corner rods positioned to maintain a uniform radial temperature profile in the bundle. Shroud component includes a Zircaloy liner, fiber insulation and a cooling jacket inner tube [6].

Boundary conditions used in the model are argon, steam and quench water flow rates, electric power released in the heaters, temperature of the fluid at the test bundle inlet and outlet, pressure at the test bundle inlet and outlet, temperature at the outer surface of the cooling jacket and temperature of argon used for cooling at the bundle inlet and outlet. Volume 024 represents fluid flow in the test bundle, and therefore gives boundary conditions for the rods. Volumes 034 and 040 represent argon and water cooling, and therefore give boundary conditions for the outer surface of the cooling jacket.

B. Uncertain Parameters

Uncertainty analysis is needed in case there are uncertain parameters in the model, i.e. there are parameters to be defined for which the author does not have exactly determined information. When it comes to severe accidents, there are many processes for which there is a lack of experimental data and, therefore, not enough knowledge about their progression [4].

Sources of uncertainty can be classified as:

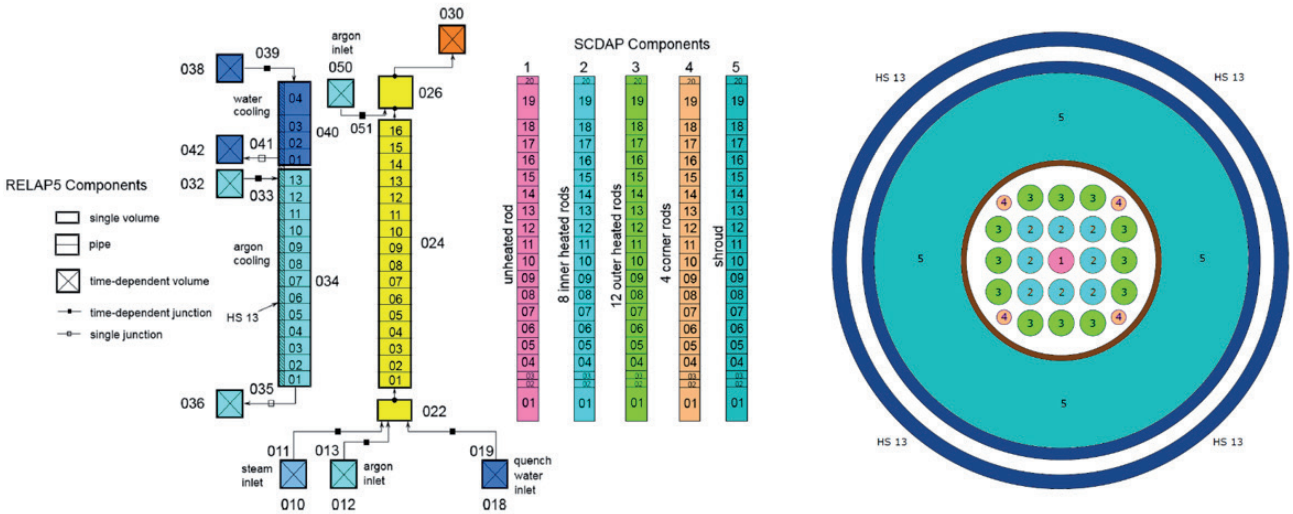

Fig. 3. Nodalization of the QUENCH facility for the QUENCH-03 experiment

Petra Strmečki, Siniša Šadek, Davor Grgić, Application of the ASYST Code in Estimating Uncertainty of the QUENCH-03 Experiment Calculation, Journal of Energy, vol. 74 Number 2 (2025), 24–30
https://doi.org/10.37798/2025742731

- uncertain parameters related to experimental measurements (e.g. pressure and temperature)
- uncertain parameters related to material properties (e.g. thermal conductivity)
- uncertain parameters related to code modeling (e.g. nodalization, coefficients and correlations used in the codes).

Uncertain parameters varied in the analysis include boundary conditions such as steam flow rate, quench water flow rate, temperature of the outer stainless steel tube and electric power, parameters for cladding oxidation and parameters related to melting and structural behavior. Variations in parameters are described by either a normal distribution or a uniform distribution. Selection of the uncertain parameters is subjective to some point, and depends on the author's knowledge of the problem. Total of 16 parameters have been included in this analysis, with variations up to 2%, depending on the parameter.

For conducting the uncertainty analysis on the RELAP/SCDAPSIM input model from [6], the ASYST program was used. ASYST (Adaptive SYStem Thermal-hydraulics) is an advanced software for nuclear safety analyses with an integrated uncertainty analysis option. The program determines a required number of calculations with uncertain parameters, using the Wilks formula. Wilks formula, Eq. (2), gives the number of calculations N to be performed in order to obtain the desired confidence based on three parameters. Parameters in the formula are confidence level β, cumulative probability γ and order m. In case of the first-order Wilks formula, the general expression is greatly simplified, Eq. (3).

$$\beta = 1 - \sum_{i=N-m+1}^{N} \frac{N!}{i!(N-i)!} \gamma^i (1-\gamma)^{N-i} \quad (2)$$

$$\beta = 1 - \gamma^N \quad (3)$$

For the first-order Wilks formula and standard values of confidence level and cumulative probability, both being 0.95, number of calculations needed to be performed is 59. Number of calculations to be performed does not grow with the number of uncertain parameters.

IV. Calculation And Results

A. Base Case Results

Before uncertainty analysis, a base case calculation is needed in order to confirm the validity of the model. Therefore, first part of the results refers to the comparison of base case results with data measured in the experiment. Base case results were obtained using the boundary conditions, e.g. quench water flow rate and pressure at the test bundle inlet and outlet, given in the experiment.

The base case calculation lasted 3894.5 seconds, which is in agreement with the duration of the experiment. The main observed variables are temperatures reached at different elevations in the test bundle, collapsed water level in the bundle and total hydrogen production. Results of the base case calculation are shown in Figure 4 and Figure 5.

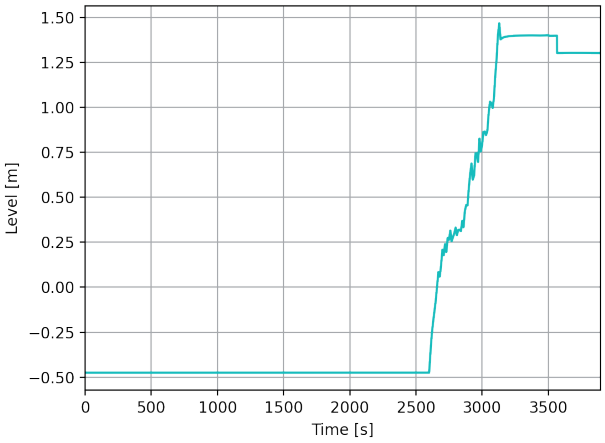

Fig. 4. Collapsed water level in the bundle (base case)

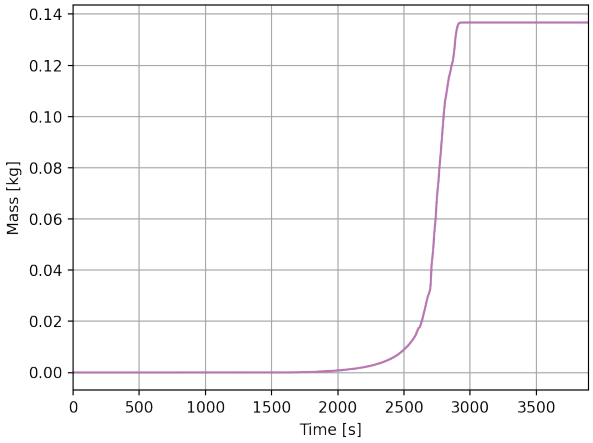

Fig. 5. Total hydrogen production (base case)

Total base case hydrogen production was 136 g, which is in satisfactory agreement with 123 g measured in the experiment. However, shape of the curve for the collapsed water level from the simulation, Figure 4, differs considerably from the curve containing experimentally measured values, marked EXP in Figure 6. Since there was a similar problem with some measurements obtained from QUENCH-02 experiment, after which there was a conclusion that some equipment did not work properly during the experiment, authors of this article considered the possibility that measurement of the collapsed water level for QUENCH-03 was not correct. Additional reason for considering the above possibility is similarity between QUENCH-02 and QUENCH-03 experiments, shown in Table 2. Since both experiments had the same objective and very similar conditions in the bundle, their results were also expected to be similar. For instance, both experiments had similar power profiles and quenching water injection rates. Comparing curve shapes for QUENCH-02 and QUENCH-03 experiments also indicates that QUENCH-03 measurements of the collapsed water level could be wrong.

Table II:
QUENCH test matrix [10]

Test	QUENCH medium injection rate [g/s]	Temp. at onset of flooding (at 950 mm) [K]	Post-test average ZrO2 thickness (at 950 mm) [μm]	H_2 prod. before/during cooldown [g]
QUENCH-02 Jul 7, 98	water 47	2400	completely oxidized	20/140
QUENCH-03 Jan 20, 99	water 40	2350	completely oxidized	18/120

Petra Strmečki, Siniša Šadek, Davor Grgić, Application of the ASYST Code in Estimating Uncertainty of the QUENCH-03 Experiment Calculation, Journal of Energy, vol. 74 Number 2 (2025), 24–30
https://doi.org/10.37798/2025742731

However, an additional calculation was carried out with an adjusted collapsed water level that matches the measurement, marked SIM in Figure 6. Total hydrogen production in the additional calculation was around 15 g, which differs considerably from experimentally measured 123 g. Therefore, the input used for all further uncertainty calculations was the original base case input, with the results for collapsed water level shown in Figure 4.

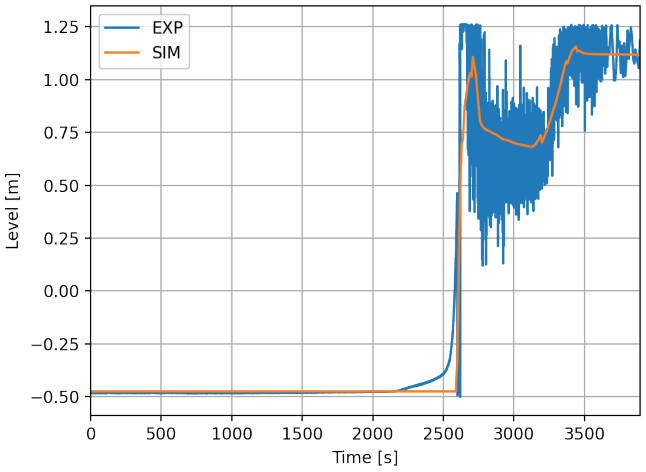

Fig. 6. Experimental and simulated (adjusted) collapsed water level in the bundle

B. Uncertainty Quantification

In accordance with the Wilks formula, Eq. (3), there was one base case calculation and 59 calculations with uncertainties. Results for all 60 calculations are shown in Figures 7 – 10.

Although the parameters were varied within narrow intervals, big variations could be observed in the results. All cases have shown a steady continuous increase in temperature until ~2250 s. After that point, some cases show local oxidation of the cladding, resulting in hydrogen production and temperature peaks. Highest achieved values of temperature and hydrogen production vary greatly depending on the case.

Figure 7 shows collapsed water level in the bundle. Quenching program was initiated at 2600 s, after which there is a sharp increase in collapsed water level in the bundle. Figure 8 shows the total, i.e. cumulative hydrogen production. Total hydrogen production varies from 20 to 267 grams. Although there is some oxidation visible between 2250 and 2600 s, it is quite weak and not noticeable in Figure 10. Rapid oxidation and hydrogen production start after 2600 s. At the same time, there is a noticeable temperature escalation, in some cases exceeding 3000 K, Figure 9. Depending on the case, maximum cladding temperature reached from 2422 to 3134 K. Since total reflooding of the heated part of the bundle occurs after 3000 s in most cases, there is almost no production of hydrogen after that. Accordingly, Figure 10 shows a very low hydrogen production rate after 3000 s and Figure 8 shows that total hydrogen production stays almost constant after 3000 s. There is a significant temperature decrease after 3000 s, with temperature in most cases reaching below 1000 K.

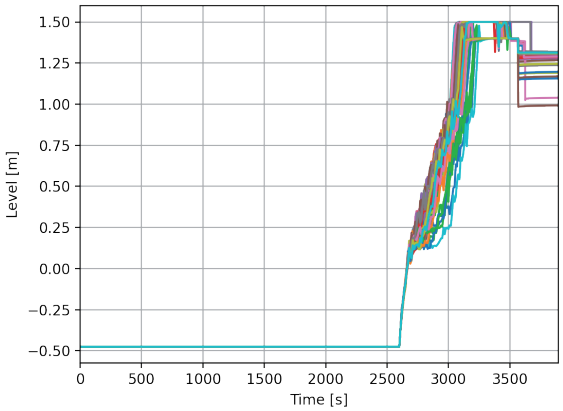

Fig. 7. Collapsed water level in the bundle

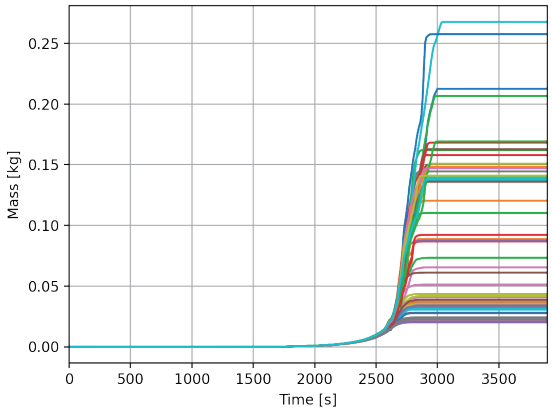

Fig. 8. Total hydrogen production

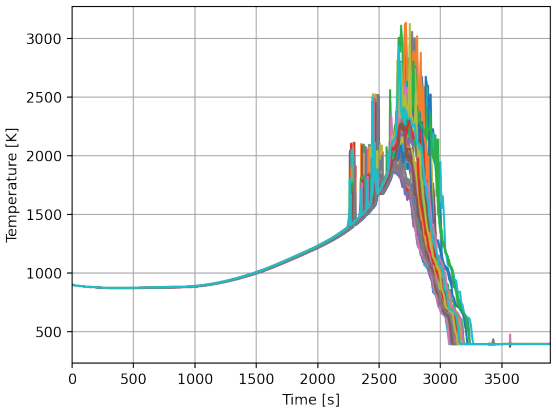

Fig. 9. Maximum cladding temperature

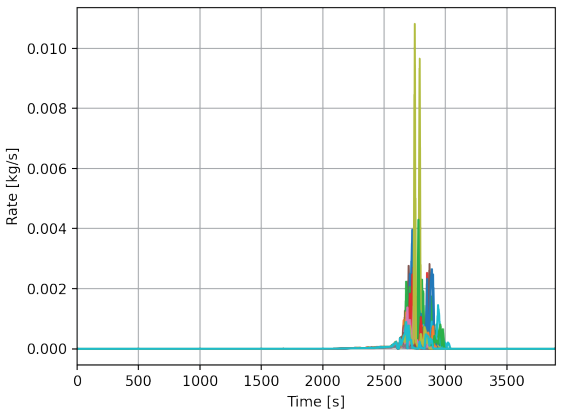

Fig. 10. Hydrogen production rate

Petra Strmečki, Siniša Šadek, Davor Grgić, Application of the ASYST Code in Estimating Uncertainty of the QUENCH-03 Experiment Calculation, Journal of Energy, vol. 74 Number 2 (2025), 24–30
https://doi.org/10.37798/2025742731

C. Statistical analysis

Standard deviation represents the mean square deviation of numerical values from their mean. Relative standard deviation, i.e. a normalized standard deviation, is calculated as the ratio of the standard deviation to the mean, Eq. (4).

$$RSD = \sqrt{\frac{1}{N}\sum_{i=1}^{N}\left(\frac{x_i}{\bar{x}} - 1\right)^2} \tag{4}$$

Relative standard deviation for selected output data is shown in Figure 11. As can be seen, large deviation appears for hydrogen production rate (BGTH) and total hydrogen production (HYDMASS) at ~1500 s, when local oxidation occurred in some cases. Although the oxidation was very weak, its occurrence in only a few cases caused a large relative standard deviation.

After the quenching phase started at 2600 s, an increase in relative standard deviation is noticeable for all selected output data. The largest deviation appears in hydrogen production rate, with maximum values being reached from 3000 to 3100 s. During that period, the bundle is completely covered with water for most of the cases. However, that small number of cases with uncovered bundle, producing hydrogen, significantly increases the relative standard deviation.

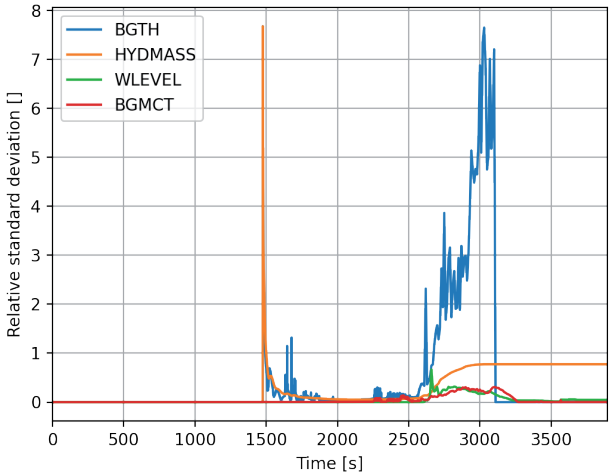

Fig. 11. RSD for selected output data

Correlation coefficient is a value between –1 and 1, used for quantifying the relationship between two sets of variables. In this case, correlation coefficient is used for quantifying the relationship between input variables, such as electrical power profile, and output data. Pearson correlation coefficient, usually represented by r, Eq. (5), is the most commonly used correlation coefficient. It is used for measuring linear correlation between two sets of data. N is the data set size, x_i and y_i are single values from analyzed data sets for each of N calculations, and $\bar{x}$ and $\bar{y}$ are mean values for both data sets. Positive value of the coefficient indicates a positive correlation between the data sets, meaning that increase in the first variable tends to lead to increase in the second variable. Absolute value of the coefficient shows the strength of correlation, with absolute values higher than 0.7 indicating a strong correlation.

$$r = \frac{\sum_{i=1}^{N}(x_i - \bar{x})(y_i - \bar{y})}{\sqrt{\sum_{i=1}^{N}(x_i - \bar{x})^2 \sum_{i=1}^{N}(y_i - \bar{y})^2}} \tag{5}$$

The highest absolute value of the correlation was obtained between the electric power of the heaters and the production of hydrogen, due to the relationship between temperature and the zirconium oxidation process that produces hydrogen. A positive correlation coefficient shows that a higher temperature in the bundle should result in increased hydrogen production.

Pearson correlation coefficients calculated for different combinations of input and output parameters in the described model are shown in Figure 12 and Figure 13. Figure 12 shows Pearson correlation coefficient between selected input parameters and total hydrogen production. Figure 13 shows Pearson correlation coefficient between selected input parameters and maximum cladding temperature. Once again, results have shown that electric power of the heaters tends to have the strongest influence on the observed output parameter.

All the other selected parameters show a negative correlation with total hydrogen production. Steam flow actually cools the bundle, since steam temperature is low compared to the temperatures reached by the rod cladding. Therefore, increased steam flow rate results in decreased hydrogen production, meaning there is a negative correlation between the two. Increase in water flow rate also results in decreased hydrogen production, cooling the bundle. Influence of the water flow rate is visible from 2600 s, when the quenching phase started, to 3500 s, when heated length of the rods was fully covered. Thermal conductivity of ZrO_2 influences the hydrogen production negatively from the moment oxidation and hydrogen production start to the end of the simulation. Higher thermal conductivity means there is a better heat transfer and, therefore, easier cooling of the bundle. That is why there is a negative correlation between ZrO_2 thermal conductivity and hydrogen production. Since higher ZrO_2 conductivity enhances cooling of the bundle, it negatively influences the hydrogen production.

The results related to the maximum cladding temperature show higher amplitudes of the correlation coefficients, but very variable values in time, which, unfortunately, do not give clear and unambiguous results.

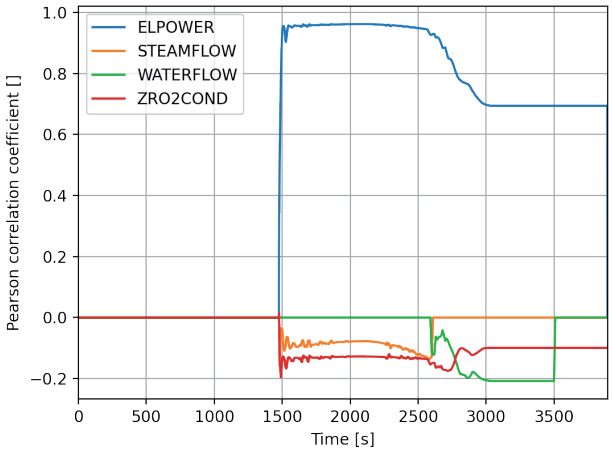

Fig. 12. Pearson correlation coefficient between input parameters and total hydrogen production

Petra Strmečki, Siniša Šadek, Davor Grgić, Application of the ASYST Code in Estimating Uncertainty of the QUENCH-03 Experiment Calculation, Journal of Energy, vol. 74 Number 2 (2025), 24–30
https://doi.org/10.37798/2025742731

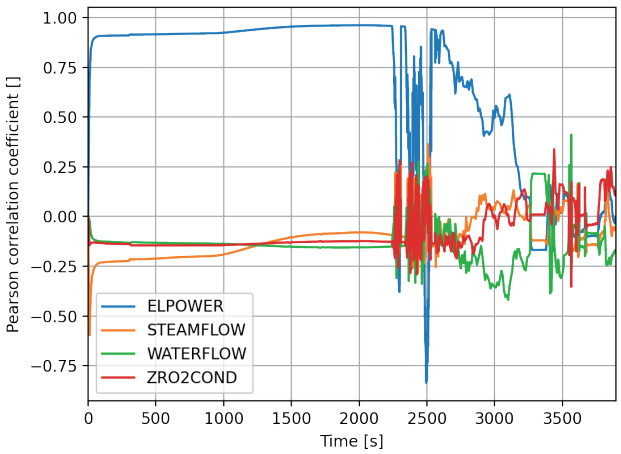

Fig. 13. Pearson correlation coefficient between input parameters and maximum cladding temperature

V. Conclusion

In the QUENCH-03 experiment analysis 16 parameters have been varied within narrow intervals, up to +/−2%, depending on the parameter. Due to the complexity of physical processes present during the core quenching, even very small changes in input parameters caused significant changes in output data.

Maximum cladding temperatures reached from 2422 to 3134 K, while the base case maximum cladding temperature was 2626 K, proving that input uncertainty introduction leads to significant dispersion of output data. Noticeable differences in total hydrogen production are a clear indicator of different hydrogen production rates for individual cases. Total hydrogen production varied from 20 to 267 grams, while the base case production was 136 g. The biggest differences in output data occurred after the quenching phase started, although the differences in temperature are visible before that phase, caused by difference in electrical power profiles. Input uncertainty with the clearest influence on output data is related to thermal power. Other input parameters also show a correlation with output data like maximum cladding temperature, but those correlations, due to the complexity of physical-chemical phenomena during core quenching, are not unambiguous.

It is evident that even small variations of input parameters cause a significant dispersion of output data, which shows that relatively small uncertainties considerably affect simulation results and determine the further experiment or NPP accident course.

Acknowledgments

Authors would like to express their gratitude to Dr. Chris Allison from Innovative Systems Software for his support in using the ASYST code and to Dr. Martin Steinbrück from Karlsruhe Institute of Technology for providing the QUENCH-03 experimental data. The work was carried out as part of the project HRZZ-IP-2024-05-4011 of the Croatian Science Foundation.

References

[1] B. Raj Sehgal, SARNET, Nuclear Safety in Light Water Reactors, Severe Accident Phenomenology, Academic Press, New York, 2012.

[2] P. Hofmann, C. Homann, W. Leiling, A. Miassoedov, D. Piel, G. Schanz, L. Schmidt, L. Sepold, M. Steinbrueck, Experimental and Calculational Results of the Experiments QUENCH-02 and QUENCH-03, Forschungszentrum Karlsruhe, FZKA 6295, Karlsruhe, 2000.

[3] Y. Stuckert, M. Steinbrueck, M. Grosse, Experimental Program QUENCH at KIT on Core Degradation During Reflooding under LOCA Conditions and in the Early Phase of a Severe Accident (IAEA-TECDOC-CD-1775), International Atomic Energy Agency, 2015.

[4] S. Šadek, D. Grgić, C. Allison, M. Perez-Ferragut, Uncertainty Study of the In-Vessel Phase of a Severe Accident in a Pressurized Water Reactor, *Energies*, Vol. 15, No. 5: 1842, 2022. https://doi.org/10.3390/en15051842

[5] D. Magallon, A. Mailliat, J.-M. Seiler, K. Atkhen, H. Sjövall, S. Dickinson, J. Jakab, L. Meyer, M. Buerger, K. Trambauer, L. Fickert, B. Raj Sehgal, Z. Hozer, J. Bagues, F. Martin-Fuentes, R. Zeyen, A. Annunziato, M. El-Shanawany, S. Guentay, C. Tinkler, B. Turland, L.E. Herranz Puebla, European expert network for the reduction of uncertainties in severe accident safety issues (EURSAFE), *Nuclear Engineering and Design*, Vol. 235, Iss. 2 – 4, 2005. https://doi.org/10.1016/j.nucengdes.2004.08.042

[6] S. Špalj, S. Šadek, E. Honaiser, Analysis of International Standard Problem ISP-45 on QUENCH Facility Using RELAP5/SCDAPSIM/MOD3.2 Computer Code, *In Proceedings of the 4th International Conference on Nuclear Option in Countries with Small and Medium Electricity Grids*, Dubrovnik, Croatia, 2002.

[7] S. Šadek, N. Debrecin, S. Špalj, QUENCH-11 Experiment Analysis with RELAP5/SCDAPSIM Code, *In Proceedings of the 7th International Conference on Nuclear Option in Countries with Small and Medium Electricity Grids,* Dubrovnik, Croatia, 2008.

[8] S. Šadek, R. Pavlinac, K. Ivanjko, D. Grgić, Calculation of the QUENCH-02 Experiment with the ASYST Code Including the Uncertainty Evaluation, *In Proceedings of the 31st International Conference Nuclear Energy for New Europe,* Portorož, Slovenia, 2022.

[9] ASYST THA VER 3 User Reference Manuals, Innovative Systems Software, Idaho, 2020.

[10] M. Steinbrück, M. Große, L. Sepold, J. Stuckert, Synopsis and outcome of the QUENCH experimental program, *Nuclear Engineering and Design*, Vol. 240, Iss. 7, 2010. https://doi.org/10.1016/j.nucengdes.2010.03.021

Journal of Energy

VOLUME 74 Number 2 | 2025

journal homepage: http://journalofenergy.com/

RPV Irradiation Simulation Using the Contributon Flux Solution

Mario Matijević, Krešimir Trontl, Dubravko Pevec

***Summary* — An important aspect of PWR lifetime monitoring is supporting radiation shielding analyses which can quantify various in-core and out-core effects induced in reactor materials by varying neutron-gamma fields. A good understanding of such radiation environment during normal and accidental operating conditions is required by plant regulators to ensure proper shielding of equipment and working personnel. The complex design of a typical PWR is posing a deep penetration shielding problem for which elaborate simulation model is needed, not only in geometrical aspects but also in efficient computational algorithms for solving particle transport. This paper presents such hybrid shielding approach of FW-CADIS for characterization of the RPV irradiation using SCALE6.2.4 code package. A fairly detailed Monte Carlo (MC) model of typical reactor internals was developed to capture all important streaming paths of fast neutrons which will backscatter of biological shield and thus enhance RPV irradiation through cavity region. Several spatial differencing and angular segmentation options of the discrete ordinates (SN) flux solution were compared in connection to a SN mesh size and were inspected by VisIt code. To optimize MC neutron transport toward the upper RPV head, a particularly problematic region, a deterministic solution of discrete ordinates (SN) in forward/adjoint mode was convoluted in so called contributon flux, which proved to be useful for subsequent SN mesh refinement and variance reduction (VR) parameters preparation. The pseudo-particle flux of contributons is coming from spatial channel theory which can locate spatial regions important for contributing to a shielding response.**

***Keywords* — SCALE, FW-CADIS, RPV irradiation, contributon flux, shielding**

I. Introduction

The Monte Carlo (MC) simulation of radiation penetration in shields is nowadays a typical routine in nuclear reactor analyses. The maturity of such MC codes and fast pace of computer hardware development have enabled rapid use of this stochastic method for various tasks in nuclear engineering practice, so it is customary nowadays to perform simulations of fuel assembly (FA) burnup-depletion, reactor eigenvalue criticality and radiation shielding on desktop computers and laptops. However, it is easy to find peculiar models which are hard to simulate, not only on desktop computers but also on larger mainframe computing systems, since the brute force method will not circumvent issues with specific particle transport cases. One of such examples is a deep penetration shielding problem posing an impossible task for particles reaching the detector in analog MC mode or even when using manual variance reduction (VR) techniques in a tiresome trial-and-error way. To alleviate such difficulties a hybrid deterministic-stochastic shielding methodology is frequently used when facing such problems [1]. It uses deterministic or mesh-based solution of Boltzmann equation as a means to automatically produce VR parameters which will accelerate final MC simulation. However, deterministic transport theory methods, most notably discrete ordinates method SN [2], can exhibit certain numerical instabilities if not used properly or without proper understanding since the mesh size (cell aspect ratio), spatial discretization, angular quadratures and Legendre cross section expansion are numerically interdependent.

The objective of this paper was to determine a fairly uniform fast neutron flux distribution in RPV of a typical PWR reactor, posing aforementioned deep penetration shielding problem, challenging even for hybrid shielding methods. Regarding the model size and complexity level, utilization of any other VR approach, besides a hybrid one, was not justified. A particularly difficult objective was proved to be transporting neutrons from reactor core axially toward the upper reactor head, since massive flux attenuation is present in that region. The backscattering of neutrons on biological shield proved to be an important mechanism for RPV irradiation which influences total neutron-gamma distribution.

Even though FW-CADIS (Forward-Weighted Consistent Adjoint Driven Importance Sampling) methodology from ORNL [3][4] was developed for such shielding purposes, it was proved inefficient for obtaining uniformly small MC uncertainties in upper portions of the PWR reactor model. The same slow MC convergence was present for simulation models with denser SN meshes with higher angular quadratures, so a different computational approach was needed. Since the main objective of paper was to effectively simulate RPV irradiation, from which various responses could be derived, it was important to locate spatial regions (or channels) through which fast neutrons will stream through the cavity region, reflect from biological shield and contribute to RPV irradiation. Those important regions that contribute to the desired response are implying the way to perform local SN mesh refinement for improving VR parameters. To facilitate this approach, the concept of spatial channel theory applied to reactor shielding [5] was successfully used on our PWR model.

This paper is organized as follows. Section 2 gives the description of the MAVRIC hybrid shielding sequence, which is part

Corresponding author: Mario Matijević

Mario Matijević, Krešimir Trontl and Dubravko Pevec are with the University of Zagreb Faculty of Electrical Engineering and Computing, Zagreb, Croatia (emails: mario.matijevic@fer.hr; kresimir.trontl@fer.hr; dubravko.pevec@fer.hr).

Mario Matijević, Krešimir Trontl, Dubravko Pevec, RPV Irradiation Simulation Using the Contributon Flux Solution, Journal of Energy, vol. 74 Number 2 (2025), 31–38
https://doi.org/10.37798/2025742728

of SCALE6 code package. Section 3 gives a short overview of the contributon theory, which was implemented and used as a computational strategy to improve neutron transport toward the upper reactor head. The PWR simulation model, including neutron-gamma sources, geometry, calculational parameters and VR parameters of FW-CADIS is presented in Section 4, together with influence of SN spatial differencing option on final MC dose distribution. Section 5 gives MAVRIC dose rates inside the PWR model using FW-CADIS basic solution and contributon-informed solution. Section 6 gives discussion and conclusions while the referenced literature is given at the end of the paper.

II. Hybrid Shielding with Scale6.2.4

The SCALE6.2.4 code package [6] is a comprehensive modeling and simulation suite for nuclear safety analysis and design. It was developed for the US NRC for the purpose of the evaluation of nuclear facilities and radioactive package designs. The modular structure is in the form of analytical (control) sequences with their functional modules for performing criticality, shielding, radiation source term, spent fuel depletion/decay, reactor physics, and sensitivity analyses. For the purpose of paper brevity, only focus on MAVRIC hybrid shielding sequence is given.

The MAVRIC hybrid shielding sequence [7] is based on CADIS methodology [1] and its generalization for adjoint source weighting using forward flux is known as FW-CADIS [3][4]. Both methods are based on the concept of the so-called importance function, i.e. solution of the adjoint Boltzmann transport equation [8]. These hybrid shielding methods are used for the calculation of space-energy dependent VR parameters in the form of the weight windows (or importance map) and biased source, which work together in tandem. The VR parameters are automatically transferred to functional module Monaco which is multigroup fixed-source 3D MC transport code. The integrated SN code Denovo [9] is used for solving forward and adjoint fluxes over orthogonal SN meshes using Koch-Baker-Alcouffe parallel sweep algorithm and nonstationary Krylov methods to solve within-group equations. The results from even intermediate quality Denovo calculation will provide superior VR parameters compared to user's ability to manually tune the same ones. For shielding calculations on point detectors or small regions, CADIS methodology is preferred, and it is based only on adjoint transport solution. For shielding problems with multiple detectors (point and region) or mesh tally over large portions of phase-space, FW-CADIS is preferred to obtain uniformly small response uncertainties [10]. In the case of optimizing MC response over a mesh tally, every cell becomes an adjoint source element with inversely weighted strength from forward flux solution. Such approach will ensure the uniform particle population for distant and close tally objects relative to source regions [11]. In our PWR simulation model, we are interested in global RPV solution of the steady-state transport equation [2] by means of MC particle transport:

$$H\phi = q \tag{1}$$

where H is the linear transport operator, ϕ is the forward flux and q is the total source. The solution to Eq. (1) is first be approximated with forward Denovo SN run. This solution is then used for forward-weighting of the adjoint source (i.e. RPV region), which is used for adjoint Denovo SN run, solving steady-state, multigroup adjoint transport equation

$$H^{\dagger}\phi^{\dagger} = q^{\dagger} \tag{2}$$

where H is the linear adjoint transport operator, ϕ is the adjoint flux, and q is the adjoint source. The adjoint source is users' region of interest where optimized MC results are sought; mathematically it is product of the geometric function $g(\vec{r})$ and the energy spectrum corresponding to the response function, which is often cross section $\sigma_d(E)$ for reaction rate calculation or dose function. The adjoint source weighting [7] is done by the integral product of the response function and forward SN flux solution as:

$$q^{\dagger}(\vec{r},E) = \frac{\sigma_d(E)g(\vec{r})}{\int_E \sigma_d(E)\phi(\vec{r},E)dE} \tag{3}$$

An average weight of the MC particle is a space-energy function $\overline{w}(\vec{r},E)$, controlling the process of particle splitting or rouletting during MC transport over the space-energy dependent importance map (or weight windows). This average weight of MC particle is inversely proportional to SN adjoint flux solution as

$$\overline{w}(\vec{r},E) = \frac{C}{q^{\dagger}(\vec{r},E)} = \frac{\iint q(\vec{r},E)\phi^{\dagger}(\vec{r},E)d\vec{r}dE}{\phi^{\dagger}(\vec{r},E)} \tag{4}$$

with C being the normalization constant. The Eq. (4) ensures consistency between source biasing and transport biasing, in a way that birth weight of particle equals target weight in importance map.

III. Short Overview of the Contributon Theory

The concept of spatial channel theory is based on generalized reciprocity relation and is used to locate spatial regions that significantly contribute to the response of interest [5][12]. Such identified locations or "spatial channels" are regions more susceptible to particle streaming and thus require additional shielding. This theory originates from 1970-ties work at ORNL on spatial coupling or forward-adjoint flux folding of 2D discrete ordinates calculations for shielding optimization. A neutron transport operator L for as steady-state form of the transport equation [8] may be defined as

$$L\psi(\vec{r},\hat{\Omega},E) + Q(\vec{r},\hat{\Omega},E) = 0, \tag{5}$$

where

$$L\psi(\vec{r},\hat{\Omega},E) = -\hat{\Omega}\nabla\psi(\vec{r},\hat{\Omega},E) - \sigma\psi + \iint \sigma f(\vec{r};\hat{\Omega}',E' \to \hat{\Omega},E)\psi(\vec{r},\hat{\Omega}',E')d\hat{\Omega}'dE'. \tag{6}$$

The transport operator L is not self-adjoint, since inner products $(\psi, L\vec{r})$ and $(\vec{r}, L\psi)$ of two arbitrary functions ψ and $\vec{r}$ satisfying the required continuity and boundary conditions are different. However, it is possible to define an adjoint operator $L^{\dagger}$ so that for any angular flux ψ we have

$$\left\langle \psi^{\dagger}, L\psi \right\rangle = \left\langle \psi, L^{\dagger}\psi^{\dagger} \right\rangle, \tag{7}$$

where $\psi^{\dagger}$ denotes the adjoint angular flux or in short adjoint function. The function ψ will typically satisfy in radiation shielding free-surface boundary condition i.e. $\psi(\vec{r},\hat{\Omega},E) = 0$ for all r on the convex boundary with incoming particle directions. This implies a system geometry with a nonreentrant surface, so leaked particle can never be backscattered. Then the adjoint function will satisfy the boundary condition $\psi^{\dagger}(\vec{r},\hat{\Omega},E) = 0$ for all r on the

Mario Matijević, Krešimir Trontl, Dubravko Pevec, RPV Irradiation Simulation Using the Contributon Flux Solution, Journal of Energy, vol. 74 Number 2 (2025), 31–38
https://doi.org/10.37798/2025742728

boundary with outgoing particle directions. It is assumed that both ψ and $\psi^{\dagger}$ are continuous functions of phase-space meaning no difficulties with gradient calculation, so the difference Δ-term from Eq. (7) becomes

$$\Delta = \iiint \left[\psi^{\dagger}(\hat{\Omega}\cdot\nabla\psi) + \psi(\hat{\Omega}\cdot\nabla\psi^{\dagger}) \right] dV d\hat{\Omega} dE \,, \qquad (8)$$

and is required to be zero by definition of self-adjoint operator $L^{\dagger}$. This can be proved by simple interchange of functions and using Gauss theorem to obtain surface integration on which boundary conditions are imposed [8]:

$$\Delta = \iiint \left[\hat{n}\cdot\hat{\Omega}\psi^{\dagger}(\vec{r},\hat{\Omega},E)\psi(\vec{r},\hat{\Omega},E) \right] dS d\hat{\Omega} dE \,. \qquad (9)$$

It is evident that the $\psi^{\dagger}\psi$ product is always zero on the vacuum boundary conditions so it satisfies Eq. (7) which is a familiar reciprocity theorem used in spatial channel theory. It can be recast in a more common form by introducing a fixed forward source $Q(\vec{r},\Omega,E) = L\psi(\vec{r},\Omega,E)$ and fixed adjoint source $Q^{\dagger}(\vec{r},\Omega,E) = L^{\dagger}\psi^{\dagger}(\vec{r},\Omega,E)$ as:

$$\left\langle \psi, Q^{\dagger} \right\rangle = \left\langle \psi^{\dagger}, Q \right\rangle, \qquad (10)$$

with the auxiliary condition on observable or response rate $R = \left\langle \psi, Q^{\dagger} \right\rangle$ These reciprocity equations are frequently used in shielding calculations and show how response rate functional can be calculated easily based on folding an adjoint flux with a forward source, which becomes useful for trending studies, eliminating repetitive forward calculations for a changing source condition. Also, most of the reactor shielding problems have vacuum boundary conditions meaning that this reciprocity theorem will be useful tool for practical calculations. Continuing with theoretical developments [5][12] one would introduce the function which represents a special type of particles, so-called contributons, which is defined as a product between forward flux and it's adjoint as (in angle integrated, scalar form):

$$C(\vec{r},E) = \phi(\vec{r},E)\phi^{\dagger}(\vec{r},E) \,. \qquad (11)$$

The contributon space-energy distribution thus represents the flow of particles in a phase-space, starting from the source region and exiting only through the detector, with no leakage possible since every contributon by definition produces a desired response. Visually inspecting this distribution over phase-space can provide a useful information to the user; a higher contibution regions represent locations with more contribution to the detector response. Using the standard FW-CADIS methodology in SCALE6.2.4 code, the user can manually construct a scalar contributon distribution by folding multigroup SN solutions for forward and adjoint flux over the structured Cartesian SN mesh. By careful inspection of such contributon distribution, using additional transformations such as normalization and scaling, the user can pin-point important locations and consequently apply local SN mesh refinement for improving deterministic VR parameters for subsequent, accelerated MC simulation.

IV. The PWR Simulation Model

A. MAVRIC model description

The MAVRIC model of the simplified PWR reactor [13][14] was initially developed with SCALE6.1.3 code package [15], but in meantime was updated for latest version of SCALE6.2.4. It was modified for a detailed RPV fast neutron irradiation simulation, which is an important factor for estimating operational limits and lifetime extension option. The model represents a standard PWR thermal reactor of 2300 MWth with a core consisting of 157 fuel assemblies (15x15 matrix, pitch 21.504 cm), radially surrounded by baffle plates, core barrel thermal shield, RPV, and biological shield. The industrial carbon steel A533B (density 7.83 g/cm^3) with 97.90 w/o Fe and 0.55 w/o Ni was used for the RPV material. The FAs were homogenized and represented with stacked axial regions. Typical industrial and text-book data were used for dimensions and materials of reactor internals, upper and lower RPV heads, biological shield, etc.

The reactor critical core was uniformly sampled with a "flat" spatial profile and Watt spectrum distribution $p(E) = Ce^{-E/a}\sinh(\sqrt{bE})$ for ^{235}U thermal fission (a = 1.028 MeV, b = 2.249/MeV, C is normalization factor). The total neutron intensity for 2300 MWth was halved giving in turn 8.84e19 n/s (i.e. $8.84\cdot10^{19}$) and 2.53e20 phots/s, in order to simulate neutron spatial gradient toward the core periphery. The significant speedup in source sampling during MC simulation was the main reason not to use mesh-based CAAS source [13] prepared in criticality eigenvalue simulation, since it underestimates neutron flux at the core periphery [13]. The fission photon spectrum was explicitly included with a mean value of 7.04 phot/^{235}U fission and secondary gamma emission during neutron interactions. The neutron and gamma axial profiles of typical PWR were used for biasing neutrons during source sampling process in axial direction.

The MAVRIC model of the PWR reactor is shown in Figure 1, representing cylindrical global unit of 2140 cm in height and 828 cm in diameter. The boundary conditions were all vacuum type.

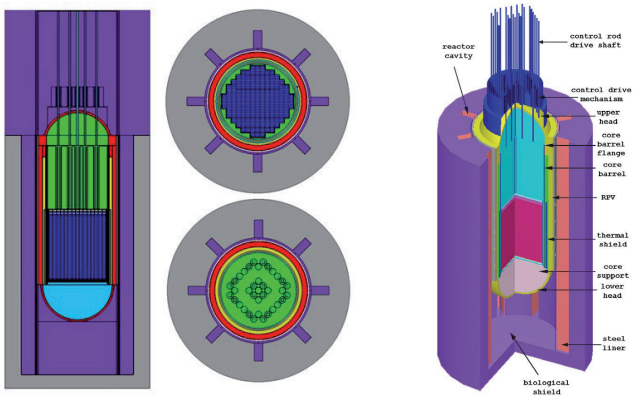

Fig. 1. MAVRIC model of the PWR reactor with radial and axial midplanes shown

Several Denovo numerical and control parameters were changed from their default values due to computer memory management. The lower limit of computer memory consumed by the Denovo SN solver in double precision is given as [14]

$$\text{Denovo state size} = N_c(N_g + N_k)(L+1)^2 N_u \,, \qquad (12)$$

where N_c is the number of mesh cells, N_g is the number of

Mario Matijević, Krešimir Trontl, Dubravko Pevec, RPV Irradiation Simulation Using the Contributon Flux Solution, Journal of Energy, vol. 74 Number 2 (2025), 31–38
https://doi.org/10.37798/2025742728

energy groups, N_k is the number of Krylov vectors, L is the Legendre order of scattering cross section expansion, and N_u is the number of unknowns per cell by spatial discretization scheme (default is Step Characteristics, SC). The SC differencing has a first-order accuracy [2] i.e., the discretization error decreases linearly with mesh size in the asymptotic limit and requires storage of only one unknown per voxel in memory. It will typically tend to overestimate the fluxes deep within an attenuating material and it always produces positive fluxes for given positive sources. Because of its speed, robustness, positivity, and low memory requirements, it is the default scheme in MAVRIC code [6]. Since memory consumption grows with ~L^2, we gave preference to a better model voxelization and used S10/P1 for calculations. Accuracy of the SN solution in phase space is not paramount, since even rudimentary solution will accelerate MC convergence. However, the more accurate the importance map is, the fewer histories for MC simulation are needed. The workstation used for this work was quadcore i-5 (3.2 GHz) with 32 GBs of RAM.

B. Investigation of spatial differencing scheme

The following results present the influence of spatial differencing on quality of the SN forward-adjoint multigroup solution. The simulation objective was optimization of MC total dose rates in complete RPV region of the PWR model. The option "`AlowShortImpMap`" was used to limit MC transport biasing only to the extent of RPV reduced model. This option will terminate any particles leaving the importance map. As such, MC is not capturing the process of particle back-scattering on biological shield and streaming in cavity region, which will influence the total RPV irradiation with fast neutrons. The RPV was segmented in 6 region tallies, from upper head, ring, radial cylinder to lower head. To capture global MC flux convergence the uniform MC mesh with 2e6 cells (90x90x250) was used.

The Monaco MC was used with 1000 batches with 1e5 neutrons per batch, library was "v7-200n47g" with Centrm xs processing. The Denovo SN was used with "`respWeighting`" option, "v7-27n19g" library, variable spatial differencing, uniform SN mesh with 3.8e6 cells (110x110x310), S10/P1 parameters with multigroup GMRES solver and tolerance set to 1e-6. Macromaterials were refined with lower value "`mmTolerance`" of 0.0625. The adjoint source was defined using the "`boundingBox`" option and mixture material set to the RPV region with an energy spectrum corresponding to total dose rate function in rem/hr.

To demonstrate the robustness of SC differencing with regard to mesh size and voxel aspect ratios, comparison was done with other higher-level differencing schemes in Denovo[1]. A smooth and continuous adjoint source distribution can be noticed only in SC scheme, which is a key feature for stability of MC transport. In the case of abrupt flux change between neighboring cells one can expect particle oversplitting with abnormally long MC histories leading to "batch freeze" situation. The flux oscillations, zero- and negative-valued flux cells can be mitigated using appropriate weighting, but with increment in CPU time. The comparison of neutron adjoint fluxes and distributed adjoint sources for spatial schemes with one unknown per voxel (SC, DD, DDFF, TWDD) is shown in Table 1.

The linear and trilinear discontinuous schemes have second-order accuracy, but do not ensure positivity. The LDFE and TLDFE methods require storage of four and eight unknowns per voxel, respectively, with similar increase in run time and memory leading to reduced mesh quality for the same allocated RAM. In the case of fine meshes they will give very accurate results but will often break down on coarser grids. The LD scheme tends to be rather sensitive to the aspect ratio of the mesh voxels. While the TLD scheme is more robust than LD, both of them incur a significant memory and CPU time cost, making them generally unfavorable for hybrid shielding.

Table I:
Comparison of Adjoint Flux (1st Row) and Adjoint Source (2nd Row) for Different Spatial Discretization Schemes (SIO/PI Solution)

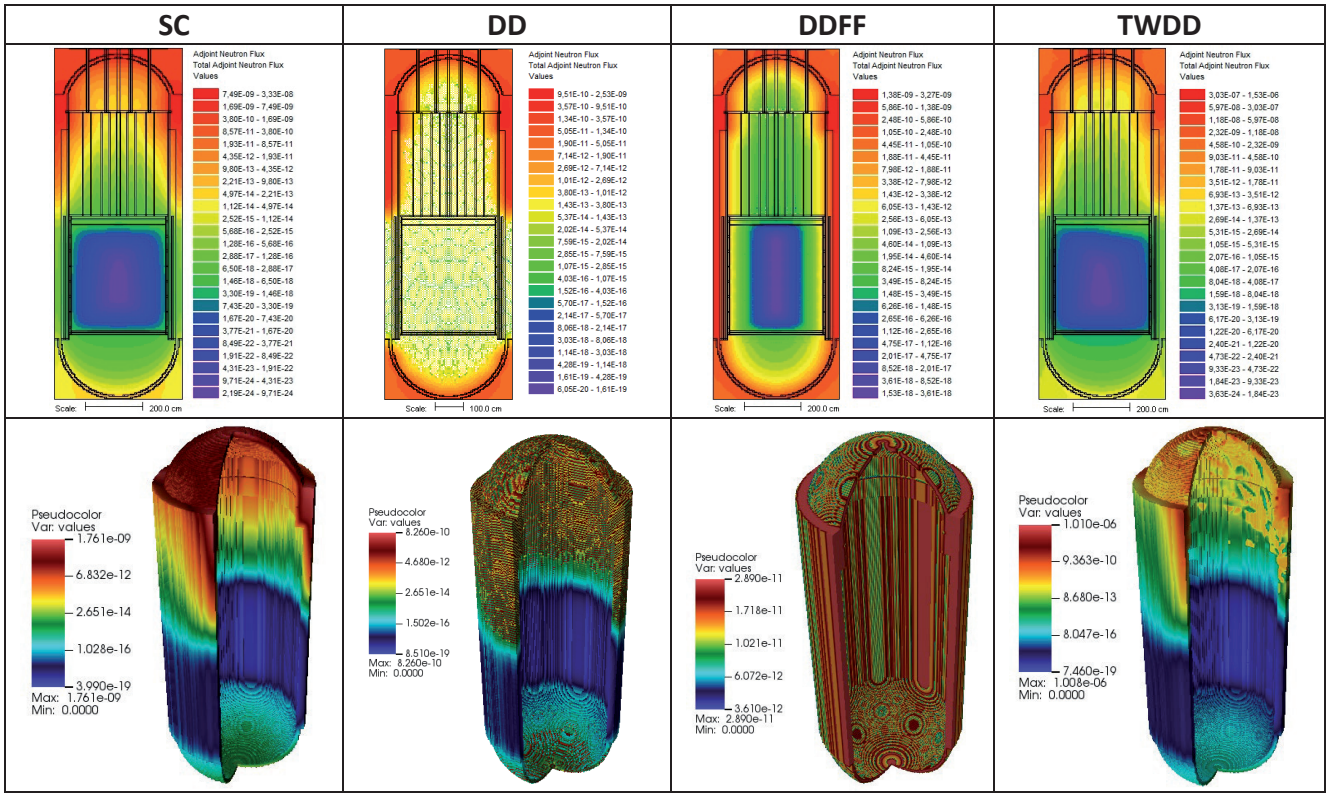

1 DD (diamond difference), DDFF (diamond difference flux-fixup), TWDD (theta-weighted diamond difference), LDFE (linear discontinuous finite element), SC (step characteristic), TLDFE (trilinear discontinuous finite element).

Mario Matijević, Krešimir Trontl, Dubravko Pevec, RPV Irradiation Simulation Using the Contributon Flux Solution, Journal of Energy, vol. 74 Number 2 (2025), 31–38
https://doi.org/10.37798/2025742728

The MAVRIC simulation cases with various spatial schemes using S10/P1 parameters are shown in Table 2 with CPU timing for different FW-CADIS calculation steps. The case-based MC total dose rate distribution is shown in Figure 2, while associated relative errors are shown in Figure 3. It is evident that only SC spatial scheme generated VR parameters which are capable of producing uniform flux distribution over the RPV interior. The obtained results also predict the region of upper RPV head and underneath space as the most difficult one for neutron transport, demanding alternative importance map capable of "pushing" neutrons through these highly attenuating materials. This shielding problem was therefore selected for testing contributon-based SN mesh refinement approach but using full MC model and back-scattering of fast neutrons from biological shield in cavity space.

TABLE II:
THE CPU TIME FOR DIFFERENT SPATIAL SCHEMES USING S10/P1

Spatial scheme	Denovo forward SN (hrs)	Denovo adjoint SN (hrs)	Total Denovo SN (hrs)	Monaco MC (hrs)	Total SN + MC (hrs)
SC	7.69	10.35	18.04	37.04	55.08
DD	4.23	5.81	10.04	6.11	16.15
DDFF	1.30	18.82	20.12	22.58	42.70
TWDD	12.03	16.20	28.23	39.27	67.50
LDFE	6.01	9.09	15.1	89.45	104.55
TLDFE	28.74	39.30	68.04	36.97	105.01

V. RPV HEAD IRRADIATION USING CONTRIBUTON THEORY

This section demonstrates usage of the contributon theory in the FW-CADIS framework to develop an improved adjoint-forward flux solution by means of local SN mesh refinement. The objective of calculation is to optimize upper RPV head irradiation by fast neutrons ($E > 0.1$). Using the total or energy-integrated contributon flux as an information for mesh refinement is a reasonable approach in case of simulating fast neutron transport above 0.1 MeV, i.e. only first 8 energy groups in the broad shielding library "v7_27n19g" and first 106 groups in the fine library "v7_200n47g". Visually inspecting multigroup SN flux solutions in the fast energy range, one can notice a high degree of similarity between group flux profiles, implying overall similar neutron reactions and mean free paths. The energy-integrated flux will thus be a good representative, in an averaged sense, for particle interactions in those fast neutron groups, so user can perform forward-adjoint flux folding to produce a total contributon flux. This approach proved to be useful for fast neutron transport, since only the most energetic neutrons will have the highest probability for reaching the distant RPV regions. In case the user objective is in total flux or dose rates inside RPV, complete neutron spectrum must be taken into account but with gross difference in group-wise flux profiles of forward, adjoint and contributon - this implies how the total contributon flux will not be a good representative for all groups, so group-wise SN mesh refinement would be necessary. For that

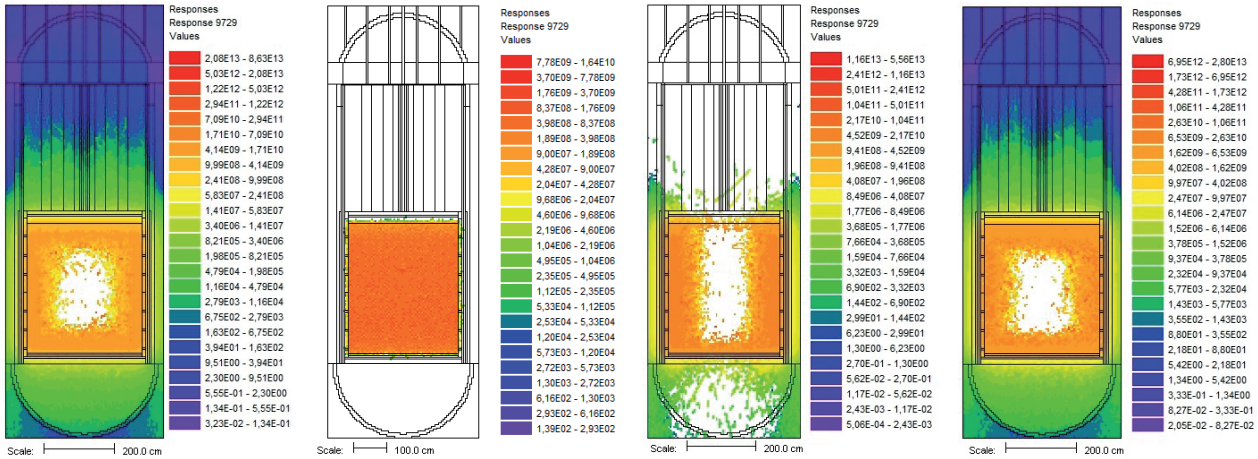

Fig. 2. MC total dose distribution (rem/hr) - SC, DD, DDFF, TWDD

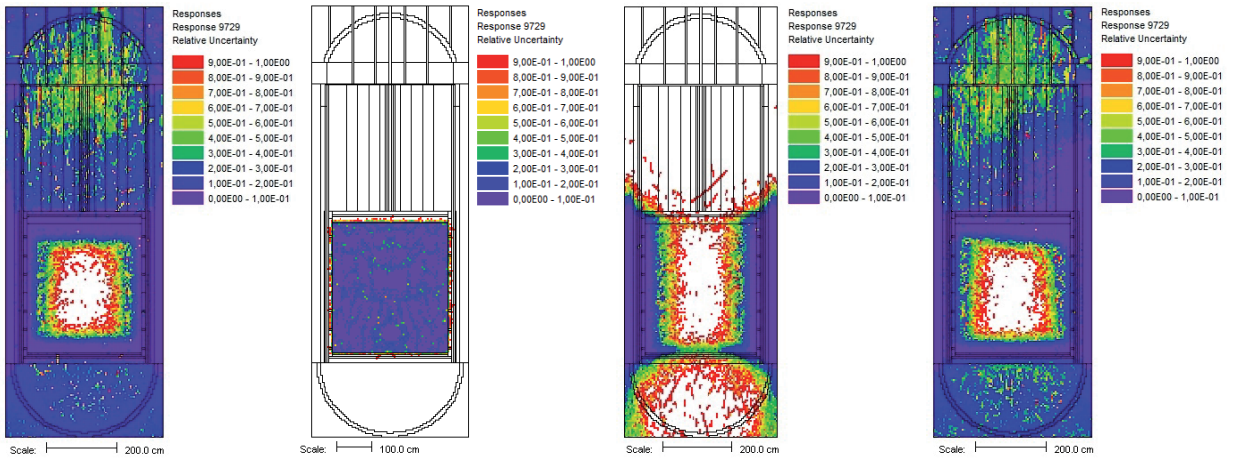

Fig. 3. MC total dose relative error - SC, DD, DDFF, TWDD

Mario Matijević, Krešimir Trontl, Dubravko Pevec, RPV Irradiation Simulation Using the Contributon Flux Solution, Journal of Energy, vol. 74 Number 2 (2025), 31–38
https://doi.org/10.37798/2025742728

case, neutron spectrum decomposition is needed, and SN mesh refinement should be done on group-by-group basis using an exact multigroup contributon solution [16].

To summarize our approach: using the total contributon flux for local SN mesh refinement is apparently justified when transporting fast neutrons which is our case of RPV irradiation with neutrons above 0.1 MeV. Auxiliary MAVRIC utilities were used to post-process intermediate Denovo SN results of FW-CADIS methodology in the following steps:

1. Basic FW-CADIS solution of fast neutron flux in RPV head
2. Copy multigroup forward and adjoint fluxes from a temp directory
3. Repair zero or negative cell flux values in forward and adjoint solutions
4. Construct multigroup contributon as product of forward and adjoint components
5. Integrate multigroup contributon to a total or single-group value
6. Normalize total contributon using maximum cell-value
7. Use a high-pass filter to retain contributon values above user value [2]

The last point should be commented: the total contributon flux can be "clipped" by manually increasing the lowest distribution value, with an upper value of 1.0 due to normalization. In this way the user has an ability to fine-tune distribution and retain only that amount of information judged to be important for the shielding objective. In this study we have retained the normalized contributon information in three ranges (or cases): a) 0 - 0.1; b) 1 - 0.01; c) 1 - 0.001.

A. MAVRIC FW-CADIS Basic and Contributon-Based Solution

The basic FW-CADIS solution of RPV head irradiation is presented next. The fast neutron spectrum above 0.1 MeV was prepared in a simple histogram form:

```
    response 99
       title="fast neutron spectrum above
0.1 MeV"
     neutronBounds 0.01e-10 1.0e-05  0.1e+06
20.0e+06  end
      values 0.0  0.0  1.0  end
    end response
```

The adjoint source was spatially limited to upper head with a fast neutron spectrum ($E > 0.1$ MeV). Denovo SN was used with "`respWeighting`" option, S4/P1 with SC spatial differencing, shielding library was "v7-27n19g", lower tolerance of 1e-6 for fluxes, and macromaterial option which produced 450 pseudo-materials from basic 23. The option "`saveExtraMaps`" was activated for keeping intermediate SN results. The SN mesh was uniform with 1.6e6 cells (85x85x220) covering cylindrical global unit (diameter 828 cm, height 2140 cm), giving cell size of cca 10 cm. Monaco MC was used with 10e6 neutron histories (200 batches, 50000 per batch) with "`allowShortImpMap`" option, "`noFissions`" and "`noSecondaries`" options, and fine group shielding library "v7-200n47g". The MC mesh tally was uniform with 2.0e6 cells (92x92x240) covering the same unit, giving cell size of 9 cm. The distribution of forward and adjoint SN source is presented in Figure 4, with a clear effect of source axial biasing and forward-weighting.

2 Based on engineering judgement by visually inspecting contributon distribution

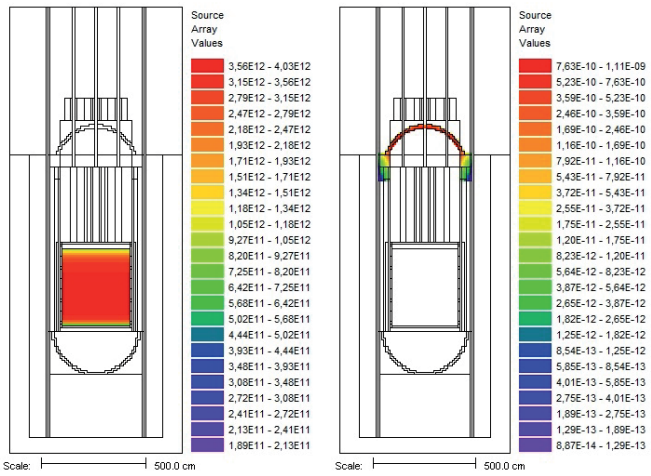

Fig. 4. Distribution of forward and adjoint SN source

The distribution of forward, adjoint and contributon flux is presented in Figure 5. It is seen how the axial PWR region above the core has the highest neutron attenuation, effectively shielding the upper head from fast neutrons. The contributon maximum is located in the cavity region of biological shield, indicating intense neutron streaming and back-scattering. Finally, the mesh tally of fast neutron flux with relative errors is shown in Figure 6. The RPV upper head flux was 6.12e4 n/cm^2/s with relative error of 31%, which is statistically not acceptable MC solution after 20 CPU hours. To lower the RPV head error to cca 10%, which would be a satisfactory result regarding the model size, a factor of 9 increase would be needed in histories and CPU time, amounting to 180 hours per run. Even then there is no strict guarantee that MC relative error would decrease as $1/\sqrt{N}$, where N is the number of neutron histories.

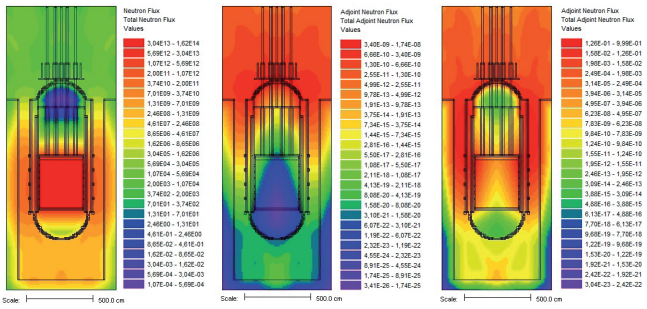

Fig. 5. Forward, adjoint and contributon SN flux solution

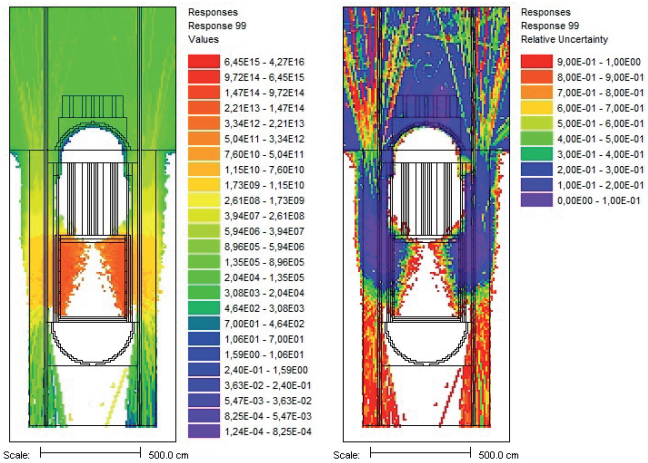

Fig. 6. MC fast neutron flux solution (n/cm2/s) with relative errors

Mario Matijević, Krešimir Trontl, Dubravko Pevec, RPV Irradiation Simulation Using the Contributon Flux Solution, Journal of Energy, vol. 74 Number 2 (2025), 31–38
https://doi.org/10.37798/2025742728

The total contributon flux is now presented in three ranges as stated before and shown in Figure 7: A (1 - 0.1), B (1 - 0.01) and C (1 - 0.001). The fast neutron streaming is very indicative, showing importance of fast neutron scattering on biological shield for upper head irradiation. This phenomenon is pronounced in axial cavity direction (not inside RPV) so SN mesh refinement in z-axis could be an effective method to improve VR parameters. The idea is to locally rebalance SN mesh with a minimum increase in total cell number. For that purpose, a short C-program was written for generating locally refined SN mesh in accordance with contributon ranges, in a format suitable for SCALE input. The mesh refinement process is shown in Figure 8, where smaller cells correspond to important regions by contributon values from Figure 7. It should be emphasized how Denovo works only on Cartesian structured meshes, so every plane defined in *x*, *y* or *z* axis extends through the whole domain.

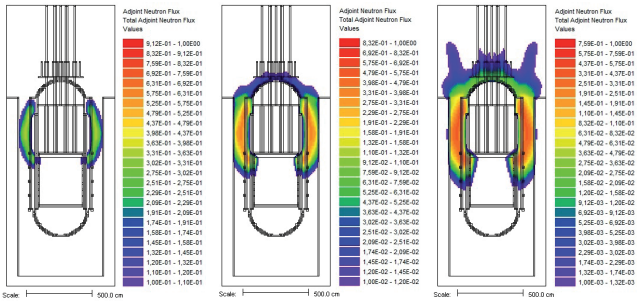

Fig. 7. Contributon flux with ranges A, B and C showing important regions

Using such axially refined SN meshes the FW-CADIS shielding calculation of PWR head was repeated three times and obtained results are presented in Figure 9. A small improvement in overall MC statistics can be seen for range B, but it's more useful to present obtained result in a tabulated form. Tables 3, 4, and 5 provide such comparison between basic run and contributon runs (A, B, C) with varying order of quadrature sets (S4, S8, S24).

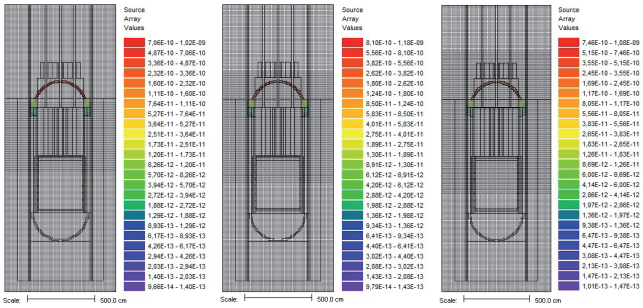

Fig. 8. Local SN mesh refinement for contributon ranges A, B and C

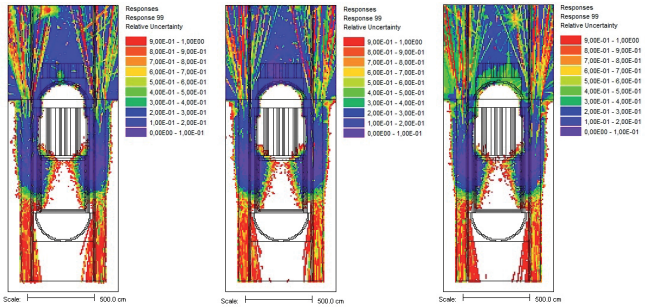

Fig. 9. MC fast neutron flux errors for contributon ranges A, B and C

One can notice cases of drastic improvement in upper head MC statistics with a minimal cell number increase for locally refined SN meshes. This is particularly true for S4/P1 variant where refined mesh incurred only 20% more cells but resulted in 3.4 times lower error. The improved quadrature sets resulted in drastic CPU time decrease of MC runs, but only at expense of long SN runs, so total (SN+MC) CPU time gets the same for S4 and S24 sets. Of course, using high-order quadrature sets will produce small values of ordinates μ_N, so to preserve SN flux positivity the mesh spacing should be more stringent in meeting the criterion $\Delta / \lambda < 2|\mu_1|$, where Δ is the cell size, λ is the neutron mfp (mean free path) and $|\mu_1|$ is the minimum value in the quadrature set [2]. Since it's not always easy to meet such criterion with interdependence of SN/PN parameters and mesh size, the proposed step 3. proved to be useful for numerical stability of FW-CADIS. Considering the total CPU time of only 7.9 hrs for reaching similar MC results, it appears how S8/P1 parameters would be suitable for contributon-informed hybrid shielding simulations with FW-CADIS methodology.

Table III:
Influence of Contributon Level on FW-CADIS with S4/P1

FW-CADIS S4/P1 case	MC upper head flux (n/cm^2/s)	MC error (1 sigma)	FOM (/min)	SN + MC time (hrs)	refined mesh / basic mesh
Basic run	6.12E+04	0.31	8.76E-03	0.8 + 20.0	1.00
Contributon A	6.82E+04	0.26	9.01E-03	0.9 + 26.4	1.18
Contributon B	4.59E+04	0.09	8.62E-02	0.9 + 21.6	1.20
Contributon C	1.27E+05	0.41	3.16E-03	1.0 + 31.2	1.29

Table IV:
Influence of Contributon Level on FW-CADIS with S8/P1

FW-CADIS S8/P1 case	MC upper head flux (n/cm^2/s)	MC error (1 sigma)	FOM (/min)	SN + MC time (hrs)	refined mesh / basic mesh
Basic run	5.90E+04	0.13	1.53E-01	2.2 + 6.8	1.00
Contributon A	4.93E+04	0.09	3.76E-01	2.6 + 5.3	1.20
Contributon B	8.73E+04	0.26	4.04E-02	2.7 + 6.2	1.21
Contributon C	6.24E+04	0.12	1.88E-01	2.6 + 5.8	1.21

Table V:
Influence of Contributon Level on FW-CADIS with S24/P1

FW-CADIS S24/P1 case	MC upper head flux (n/cm^2/s)	MC error (1 sigma)	FOM (/min)	SN + MC time (hrs)	refined mesh / basic mesh
Basic run	6.84E+04	0.11	4.39E-01	16.2 + 2.9	1.00
Contributon A	5.20E+04	0.08	9.45E-01	17.8 + 2.7	1.09
Contributon B	7.01E+04	0.17	1.98E-01	17.6 + 2.8	1.11
Contributon C	5.70E+04	0.08	9.55E-01	18.2 + 2.8	1.13

Mario Matijević, Krešimir Trontl, Dubravko Pevec, RPV Irradiation Simulation Using the Contributon Flux Solution, Journal of Energy, vol. 74 Number 2 (2025), 31–38
https://doi.org/10.37798/2025742728

Finally, it's worth noting how increasing the axial refinement region by considering contributon flux with a small lower bound, one would lose "locality" of SN mesh refinement and produce a new mesh with a worsen aspect ratio of the mesh voxels, i.e. combination of small and large cells. This situation can be seen for S4/P1 variant, case C, where MC error jumped to 41% even though refined mesh had 29% more cells compared to the basic run.

Conclusion

This paper investigates a potential improvement in FW-CADIS hybrid shielding methodology by using the contributon theory. The contributon flux, created by folding forward-adjoint SN solution, proved to be useful for subsequent local SN mesh refinement and improved variance reduction parameters preparation. The pseudo-particle flux of contributons is coming from spatial channel theory which can locate spatial regions important for contributing to a shielding response. This approach was successfully applied to a difficult shielding problem of RPV upper head irradiation by fast neutrons ($E > 0.1$ MeV). The contributon maximum was noticed in the axial cavity region of the biological shield, implying high influence of neutron streaming and scattering for reaching the RPV upper head. Three ranges of normalized contributon flux were proposed and used for subsequent axial mesh refinement. The refined SN mesh proved to be a rather sensitive to voxel aspect ratio but finally produced improved MC results with minimal increase in cells. Numerical investigation showed how S8 quadrature set on refined mesh produced satisfactory MC result with CPU time decrease of almost 3 times compared to S4 and S24 sets. The obtained conclusions should be however used judiciously, since more numerical investigation is necessary on similar deep-penetration shielding problems.

References

[1] J.C. Wagner, A. Haghighat, "Automated Variance Reduction of Monte Carlo Shielding Calculations Using the Discrete Ordinates Adjoint Function," *Nuclear Science and Engineering*, Vol. 128, 2, 186, 1998.

[2] E.E. Lewis and W.F. Miller Jr., Computational Methods of Neutron Transport, American Nuclear Society, 1993.

[3] J.C. Wagner, D.E. Peplow, S.W. Mosher, "FW-CADIS method for global and regional variance reduction of Monte Carlo radiation transport calculations," *Nuclear Science and Engineering*, Vol. 176, no. 1, pp. 37–57, 2014.

[4] J.C. Wagner, E.D. Blakeman, D.E. Peplow, "Forward weighted CADIS method for global variance reduction," *Transactions of the American Nuclear Society*, Vol. 97, pp. 630–633, 2007.

[5] M.L. Williams, W.W. Engle, Jr., The Concept of Spatial Channel Theory Applied to Reactor Shielding Analysis, *Nuclear Science and Engineering*, Vol.62, pp. 92-104, 1977.

[6] W.A. Wieselquist, R.A. Lefebvre, M.A. Jessee, Eds., SCALE Code System, ORNL/TM-2005/39, Version 6.2.4, Oak Ridge National Laboratory, Oak Ridge, Tennessee (2020). Available from Radiation Safety Information Computational Center as CCC-834.

[7] D.E. Peplow, "Monte Carlo Shielding Analysis Capabilities with MAVRIC," *Nuclear Technology*, Vol. 174, no. 2, pp. 289–313, 2011.

[8] G.I. Bell, S. Glasstone, Nuclear Reactor Theory, Van Nostrand Reinhold Company, Litton Educational, New York, NY, USA, 1970.

[9] T.M. Evans, A.S. Stafford, R.N. Slaybaugh, K.T. Clarno, "Denovo: a new three-dimensional parallel discrete ordinates code in SCALE," *Nuclear Technology*, Vol. 171, no. 2, pp. 171–200, 2010.

[10] D.E. Peplow, T.M. Evans, J.C. Wagner, "Simultaneous optimization of tallies in difficult shielding problems," *Nuclear Technology*, Vol. 168, no. 3, pp. 785–792, 2009.

[11] J.C. Wagner, D.E. Peplow, S.W. Mosher, T.M. Evans, "Review of hybrid (deterministic/monte carlo) radiation transport methods, codes, and applications at Oak Ridge National Laboratory," *Progress in Nuclear Science and Technology*, Vol. 2, pp. 808–814, 2011.

[12] M.L. Williams, Generalized Contributon Response Theory, *Nuclear Science and Engineering*, Vol. 108, pp. 355-383, 1991.

[13] M. Matijević, D. Pevec, K. Trontl, Dose rates modeling of pressurized water reactor primary loop components with SCALE6.0, *Nuclear Engineering and Design*, Vol. 283, pp. 175-192, 2015.

[14] M. Matijević, D. Pevec, K. Trontl, PWR Containment Shielding Calculations with SCALE6.1 Using Hybrid Deterministic-Stochastic Methodology, *Science and Technology of Nuclear Installations*, Vol. 2016, pp. 1-30, 2016.

[15] "SCALE: A Comprehensive Modeling and Simulation Suite for Nuclear Safety Analysis and Design", ORNL/TM-2005/39, Version 6.1, June 2011. Available from Radiation Safety Information Computational Center at Oak Ridge National Laboratory as CCC-785.

[16] T. Flaspoehler, B. Petrovic, Contributon-Based Mesh-Reduction Methodology for Hybrid Deterministic-Stochastic Particle Transport Simulations Using Block-Structured Grids, *Nuclear Science and Engineering*, Vol. 192, Issue 3, pp. 254-274, 2018.

[17] VisIt: An End-User Tool for Visualizing and Analyzing Very Large Data, VisIt User's Manual, Version 1.5, UCRL-SM-220449, Lawrence Livermore National Laboratory, Weapons and Complex Integration, 2005.

Mario Matijević, Krešimir Trontl, Dubravko Pevec, RPV Irradiation Simulation Using the Contributon Flux Solution, Journal of Energy, vol. 74 Number 2 (2025), 31–38
https://doi.org/10.37798/2025742728

ENERGIJA